
UNIVERSITÀ DEGLI STUDI
DI GENOVA

PhD Program In Bioengineering And Robotics


# INNOVATIVE PLATFORMS FOR QUANTITATIVE *IN VITRO* CHARACTERIZATION OF CARDIAC ELECTRO-CONTRACTILE ACTIVITY

Thesis submitted for the degree of Doctor of Philosophy (38° cycle)


Supervisor

Prof. Roberto Raiteri

Candidate

Cecilia Beccari

Dibris

Department of Informatics, Bioengineering, Robotics and Systems Engineering

# Abstract

Cardiovascular diseases remain the leading cause of mortality worldwide, while cardiotoxic side effects continue to limit the safety and efficacy of many pharmacological therapies. Advanced experimental methods capable of capturing early and subtle functional alterations of cardiac tissue are therefore essential for improving pre-clinical investigation. In this context, *in vitro* cardiac models represent powerful and versatile tools, providing quantitative, reproducible, and physiologically relevant assessment of both electrophysiological and contractile cardiac function. However, most existing platforms investigate these two aspects separately or provide only qualitative readouts averaged over large populations, limiting their translational relevance for disease modeling and drug screening. This PhD work focuses on the development and validation of multimodal experimental platforms for integrated and quantitative investigation of electro-contractile-mechanical properties in *in vitro* cardiac models, with the aim of identifying functional biomarkers sensitive to pathological conditions and pharmacological interventions. In the first part of the work, a combined Atomic Force Microscopy–Microelectrode Array (AFM MEA) platform was optimized to enable synchronized, single-cell-level measurements of extracellular field potentials, contractile behavior, and mechanical properties in a two-dimensional cardiac model. This system was employed to study doxorubicin-induced cardiotoxicity and to evaluate the cardioprotective potential of extracellular vesicles derived from human amniotic fluid stem cells (hAFSC-EVs). The results reveal that doxorubicin induces marked alterations in both electrical and contractile parameters, while pre-treatment with extracellular vesicles partially mitigates these effects, highlighting their cardioprotective potential. In the second part, to overcome the low-throughput limitation of the AFM-MEA setup, a novel hybrid platform integrating an active Thin-Film Transistor Microelectrode Array (TFT-MEA) with a flexible Micro-Pillar Array (MPA) was developed. Preliminary results demonstrated the platform's potential to enable high-throughput, label-free recording of both electrical and contractile activity from different regions of the same cardiomyocyte population. Pharmacological validation with isoprenaline confirmed the platform's sensitivity and reliability for multimodal functional analysis and drug screening applications. Overall, this work proposes innovative experimental tools for the quantitative and integrated study of cardiac electro-contractile coupling *in vitro*, either at single-cell level with low-throughput or at the cell population level with high-throughput. These approaches offer new opportunities for cardiotoxicity assessment and drug screening, and represent a step toward more predictive and safer preclinical evaluation of therapeutic strategies.

## *Contents*

# List of Figures

# List of Tables

# Chapter 1 - General Introduction

## 1.1 Cardiovascular Diseases

If you are reading a scientific article related to cardiovascular research, it's likely you'll come across the following sentence: *"Cardiovascular diseases are the leading cause of death worldwide."* But why do cardiovascular diseases consistently top the list of global mortality causes year after year? And what can be done to reduce their impact?

While significant progress has been made in both research and clinical practice, there is still a pressing need to improve early identification of risk factors, encourage healthier lifestyles, and develop novel experimental models and more targeted therapies [1],[2],[3].

According to the World Health Organization (WHO), approximately 19.8 million people died from cardiovascular diseases in 2022, accounting for about 32% of all global deaths. More than 75% of these deaths occur in low- and middle-income countries, where access to timely diagnosis and adequate treatment is often limited [4].

Despite their high prevalence, the biological mechanisms underlying many cardiovascular conditions remain only partially understood, and effective therapeutic strategies are still limited. Consequently, there is a continuous need to improve early identification of risk factors, promote preventive strategies, and develop experimental models capable of supporting the discovery of safer and more effective therapies [5].

CVDs comprise a heterogeneous group of disorders affecting the heart and blood vessels. Major categories include ischemic heart disease, peripheral artery disease, hypertension, valvular diseases, cardiomyopathies, and cardiac arrhythmias. These conditions may present as acute events, such as myocardial infarction or cardiac arrest, or follow a chronic course characterized by progressive deterioration of cardiac function [6].

Beyond their impact on mortality, cardiovascular diseases represent a major source of chronic morbidity. Many patients survive acute cardiovascular events but experience long-term complications that significantly impair quality of life and impose a substantial burden on healthcare systems worldwide [7]. The economic cost associated with cardiovascular diseases is therefore extremely high. In the United States alone, direct and indirect healthcare expenses related to CVDs exceed $350 billion per year [8].

Cardiovascular diseases can originate from congenital defects present at birth or develop later in life as acquired conditions. While genetic predisposition and aging contribute to disease susceptibility, a large proportion of cardiovascular disorders are strongly associated with modifiable lifestyle-related risk factors, including hypertension, hypercholesterolemia, type 2 diabetes mellitus, smoking, poor diet, physical inactivity, and excessive alcohol

consumption [9]. It has been estimated that up to 90% of cardiovascular diseases are linked to these modifiable factors and could potentially be prevented through early intervention and lifestyle modifications [10],[11].

While traditional cardiovascular risk factors remain critically important, increasing attention has recently been directed toward additional contributors to cardiac dysfunction, including adverse effects associated with pharmacological treatments [12],[13]. Among these, drug-induced cardiotoxicity has emerged as a major challenge in both clinical practice and drug development.

## 1.2 Cardiotoxicity

Cardiotoxicity refers to the potential of certain chemical agents to damage the heart tissue, affecting either electrical conduction or pumping function [14],[15]. Cardiotoxic substances may lead to heart failure, arrhythmias, myocarditis, or cardiomyopathies [16]. While some cardiotoxic effects are reversible, others may cause permanent structural and functional damage. Generally, cardiac injury manifests as a reduction in stroke volume and ventricular ejection. Cardiotoxicity may be caused by drug treatments—referred to as pharmacological cardiotoxicity—or by other interventions, like radiotherapy [17].

This phenomenon is one of the main reasons behind the failure of many drug candidates during clinical trials and is also responsible for the withdrawal of several medications from the market. Statistic studies report that cardio-toxic drugs are responsible for the 45% of the total post-marketing drug withdrawal from the market [18]. The development of new drugs is a long, expensive process characterized by low success rates and a high risk of failure (approximately 60%) [19]. On average, the journey from discovery to market takes 10 to 15 years, with median costs exceeding $5 billion [20]. For this reason, addressing cardiotoxicity is not only a clinical necessity but also a major economic challenge.

To advance toward more effective diagnosis and therapy, enhancing early diagnostic capabilities becomes crucial. Detecting cardiovascular alterations at a stage when functional changes are still reversible can make a significant difference in clinical outcomes. However, diagnosis alone is not enough: there is a growing demand for treatments that are more effective, more personalized, and have fewer side effects.

Despite progress in drug design and the identification of new therapeutic targets, the development of cardiac therapies still lags behind other fields, such as oncology [21].

Moreover, cardiotoxic side effects are sometimes discovered only after the drug has been released to the market. This limitation is partly due to the high costs associated with drug screening and the shortcomings of current preclinical testing platforms.

As a result, there is a clear need for new platforms that are physiologically relevant, cost-effective, and high-throughput, capable of improving both cardiac drug discovery and safety assessment [22]. It is in this context that advanced experimental platforms capable of mimicking the physiological and pathological conditions of the human heart become essential. These systems allow researchers to better understand disease mechanisms, design preventative strategies, evaluate drug safety and efficacy, assess cardiotoxicity, and test potential cardioprotective strategies.

Any new treatment must go through a stringent regulatory approval process, demanding robust preclinical and clinical trial data.

To reach the clinical trial phase, solid preclinical evidence is required, often through a combination of methods at the interface of biology and engineering—including *in vivo*, *ex vivo*, *in vitro*, and *in silico* models.

These experimental approaches rely on different types of biological models, each providing specific advantages and limitations depending on the research objective.

## 1.3 Models

*In vivo* models refer to studies conducted in living organisms such as laboratory animals (e.g., mice, rats) and, in some cases, humans. These models preserve natural physiological interactions and allow for the observation of systemic effects such as metabolism or inter-organ communication [23],[24]. Historically, *in vivo* models have been the cornerstone of biomedical research and the gold standard for evaluating cardiac therapeutics, enabling major advancements in our understanding of human physiology and the development of new therapies for numerous conditions [25].

However, these models come with several limitations. Animal studies require expensive equipment, trained personnel, and specialized facilities. The duration of experiments is often long, and they do not allow for the evaluation of large numbers of drug candidates. Ethically, the use of animals raises serious concerns, especially considering the inevitable sacrifice involved [25]. Furthermore, interspecies differences in anatomy, physiology, and genetics often limit the translation of findings to humans, contributing to high failure rates in clinical trials [26],[27]. *Ex vivo* models involve the study of tissues or organs extracted from living organisms and maintained outside the body for a limited time.

These models retain some physiological structure and function in a more controlled environment than *in vivo* studies. However, they suffer from limited viability once removed from the body and pose standardization challenges that affect reproducibility [28],[24].

*In silico* models rely on computer simulations and mathematical algorithms to model biological processes, drug kinetics, or molecular interactions. These models are becoming increasingly powerful thanks to advances in AI and bioinformatics. They offer the ability to rapidly explore clinical scenarios at low cost and large scale. However, they cannot fully replicate biological complexity and depend heavily on the quality and availability of input data. While they are invaluable for guiding experiment design, they cannot yet completely replace experimental validation [29],[30].

*In vitro* models, finally, are conducted in artificial environments such as petri dishes or culture plates. They allow the study of specific cellular or molecular mechanisms under highly controlled, standardized, and reproducible conditions [24]. Although they cannot capture the full complexity of a living organism, they offer several advantages over *in vivo* models: lower cost, ethical viability, and faster data acquisition [31],[32]. Depending on the model type, both short- and long-term studies can be performed, making them ideal for disease research and drug screening—provided their systemic translation limitations are acknowledged [33].

In this landscape, *in vitro* cardiac models stand out for their ability to combine reproducibility, adaptability, and cost-effectiveness with detailed functional analysis. They have become particularly valuable for studying cellular mechanisms, evaluating drug safety, and developing advanced experimental platforms capable of simultaneously monitoring multiple aspects of cardiac function [34],[20].

Crucially, these models must also allow the extraction of specific, physiologically relevant parameters aligned with the research objective. To identify such parameters, it is therefore necessary to understand the physiological mechanisms that govern the electrical and mechanical activity of cardiomyocytes.

## 1.4 Physiological basis of cardiac electrocontractile activity

The heart is responsible for pumping blood throughout the body, delivering oxygen and nutrients to tissues while removing metabolic waste products. This function is made possible by the coordinated electrical and mechanical activity of cardiomyocytes.

Cardiac electrical activity originates in specialized pacemaker cells located in the sinoatrial node. From these cells, the electrical signal propagates through the atria, reaches the atrioventricular node, and is subsequently transmitted along the His–Purkinje conduction

system, ultimately activating ventricular cardiomyocytes. The propagation of this impulse ensures the coordinated contraction of the myocardium, which beats at a rate of approximately 60–90 beats per minute and pumps about 5 liters of blood per minute throughout the body [13],[35].

At the cellular level, the impulse transmission between pacemaker cells and between nodal and contractile cells occurs through the passage of ionic current between one cell and the next, via intercalated discs (gap junctions and desmosomes), enabling the myocardium to behave as a functional syncytium, allowing rapid propagation of excitation throughout the whole tissue [36],[37]. The resting membrane potential (the potential difference across the cell membrane) of a pacemaker cell is approximately –60 mV. Spontaneously, thanks to $Na^+$ entry through funny sodium channels, the membrane potential becomes less negative, triggering the opening of T-type and L-type calcium channels, allowing $Ca^{2+}$ inflow and full depolarization of the cell (+40 mV) [38]. At this point, cations in the nodal cells pass to adjacent contractile cells, which have a resting membrane potential around –80/–90 mV. The influx of positive ions and the rise of membrane potential to the threshold (–70 mV) causes opening of voltage-gated sodium channels, with further $Na^+$ inflow and an increase in membrane potential. When about +10 mV is reached, $Na^+$ channels close and $Ca^{2+}$ and $K^+$ channels open, causing slow $Ca^{2+}$ entry and greater $K^+$ efflux; this leads to a slight drop in membrane potential (to 0 mV), followed by the “plateau phase”, during which the membrane potential stays nearly constant, due to simultaneous $Ca^{2+}$ inflow and $K^+$ outflow [39],[40].

Calcium ions play a central role in linking electrical excitation to mechanical contraction. $Ca^{2+}$ ions entering through L-type $Ca^{2+}$ channels bind to ryanodine receptors (RyR2) on the sarcoplasmic reticulum (SR) membrane, triggering the opening of additional $Ca^{2+}$ channels and the phenomenon called "calcium-induced calcium release" (CICR). This leads to a massive release of $Ca^{2+}$ from the SR into the cytosol.

The released $Ca^{2+}$ binds to troponin C, causing actin–myosin interaction and initiating cross-bridge cycling: the sliding of actin over myosin filaments causes cell contraction. The direct connection between adjacent cells ensures synchronization, forming a functional syncytium and resulting in coordinated contraction of the entire myocardium [41],[42],[43].

After contraction, cells undergo repolarization, returning to their resting potential in preparation for the next contraction. In pacemaker cells, after reaching +40 mV, $Na^+$ and $Ca^{2+}$ channels close while $K^+$ channels open, causing $K^+$ to leak out and reducing the membrane potential back to resting levels [44],[45].

This decrease means fewer positive ions enter adjacent contractile cells, ending the plateau phase; cytosolic $Ca^{2+}$ is taken back into the sarcoplasmic reticulum by SERCA pumps and expelled from the cell by $Na^{+}/Ca^{2+}$ exchangers (NCX) and $Ca^{2+}$-ATPase pumps, ending contraction and allowing the cell to rest. Simultaneously, massive $K^{+}$ efflux returns the contracting cell's membrane potential to resting values, completing repolarization and the "excitation–contraction" cycle [46].

Understanding this sequence of electrical activation, calcium signaling, and mechanical contraction is fundamental for investigating cardiac physiology. Consequently, experimental platforms capable of simultaneously measuring electrical activity and contractile behavior provide valuable tools for studying cardiac function, disease mechanisms, and the effects of pharmacological compounds.

The quantification of the contractile force generated by cardiomyocytes can provide information about the heart's efficiency in pumping blood to the rest of the body. In a preclinical context, measuring this parameter can contribute to the investigation of pathological mechanisms and to the evaluation of drug-induced alterations in cardiac functionality.

At the same time, the detection of electrical activity is equally essential. Extracellular potential recordings reflect the underlying cellular action potential and provide important information about ion currents and the function of the associated ion channels.

For these reason, the simultaneous investigation of electrical activity and mechanical contraction represents a powerful approach for characterizing cardiomyocyte function *in vitro*.

## 1.5 Techniques for investigating cardiac electrocontractile activity

The function of the heart relies on the tight coupling between electrical excitation and mechanical contraction. Electrical signals generated by cardiomyocytes trigger intracellular calcium dynamics, ultimately leading to the contraction of the cardiac muscle. Consequently, a comprehensive characterization of cardiac function requires the simultaneous investigation of both electrophysiological and contractile properties.

Over the past decades, the increasing demand for physiologically relevant *in vitro* cardiac models has driven the development of numerous experimental techniques aimed at investigating these two fundamental aspects of cardiac functional activity. This progress has resulted in experimental platforms and tools capable of extracting essential information related to heart's models' extracellular filed potential and contraction force.

Several techniques are available to measure the contractile force of cardiac cells and tissues, each relying on distinct physical principles and capable of providing unique insights into cellular mechanics.

A widely used approach involves force transducers—commonly referred to as *two-point force transducers*. In this method, the cardiac sample (either single cells or tissue fibers) is positioned between two flexible force-sensing posts. Tissue contraction causes the posts to deflect, and this deflection is measured either optically, using laser-based detection of bending, or electrically, using strain gauges. By knowing the mechanical properties of the posts, the measured deflection can be accurately translated into the force exerted by the tissue [47],[48]. Another method uses *Atomic Force Microscopy* (AFM) for direct measurement of contractile force at the single-cell level. In this technique, a cantilever is brought into contact with the cell surface, and once the feedback loop is disabled, the cell's contraction causes deflection of the cantilever [49]. Given the known spring constant of the cantilever, the force applied by the cell can be directly calculated [50],[51]. This technique will be discussed in more detail later.

*Micro- or nanopillar arrays* offer a valuable tool for force quantification. These devices consist of flexible, elastic polymeric pillars on which cells are seeded. As cells adhere and contract, they bend the pillars, and the resulting deflection can be analyzed to estimate the generated force [52],[53]; this technique will be discussed in more detail later as well.

Techniques that allow force measurement based on optical observations include *video-based approaches* to capture the dynamic behavior of contraction by tracking changes in cardiomyocytes shape using high-resolution imaging [54].

While these methods provide valuable information on contraction kinetics—such as frequency, duration, and amplitude—they do not allow for direct quantification of contractile force, as no straightforward correlation exists between these parameters and force magnitude [55],[56].

Among the most widely adopted optical techniques is *Traction Force Microscopy (TFM)*.

This method involves culturing cells on a soft, deformable substrate embedded with fluorescent beads, which serve as fiducial markers. As cells contract, they deform the substrate, causing displacement of the beads. By tracking bead movement and combining this with knowledge of the substrate's mechanical properties, the magnitude and spatial distribution of the cellular traction forces can be inferred [57],[58],[59].

The use of *flexible substrates* is also widespread for force measurements.

These substrates deform in response to cellular contraction and can be monitored using optical sensors such as laser deflection systems [60],[61]. Alternatively, integrating the substrate with *flexible strain sensors* enables electrical detection: the deformation changes the electrical properties (e.g., resistance or capacitance) of the sensor, which can be measured and correlated with contraction dynamics [62],[63].

Finally, *impedance-based techniques* can provide indirect measurements of cellular activity. By applying an alternating current between *interdigitated electrodes*, the impedance across them varies depending on the presence, morphology, and behavior of the cells cultured on top [64],[65]. While this method can reflect changes in cell adhesion, beating frequency, and morphology, impedance is also influenced by other factors—such as confluency or time in culture—so results must be interpreted with caution.

Electrophysiology techniques are essential tools for investigating cardiac physiology, with different levels of complexity, from the single cell up to the entire tissue or organ. Among these, the gold standard has always been represented by the *patch-clamp technique*, which allows for intracellular electrophysiological measurements at the single-cell level thanks to the use of a micropipette that creates a high-resistance seal with the cell membrane and thus enables the recording of ionic currents inside it, and the studying of the corresponding ion channels. This technique has evolved over time to offer different configurations (whole-cell, inside-out, and outside-out patches) [66],[67]. Although it has exceptional resolution, patch clamp suffers from being technically demanding and low throughput, and to address these limitations and study electrical activity across larger cell populations and tissues, Microelectrode Array (MEA) technology is widely used.

MEAs consist of arrays of microelectrodes integrated into a rigid or flexible substrate, capable of simultaneously measuring extracellular potentials of electrically active cells from more than hundreds of recording site [68],[69]. More information regarding these tools will be provided later. Alongside these electrode-based techniques, there are also optical electrophysiology approaches, including calcium imaging and potentiometric imaging. These methods use fluorescent dyes that are sensitive to intracellular calcium levels and changes in membrane potential, respectively [70].

*Calcium imaging* uses calcium-sensitive dyes or genetically encoded calcium indicators to follow the fluctuations of the $Ca^{2+}$ ion during cardiac activity [71],[72],[73]. Similarly, *potentiometric imaging* uses voltage-sensitive dyes that, by varying their fluorescence signal in response to changes in the electrical signal, allow for tracking variations in the cellular membrane potential [74],[72],[73].

Both optical methods thus enable tracking of electrical signals using fluorescence microscopy setups, integrated with the appropriate filters; limitations of these techniques include issues of dye toxicity, photobleaching, and motion artifacts, which therefore require special attention during data acquisition and analysis.

Despite the availability of numerous techniques for investigating cardiac electrophysiology and contractility, most experimental platforms focus on only one of these aspects, studying either the electrical activity or the mechanical behavior of cardiomyocytes separately [75] [76] [77] [78] [79] [80]. Even when both aspects are considered, many approaches rely on indirect or qualitative measurements of contractile behavior, without providing a direct quantification of the force generated by the cells [81] [82] [83] [84].

As a result, experimental platforms capable of simultaneously measuring electrical activity and quantitatively assessing contractile force remain relatively limited. The development of such integrated systems represents an important step toward a more comprehensive characterization of cardiomyocyte function and toward the creation of advanced *in vitro* platforms for cardiac disease modeling and pharmacological screening.

Nevertheless, several experimental approaches have been proposed in recent years to address this challenge.

Among the experimental platforms developed to simultaneously measure electrical activity and contractile force, several representative examples are described below.

In 2015, Ribeiro et al. studied the functional maturation of hiPSC-CMs by analyzing their electrical properties through patch clamp and their contractile force via imaging of fluorescent beads displacement, through traction force microscopy (TFM).

They observed that the increase in amplitude and speed of the action potential was correlated with an increase in contraction force, highlighting a direct link between electrical activity and mechanical function [85].

In 2018, Caluori and colleagues introduced an organ-on-chip platform combining atomic force microscopy (AFM) and microelectrode arrays (MEA) to non-invasively record electromechanical activity in 3D cardiac models. This system allowed the evaluation of specific drug effects on both a healthy model and one affected by Duchenne muscular dystrophy (DMD), showing how electrophysiological alterations are closely linked to mechanical changes [86].

In 2021, Ohya et al. developed a flexible electronics-based platform, consisting of a deformable substrate for quantitative measurement of contractile force and integrated electrodes for electrical recordings.

The system was tested using various drugs, demonstrating its effectiveness in detecting changes in the electromechanical properties of cardiac cells cultured on the substrate [87].
Also in 2021, Kanade et al. proposed an innovative MEA-on-cantilever device; a flexible cantilever with integrated electrodes enabling simultaneous recording of extracellular potentials and contraction force. The latter was measured from cantilever deflection, detected using a laser vibrometer. The device proved useful for drug toxicity screening on cardiac cells [88].
In 2022, Zhao et al. designed a suspended PDMS structure that integrates MEAs and laser vibrometry, allowing real-time measurement of cellular contractile force and extracellular field potential. The system was tested with lidocaine, further reinforcing the feasibility of simultaneously evaluating electrical and contractile parameters in complex cell models [89].
In 2023, Wu and colleagues developed a heart-on-a-chip platform that integrates flexible 3D-printed PEDOT:PSS micropillar electrodes with nanocomposite microwires, both produced via 3D printing. The micropillars enable recording of the tissue's extracellular electrical activity, while the microwires anchor the cardiac construct and allow optical measurement of its contractile force using embedded fluorescent quantum dots. This platform effectively delivers an integrated, real-time assessment of cardiac function and drug-induced responses *in vitro* [90].
Finally, in 2024 Kanade et al. presented a device integrating a flexible polymer cantilever with embedded electrodes, enabling simultaneous monitoring of cardiac cells' contractile behavior and electrical activity. Mechanical contraction is quantified through cantilever deflection, while electrical signals are recorded via the integrated electrode array. The platform was validated using pharmacological compounds, demonstrating its capability to detect drug-induced alterations in both contractile and electrical cardiac responses [91].
These studies demonstrate the growing interest in experimental platforms capable of simultaneously evaluating the electrical and contractile behavior of cardiac cells and tissues. However, further developments are still needed to achieve systems that provide high-resolution, quantitative, and reproducible measurements of cardiomyocyte electromechanical activity under controlled *in vitro* conditions.

## 1.6 Thesis Objective

The aim of this thesis is to investigate the two fundamental functional aspects of cardiac activity: electrical activity and mechanical contraction. In the heart, these two processes are tightly coupled through excitation–contraction coupling mechanisms, and their simultaneous evaluation provides a more comprehensive characterization of cardiomyocyte function.

However, many experimental approaches currently available for *in vitro* cardiac research investigate these aspects separately, focusing either on electrophysiological activity or on mechanical behavior. Consequently, platforms that enable the simultaneous assessment of both electrical and contractile properties are still relatively scarce.

In this context, the development of experimental systems able to perform simultaneous and quantitative measurements of cardiomyocytes electrocontractile activity represents a promising strategy for improving the characterization of *in vitro* cardiac models and for supporting pharmacological investigations.

The objective of this work is therefore to develop and employ experimental platforms capable of simultaneously monitoring the electrical and contractile activity of cardiomyocytes, enabling the extraction of multiple functional parameters that may serve as potential biomarkers for distinguishing healthy and pathological cardiac models.

Two experimental platforms are presented in this thesis:

AFM–MEA Experimental Platform: This setup combines microelectrode arrays (MEA) for electrophysiological recordings with atomic force microscopy (AFM) for the measurement of contractile and mechanical properties. The system allows simultaneous and synchronized acquisition of electrical signals and contractile force at the single-cell level.

During this thesis, the platform previously developed by our research group was reproduced and further refined, incorporating several improvements. The system was subsequently employed in a pharmacological assay to evaluate the cardioprotective potential of extracellular vesicles (EVs) secreted by human amniotic fluid-derived stem cells (hAFSC) against the cardiotoxic effects induced by Doxorubicin.

TFT–MEA/MPA Experimental Platform: The second platform consists of a system integrating thin-film transistor microelectrode arrays (TFT-MEAs) for electrophysiological recordings with a micropillar array (MPA) module for the analysis of contractile behavior.

Within this framework, my primary contribution was the integration and validation of the contractility-sensing module MPA into the existing TFT-MEA platform, thereby enhancing the system reliability and enabling the simultaneous acquisition of electrical and contractile parameters from *in vitro* cardiac models.

Together, these platforms provide advanced experimental tools to investigate cardiac electromechanical activity and to support the development of physiologically relevant *in vitro* models for cardiac disease research and pharmacological screening, ultimately contributing to the identification of novel functional biomarkers.

# Chapter 2 - AFM-MEA Experimental Platform for Multimodal In Vitro Cardiac Drug Screening

## 2.1 AFM-MEA Experimental Set-Up

The objective of this chapter was to develop and implement an experimental platform integrating microelectrode arrays (MEA) and atomic force microscopy (AFM) to investigate the electro-contractile-mechanical properties of a two-dimensional *in vitro* cardiac model. The combined application of these two technologies enables the simultaneous characterization of electrical activity and contractile behavior at the single-cell level. This integrated approach allows the extraction of electrical, contractile, mechanical, and hybrid parameters that can provide a comprehensive description of cardiomyocyte function.

The experimental setup presented in this chapter builds on previous work developed by our research group [92],[93],[94] and was further optimized during this thesis project for the experimental applications described in section 2.2.

### 2.1.1 Introduction

The study of cardiomyocyte function requires experimental tools capable of simultaneously capturing both electrical and mechanical aspects of cellular activity. Microelectrode arrays (MEAs) provide a well-established method for recording extracellular electrical signals from cardiac cells, while atomic force microscopy (AFM) enables high-resolution measurements of cellular mechanical properties and contractile forces. By integrating these two technologies into a single experimental platform, it becomes possible to investigate the electro-contractile-mechanical behavior of cardiomyocytes with high temporal and spatial resolution.

The following sections briefly describe the principles of MEA and AFM technologies before presenting the integrated experimental setup.

*Microelectrode Array (MEA)*

The first planar microelectrode array (MEA) used for *in vitro* cell culture dates back to 1972, when Thomas and colleagues recorded field potentials from embryonic chick heart cells [95]. MEAs consist of microscopic electrodes—typically made from platinum, gold, or indium-tin oxide (ITO)—embedded on substrates such as silicon or glass. These electrodes are microfabricated and arranged in a grid-like pattern, enabling simultaneous, noninvasive recordings from multiple locations of cells cultured directly on the array surface. This setup allows for long-term monitoring of cellular electrical activity [96],[68],[97]. Cells cultured on

MEAs adhere and interconnect, forming a continuous layer known as a syncytium. When one cell generates an action potential, the electrical activity propagates through the syncytium, and the MEA electrodes capture this as an extracellular field potential (FP). This signal closely mirrors the first derivative of the intracellular action potential (AP) [98],[99]. Beyond recording electrical activity, MEAs can actively stimulate cells electrically [100]. Electrical stimulation has proven not only effective in triggering excitation but also in promoting the morphological and functional maturation of cardiomyocytes [101],[69]. Since their initial use, planar MEAs have undergone significant evolution. Advancements include new substrate materials, the integration of complementary components [102],[103], and expansion into the third dimension to better capture spatially distributed signals [104]. The most widely used MEA fabrication technique is lithography, though it is increasingly combined with other microfabrication methods [105]. While silicon and glass remain standard substrates, polymeric materials are gaining popularity due to their ease of processing, flexibility, biocompatibility, and mechanical compliance with native tissue stiffness [106],[107]. Notably, polydimethylsiloxane (PDMS) [108] and parylene [109] are commonly used alternatives. To address the limitations of two-dimensional cultures, researchers have increasingly adopted three-dimensional (3D) models that more closely mimic *in vivo* cardiac structures. In tandem, MEA technology has evolved to support signal acquisition within 3D tissues such as organoids, spheroids, and engineered scaffolds [110],[111],[112],[113]. The emergence of 3D culture systems also introduced the need for functional perfusion to maintain nutrient and gas exchange. This led to the integration of MEAs with microfluidic devices, enabling dynamic and physiologically relevant culture conditions [114],[115]. Driven by the demand for improved interface properties and application-specific performance, MEAs now come in a vast range of geometries, dimensions, and configurations. These have been tailored and integrated into specialized devices designed to meet the diverse needs of both clinical and research applications [116],[105].

*Atomic Force Microscopy (AFM)*

Atomic Force Microscopy (AFM) was invented in 1986 by Gerd Binnig, Calvin Quate, and Christoph Gerber as one of several Scanning Probe Microscopy (SPM) techniques developed during that decade [117],[118]. All SPM methods aim to obtain the topography of a sample with nanometer resolution by detecting a highly localized interaction between a sharp probe and the sample surface. The ability to generate high-precision surface maps is

made possible by the use of piezoelectric positioners (typically one for each of the x, y, and z axes), which can move the probe relative to the sample with sub-nanometer accuracy [119],[120]. AFM uses a flexible microscopic cantilever as a spring to measure the interaction forces between the tip, attached to the free end of the cantilever, and the sample under investigation. The microcantilever is fixed to a rigid support and bends or deflects in response to local attractive ($F < 0$) or repulsive ($F > 0$) forces between the tip and the sample. The deflection of the microcantilever is detected and converted into an electrical signal [121],[122]. A standard AFM setup consists of the following components: a microfabricated cantilever with a sharp tip, an optical detection system that monitors the cantilever deflection by reflecting a laser beam off the top surface of the cantilever onto a four-quadrant photodiode, a feedback control system that uses piezoelectric actuators to adjust the vertical position of the sample or tip, while raster scanning the sample surface [123]. To quantify cantilever deflection, a low-power focused laser beam is directed onto the reflective back side of the cantilever and the reflected beam hits a four-quadrant photodiode. When the cantilever is undeflected (i.e., not interacting with the sample), the photodiode is aligned so that the laser spot strikes the center of the four quadrants, distributing the light equally between the upper and lower quadrants. In this neutral state, the difference signal between the top and bottom quadrants is zero. As the cantilever experiences force-induced bending upon interaction with the sample, the reflected laser beam shifts slightly, altering the distribution of light on the photodiode [124]. This change produces a voltage signal proportional to the cantilever deflection [125],[126]. The system continuously monitors the cantilever deflection in real time by measuring this voltage signal. This signal is sent to the feedback electronics, which adjust the position of the piezoelectric actuators to maintain a constant interaction force or height, depending on the type of measurement being performed and the information sought [50],[127].

Since its invention, AFM has proven itself as a multi-purpose tool for investigating a wide range of different samples with nanometer-scale resolution, not only for their topographic characterization but also, and above all, for its ability to directly quantify the mechanical properties of a material and to analyze samples in controlled environmental conditions, without the need for any kind of preliminary treatment [128],[124],[129]. Nowadays, thanks to the possibility to operate in liquid environments and at controlled temperature, AFM is a well established technique to study the physical-chemical and mechanical properties of biomolecules and cells at the single-cell level and with (sub-)nanometer resolution [130],[131],[132].

In paragraph 2.1.2 – Experimental Platform, the main components of the experimental platform, the procedures used for acquiring the experimental data, and the analysis methods will be presented. In the subsequent paragraph of the thesis, 2.1.3 – Application of the experimental platform, the electrical, contractile, and mechanical parameters that can be derived from these combined measurements will be presented, together with a discussion of their physiological significance and their potential impact in the context of cardiovascular research, particularly in the areas of disease modeling and pharmacological investigation.

### 2.1.2 Experimental Platform

The experimental set-up described in this chapter combines the simultaneous use of microelectrode arrays (MEA) and atomic force microscopy (AFM) to perform single-cell measurements on a two-dimensional *in vitro* model of cardiac muscle (Fig 2.1).

*1. Set-Up Components*

The following section outlines and describes the structural components of the experimental apparatus.

❖ **Multi Channel Systems (MCS) Recording System:**

- Microelectrode Array (MEA): model 60MEA200/30iR-Ti, composed of 60 electrodes (59 recording sites + one internal reference electrode) coated with a titanium nitride (TiN) layer. The electrodes have a diameter of 30 µm and an interelectrode distance of 200 µm.
- Recording system: model MEA2100-Mini-60-System .

  It consists of several components: headstage, signal collector unit (SCU), interface board (IFB), and software. Thanks to the reduced size of the headstage, the system allows recordings even in confined spaces, such as inside an incubator or under a microscope. In our case, the entire system is positioned under the AFM system that is also equipped with an upright optical microscope. Potentials recorded by the microelectrodes are amplified and digitized directly on the headstage with 24-bit resolution.

  The signal collector unit collects data from the headstages and transfers them to the interface board. Up to 4 headstages can be connected to each SCU, while 2 SCUs can be connected to one IFB.

  The interface board receives data from the SCU via an iX industrial type B cable. In the interface board, a freely programmable digital signal processor can be used for real-time signal detection and feedback. In addition, it provides various analog and digital inputs and outputs for synchronization with other instruments. The interface board connects to the computer via USB 3.0 SuperSpeed.

I employed two analog inputs to collect data from the AFM (cantilever vertical position and cantilever vertical deflection), thus allowing all signals to be visualized and synchronized in real time through the MEA2100-Mini software (Multi Channel Suite – Experimenter). “Experimenter” is an acquisition and online analysis tool with an intuitive drag-and-drop interface. It allows the configuration of virtual experiments (data sources, filters, spike detection, recording), monitoring of battery level and signal quality, and real-time data visualization.

- **Thermostat:** The thermostat is directly connected to the MEA2100-Mini’s headstage to heat the metal backplate in order to maintain the temperature of the cells plated on the MEA at 37 °C.
- **Upright optical microscope** (Zeiss AxioZoom.V16): The optical microscope allows top view of the sample and AFM probe. Together with the motorized sample stage of the AFM it is used to align the AFM probe on the MEA surface with single cell resolution, thus allowing repeated measurement of the same cell at different days *in vitro* (DIV).
- **Atomic Force Microscope (AFM):** model NanoWizard 4.0 Bioscience (Bruker Corp., Berlin, Germany) with the following main components:

  The software for setting the parameter of the various acquisition modes (see below for “Acquisition Modes”). Its interface enables real-time visualization of the piezoelectric actuator and cantilever vertical deflection signals. Sample positioning in the xy-plane is achieved by a dedicated scanner, while a piezoelectric actuator enables precise cantilever movement along the z-axis. The setup further includes the AFM head, which accommodates a holder for mounting the cantilever and enabling measurements. Additional spacers were incorporated to provide sufficient space for the positioning of the MEA2100-Mini headstage beneath the AFM head. In addition, a Vortis™ 2 Controller with Signal Access Module (SAM) allows access to and electronic modification of most analog channels of the AFM software, as well as providing digital input and output channels.

- MONITOR CONNECTORS: Analog channels that directly output the unprocessed electronic signals coming from the NanoWizard® head. These can be used to monitor signals by means of external equipment, and employed for feedback, triggering, etc. C-BNC-Lemo1m cable connects Monitor 1 to the ANALOG INPUT 2 of the IFB, in order to record the vertical deflection of the cantilever in the MCS software.
- ANALOG OUT CONNECTORS: Provide analog output (DAC) channels that can be programmed from the SPM software (High Speed) as well as the output of the analog signals that drive the xyz piezos (Precision), which can be used for monitoring or feedback

purposes. C-BNC-Lemo1m cable connects ANALOG OUT 4 FAST SCANNER Z PIEZO DAC (800 kHz, 20 bit) to ANALOG INPUT 1 of the IFB to record the vertical position of the piezoelectric actuator that controls the cantilever position along the Z-axis (vertical position).

❖ The entire set-up is housed within the **JPK Acoustic Enclosure** and placed on an active vibration isolation table to provide acoustic and mechanical noise reduction.

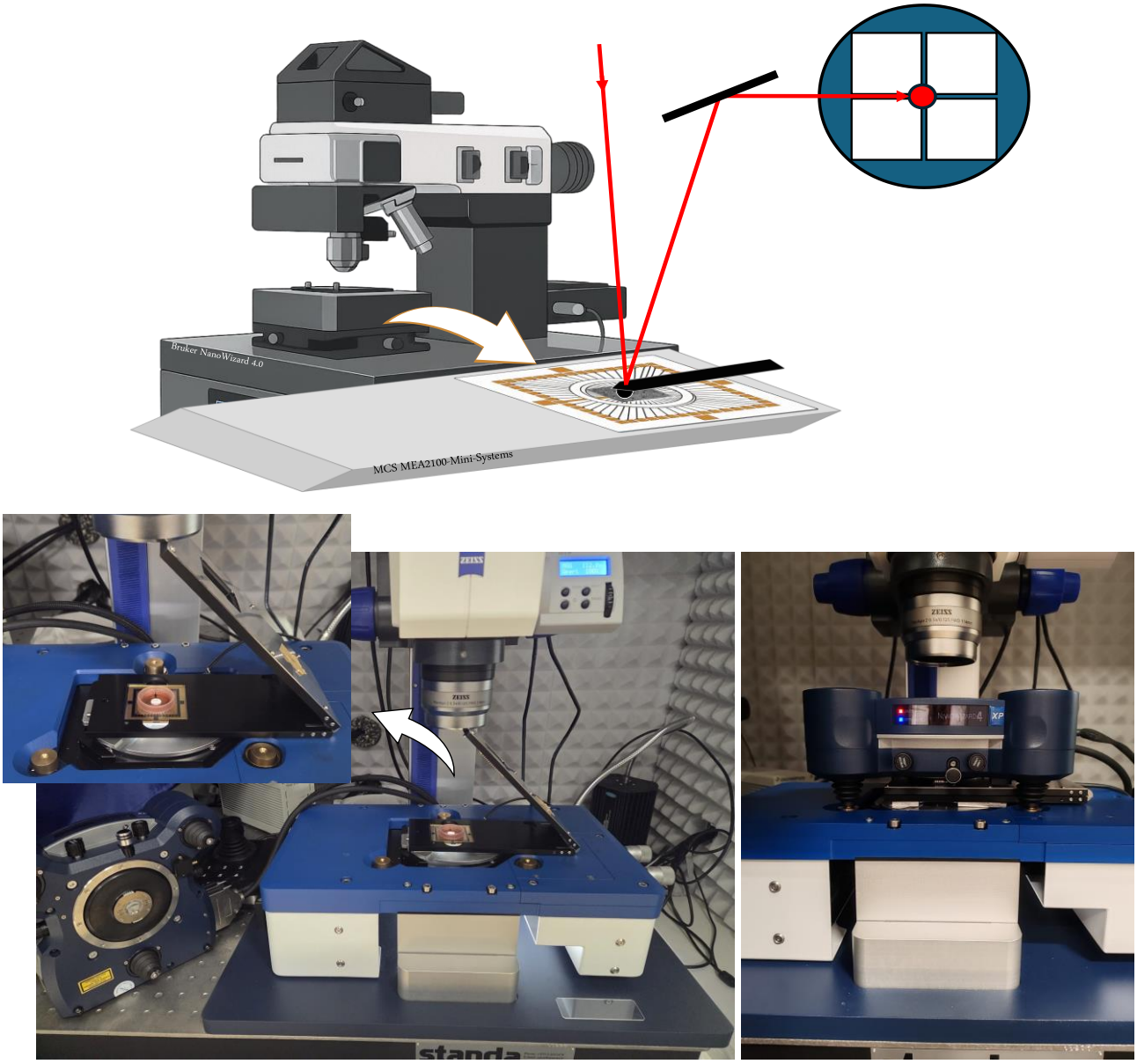


**Fig 2.1 Schematic representation (top) and photographic images (bottom) of the AFM–MEA experimental platform.** The system integrates an upright optical microscope for sample visualization, the atomic force microscopy (AFM) head equipped with a cantilever holder for the measurement of contractile and mechanical signals, and a MEA2100-Mini-System (Multichannel Systems) for extracellular electrical recordings. The microelectrode array (MEA) is positioned within the Mini-System headstage, while the AFM head is aligned above it to enable simultaneous measurements. The entire setup is mounted on a vibration isolation table to minimize mechanical noise and ensure measurement stability.

*2. Experimental Procedure*

During the experiment, the AFM cantilever is brought into contact with a cell of interest to perform mechano-contractile measurements, while the electrical activity of the same cell is simultaneously recorded by the underlying MEA electrode. Using a single controller, signals from both the MEA and the AFM can be synchronized:

- The MEA2100-Mini-60-System records extracellular potentials;
- The AFM provides signals related to the cantilever's vertical position and deflection.

**System Calibration**

At the beginning of each experimental session, the AFM is calibrated:

- The spring constant of the cantilever is determined.
- The sensitivity of the optical deflection detection system is determined: it is measured by acquiring a map of force–distance curves on a rigid substrate (Petri dish), under the same conditions as the experimental measurements (curves performed in culture medium, at a temperature of 37 °C).

**Sample Preparation**

After the calibration process, the cell sample is transferred from the incubator to the experimental setup, where measurements are performed, and the cantilever is brought into contact with the culture medium. The system is then left to equilibrate for approximately 5 minutes, allowing the cells to acclimate to the new environment and for all components to reach stable conditions. This step ensures thermal and mechanical stabilization of the cantilever, minimizing drift due to expansion or relaxation and reducing noise in the acquired signals, thereby improving measurements stability and reproducibility. Subsequently, cell viability is assessed through optical inspection using the integrated microscope.

**Experimental Measurements**

Once stabilization of all experimental components is confirmed, the actual measurements can begin.

a) Acquisition and recording of 1 minute of baseline electrical activity: This step allows the assessment of the electrophysiological health status of the cells, verification of background noise levels (in case of high noise, cleaning of the electrical contacts may be performed), and identification of the electrodes with the best signal-to-noise ratio (SNR) to be used for subsequent combined measurements.

b) Integration of optical and electrical information: Guided by both optical and electrical data, the sample is repositioned using piezoelectric motors that control movement along the

xy-plane. This allows the AFM cantilever to be accurately aligned above the selected cell/electrode from which the signal will be acquired.

c) Cell targeting and contact: Once the cell is chosen, the cantilever is brought into contact with it by means of the piezoelectric actuator controlling the cantilever's position along the Z-axis. At this point, the different acquisition modes, described below, can be carried out.

*3. Acquisition Modes*

The electrical (MEA) and contractile–mechanical (AFM) signals are simultaneously recorded throughout all acquisition modes. Specifically, the MEA signal is acquired at a sampling frequency of 10 kHz.

The AFM measurements, summarized in Fig 2.2, can be summarized as follows:

1. **Amplitude**: The cantilever is brought into contact with the target cell in "Contact Mode", and the minimum setpoint is applied to ensure stable contact with the cell surface during the contractile cycle, while minimizing cell indentation so as to perturb its activity as little as possible. Thanks to the feedback system, and by appropriately adjusting the feedback gains (IGain and PGain), it is possible to monitor the cell's contraction pattern over time by recording the vertical movement of the piezoelectric actuators that control the cantilever' position along z-axis, therefore tracking changes in the cell's height during its activity. Once the cantilever is positioned on the cell, the signal from the piezoelectric actuator is acquired (fs = 10 kHz). Real-time visualization of this signal in both the AFM and MCS software allows verification of signal quality, enabling adjustments to the feedback gains and, if necessary, to the cantilever's position on the cell (lifting, repositioning, and lowering it again) until a signal with a good SNR is obtained. After identifying the optimal position and the most suitable measurement parameters, the cantilever's placement on the cell is documented by acquiring an optical image, which serves as a reference for any subsequent measurements. The actuator signal is then recorded for a duration of 1 minute, after which the cantilever is lifted by a few micrometers (5 µm) to proceed with the second acquisition mode;
2. **Contraction**: the cantilever is pressed onto the cell in "Contact Mode", using a setpoint value sufficient to counteract the cell's vertical displacement during contraction and to sense the force it exerts. By pressing the cantilever onto the cell, the cell's contraction induces a vertical deflection of the cantilever, which is recorded by the optical detection system. The cantilever bends in response to the contraction force (F), which can be

calculated from the vertical deflection (x) multiplied by the cantilever's spring constant (k), according to Hooke's law. During this type of measurement, the feedback system that normally adjusts the vertical position of the cantilever in response to interaction forces with the substrate, is disabled. Specifically, once the cantilever is brought into contact with the cell of interest at the chosen set point, the feedback gains (IGain and PGain) are set to zero. In this way, the cantilever maintains its vertical position and is deflected by the cell without repositioning itself. The vertical deflection signal of the cantilever is continuously monitored through real-time visualization and is recorded for 1 minute (fs = 10 kHz) . Afterward, the cantilever is lifted again by 5 μm from the cell surface to proceed with the third and final acquisition mode;

3. **Mechanical**: Thanks to the "Force Spectroscopy Mode", a map of force–distance curves is generated at a specific point on the cell through indentation measurements, from which various mechanical properties of the cell of interest (e.g., viscoelasticity, stiffness, adhesion) can be derived. By simultaneously recording the cantilever's vertical position signal, as well as the extracellular field potential signal, the extracted mechanical parameters can be synchronized with the electrical activity, allowing meaningful correlations to be established. The force–distance curves are acquired over an extremely small area and can therefore be considered as point measurements. Acquisition parameters are selected to ensure an adequate level of cell surface indentation, while avoiding interference with the cell's natural contraction. A balance must also be maintained between several factors: the number of curves acquired between successive contractions, the ability of the cantilever to fully detach from the cell between consecutive curves, and a sufficiently high acquisition speed to allow the complete map of curves to be recorded within a relatively short time frame; this ensures that the sample does not remain outside the incubator for too long, thereby preserving its viability and stability.

*4. Data Analysis*

The parameters of interest (Fig 2.3) were extracted by analyzing the various signals acquired through MEA and the different AFM acquisition modes, using a custom-developed code in MATLAB (The MathWorks, Natick, MA, USA), specifically designed ad hoc to analyze synchronous electrical and mechano-contractile recordings.

Below, the extraction method of all parameters of interest, derived from the different types of acquired signals, will be briefly presented.

Electrophysiological parameters

The analysis of the extracellular field potential signal (acquired via MEA during all three AFM mechano-contractile acquisition modes) enables extraction of the following parameters. From the extracellular potential signal, cardiac events are identified, and for each beat the maximum and minimum peaks of the depolarizing phase are detected using a threshold defined as:

$$Threshold = N * std\ (signal_{10})$$

where $N$ is a multiplicative factor, $std$ is the standard deviation of the signal, and $signal_{10}$ represents the first 10 seconds of the recording.

For each event, the time instants of the maximum and minimum peaks $(t_{MAX}, t_{MIN})$ and their amplitudes $(Maxima, Minima)$ are extracted.

From this point on, unless otherwise specified, the index $i$ will be defined as follows:

$$i = 1{:}\, length(t_{MAX})$$

**Inter Beat Interval (IBI)**: This parameter is obtained by calculating the time interval between one cardiac event/beat and the next, i.e., between two consecutive depolarizing maximum peaks $(t_{MAX})$. It is computed for each cardiac event $i$ detected throughout the whole duration of the electrical recording, as follows:

$$IBI(i) = t_{MAX}(i+1) - t_{MAX}(i), \text{ with } i = 1{:}\, length(t_{MAX}) - 1.$$

**Peak-to-Peak Amplitude (PPA)**: The amplitude of the field potential is defined for each cardiac event $i$ as the difference between the maximum and minimum of the depolarization phase $(PPA(i) = Maxima(i) - Minima(i))$**.** For each $Maxima$, the corresponding $Minima$ is searched within a time window from $t_{MAX}$ to $(t_{MAX} + DEP)$. The meaning and extraction of $DEP$ parameter are described below.

Three additional key time points are identified for the extraction of subsequent electrical parameters of interest. The start and end instants of the cellular depolarization wave are extracted as follows:

- $Start\ of\ depolarizing\ wave\ (t_{start})$: corresponds to the onset of the rising phase of the positive peak of the depolarizing wave, detected by determining the instant when the signal derivative changes sign relative to the baseline. For each cardiac event $i$, this value is searched within a short time window before $t_{MAX}(i)$. This instant is also referred to as the “Q point”, due to its similarity with the depolarization wave detected in electrocardiogram (ECG) traces, and corresponds to the opening of sodium channels $(Na^+)$ marking the onset of cellular depolarization.

- $End\ of\ depolarizing\ wave\ (t_{end})$: corresponds to the end of the rising phase following the negative peak of the depolarizing wave, detected by identifying the instant when the signal derivative changes sign relative to the baseline value. For each cardiac event $i$, this value is searched within a short time window after $t_{MIN}(i)$.

Using these two temporal instants, $t_{start}$ and $t_{end}$, the following parameter is defined.

**Depolarization Duration (DEP)**: for each cardiac event $i$, this parameter is calculated as the time interval between $t_{start}(i)$ and $t_{end}(i)$. The DEP parameter is analogous to the QRS complex in an electrocardiogram.

The instant marking the end of the extracellular potential for a cardiac event is then extracted. It corresponds to the positive repolarization wave caused by the efflux of potassium ions ($K^+$) from the cell.

This wave is often referred to as the "T wave", by analogy with the repolarization wave observed in ECG traces. For each cycle, its maximum is searched within a time window defined as follows:

$$Window_i = \ t_{start}(i+1) - t_{end}(i),\ with\ i = 1{:}\ length(t_{MAX}) - 1$$

By searching for the maximum of $Signal(Window_i)$, both the amplitude of the repolarizing T wave, $T_{wave}(Amplitude)(i)$ and its timing, $T_{wave}(Time)(i)$ are extracted.

**Field Potential Duration (QT)**: This parameter represents the duration of the electrical field potential of a cardiac event, associated with the duration of the cardiac event detected via electrocardiogram (ECG), and is often referred to as the "QT segment." It is calculated for each cardiac event $i$ as the time interval between the start of depolarization and T wave peak: $QT(i) = \ t_{start}(i)$ - $T_{wave}(Time)(i)$.

**Depolarization Speed**: This parameter is analogous to the rising velocity of the cellular action potential and is calculated as the maximum slope of the rising phase of the positive depolarization peak. For each cardiac event $i$, it is calculated as the maximum derivative of the signal between the Q point ( $t_{start}(i)$) and the maximum depolarization peak ($t_{MAX}(i)$).

Contractile parameters

The analysis of the vertical displacement signal of the piezoelectric actuator controlling the cantilever position along the z-axis, acquired in the AFM "***Amplitude***" mode, enables extraction of the "Contraction Amplitude" parameter.

The signal, initially acquired in Volts (V), is converted into displacement (μm) according to the following formula:

$$\mathrm{um} = (-3) * \mathrm{V} + 15$$

**Contraction Amplitude**: this parameter, defined as the maximum signal amplitude relative to the baseline, provides for each cardiac event $i$, the amplitude of the maximum cell displacement during contraction, $Height(i)$.

Similarly, analysis of the cantilever vertical deflection signal acquired in the AFM "*Contraction*" mode allows extraction of the following parameters.

First, the deflection signal $(x\ [nm] = V * sensitivity\ [nm/V])$ is converted into a force signal $(F\ [nN])$ using the known cantilever spring constant $(k\ [nN/nm])$ and Hooke's Law $(F = k * x)$. Subsequently, the peaks corresponding to individual cardiac events are then identified. Each event is then characterized by extracting the maximum amplitude of the signal and its occurrence time, denoted as $Maxima\_Amplitude_{Force}(i)$ and $t_{MAX}\_Force(i)$, respectively.

From this point onward, unless otherwise specified, the index $i$ is defined as follows:

$$i = 1{:}\, length(t_{MAX}\_Force)$$

**Inter Beat Interval (IBI)**: calculated as the time between consecutive contraction peaks. It is computed for each cardiac event $i$ detected throughout the entire duration of the contractile recording $(IBI(i) = t_{MAX}\_Force(i+1) - t_{MAX}\_Force(i)$, with $i = 1{:}\, length(t_{MAX}\_Force) - 1)$.

Two additional significant time instants are identified, allowing the extraction of the subsequent parameters of interest.

- *Contraction onset* $(\mathrm{t\_Contr_{start}})$: the time instant corresponding to the beginning of the rising phase of the contractile event is extracted. For each cardiac beat $i$, within a short time window preceding $t_{MAX}\_Force(i)$, the instant at which the signal derivative changes sign with respect to the baseline is identified $(= \mathrm{t\_Contr_{start}})$.
- *Contraction end* $(\mathrm{t\_Contr_{end}})$: the time instant corresponding to the end of the falling phase of the contractile event is extracted. For each cardiac beat $i$, within a short time window following $t_{MAX}\_Force(i)$, the instant at which the signal derivative changes sign with respect to the baseline is identified $(= \mathrm{t\_Contr_{end}})$.

**Refractory Period ($t_{REF}$):** this parameter represents the time interval between the end of one contraction and the onset of the next, and is calculated as $\mathrm{t}_{REF}(i) = \mathrm{t\_Contr_{start}}(i+1) - \mathrm{t\_Contr_{end}}(i)$, with $i = 1{:}\, length(t_{MAX}\_Force) - 1$.

**Contraction Force Amplitude**: this is the maximum amplitude of the acquired signal relative to the baseline. For each cardiac event $i$, it is obtained by evaluating the maximum amplitude of the cellular contraction force signal, $Maxima\_Amplitude_{Force}(i)$.

**Contraction Force Duration**: this parameter is calculated as the *Full Width Half Maximum* (*FWHM*). For each event $i$, the time point corresponding to half of the maximum amplitude

are identified on the rising ($t\_Up_{50\%}(i)$) and falling ($t\_Down_{50\%}(i)$) phases of the signal, and their difference is computed: $FWHM(i) = t\_Down_{50\%}(i) - t\_Up_{50\%}(i)$.

**Contraction Force Velocity**: the $Maxima\_Velocity_{Force}(i)$ is defined as the maximum slope of the rising phase of the force signal. For each cardiac event $i$, it is obtained by computing the derivative between $\mathrm{t\_Contr_{start}(i)}$ e $t_{MAX}\_Force(i)$ and extracting its maximum value.

Electro-contractile Coupling

**Electro-Contractile Coupling ($\mathbf{EC\_Coupling}$)**: this parameter is defined as the time interval between the peak of the electrical activity and the peak of the contractile activity. For each cardiac event $i$, it is calculated as the difference between the time of the maximum depolarization peak of the extracellular field potential [$t_{MAX}(i), Maxima(i)$]*)* and the time of the maximum contraction force peak [$t_{MAX}\_Force(i),\ Maxima\_Amplitude_{Force}$]).

Accordingly, the electro-mechanical coupling is expressed as:

$$EC\_Coupling(i) = t_{MAX}\_Force(i) - t_{MAX}(i)$$

Mechanical properties

The electro-mechanical parameter **Young Modulus Temporal Behavior** was obtained by combining data from MEA electrical recordings and AFM indentation measurements acquired in "***Mechanical***" mode (Fig 2.4).

This integrated approach enables reconstruction of the temporal evolution of cellular stiffness during the cardiac cycle and its direct correlation with electrical activity.

- AFM Signal Analysis

Force–distance (F–D) curve maps were analyzed using the **JPKSPM Data Processing** software, which allows visualization, quality assessment of the acquired curves, verification of indentation depth, and application of mathematical contact models. In this study, the Derjaguin–Muller–Toporov (DMT) model was used—an extension of the Hertz model that also accounts for attractive tip–sample forces [133].

This model makes the same assumptions as the Hertz model [134] (infinitely thick, isotropic, homogeneous, and purely elastic sample), but additionally accounts for attractive forces acting between the tip and the sample.

Knowing the mechanical characteristics of the cantilever and tip (e.g., spring constant, tip radius), the DMT model can be applied and used to fit each acquired force–distance curve, extracting the mechanical parameters of interest. Each parameter is thus estimated for all successfully analyzed curves (N = # pixels), generating a structured dataset whose size corresponds to the total number of valid curves acquired during the experiment.

- Combined Signal Analysis (MEA + AFM)

To correlate electrical and mechanical signals, a custom MATLAB script was developed. The objective of this analysis was to reconstruct the temporal evolution of the mechanical parameter within a representative cardiac cycle. This was achieved by synchronizing the AFM-derived mechanical measurements with the electrical activity recorded by the MEA system. The procedure consisted of three main steps:

a) Electrical Signal Analysis (MEA)

The electrical data is analyzed as previously described. From the extracellular electrical signal, time instants associated with characteristic electrical events (e.g., $t_{MAX}$) are identified. These instants are denoted as $t\_Beat(i)$ and mark the beginning of each cardiac cycle.

b) Mechanical Signal Analysis (AFM)

From the piezoelectric actuator displacement signal (Z-position) recorded during F–D curve acquisition, local maxima ($Max\_Piezo$) and minima ($Min\_Piezo$) are identified, corresponding respectively to the positions of maximum retraction and maximum extension (indentation) of the cantilever. Each max–min pair identifies a single acquisition cycle, corresponding to one F–D curve. For each max-min pair, an intermediate point approximating the instant of first contact between the AFM tip and the sample, was calculated as: $t\_Contact(i) = Min\_Piezo(i) + 0.3125(Max\_Piezo(i) - Min\_Piezo(i))$.

This time is taken as the reference time for the corresponding F–D curve, serving as a temporal marker indicating when that curve was acquired (during the electrical signal recording).

Since each F–D curve is subsequently fitted with the DMT model to extract the mechanical parameters, each $t\_Contact(i)$ can be associated with the corresponding mechanical parameter value obtained from the fitting. The result of this procedure is a dataset composed of N (= # pixels = # F–D curves) mechanical parameter values, each linked to a specific time instant during the field potential recording; a time-resolved dataset of mechanical properties.

c) Electro-Mechanical Remapping (MEA + AFM)

To relate mechanical parameters to the cardiac cycle, a temporal remapping procedure was implemented, allowing representation of mechanical parameter as a function of the cardiac cycle. From the MEA electrical signal, the time instants marking each beat ($t\_Beat(i)$) are extracted, while from the AFM piezoelectric actuator signal, the contact times ($t\_Contact(i)$) associated with each F–D curve are obtained. From these two time series, each curve was assigned a relative time within the cardiac cycle:

$$tnew(i) = t\_Contact(i) - t\_Beat(i)$$

Through this procedure, each mechanical parameter is projected onto a time axis referenced to the cardiac cycle. All curves acquired over multiple beats are therefore remapped within a single representative cardiac cycle, defined by the interbeat interval (IBI) closest to the median value ($IBI_{Representative} = IBI \approx median(IBI)$). In this way, data acquired across multiple beats are combined into a continuous description of mechanical dynamics, showing how mechanical properties vary throughout a heartbeat, from the beginning to the end of the cycle.

To ensure the validity of the remapping procedure, several conditions must be satisfied:

- ✓ Stability and Regularity of the Electrical Signal

  The recorded electrical signal must display a stable rhythm and low inter-beat variability (expressed by a coefficient of variation, $CV\ (IBI) = \frac{std(IBI)}{mean(IBI)} < 0.3$). This requirement is essential to assume that consecutive cardiac cycles are temporally comparable and can be superimposed to generate a representative cycle. If the duration of the extracellular field potential varied significantly between beats, it would be impossible to correctly align mechanical parameters with corresponding electrical events. Thus, electrical signal stability is a necessary condition to define a representative cardiac cycle onto which all mechanical data can be projected.

- ✓ Consistency of Mechanical Properties Across Successive Cycles

  It is assumed that the cell's intrinsic mechanical properties remain stable during the acquisition time window. This assumption is reasonable since the measurement duration is short enough to exclude structural or physiological changes in the cell (such as fatigue, cytoskeletal alterations, or volume variations). This condition allows each force–distance curve to be treated as an independent observation of the same mechanical system, at a different instant of the cardiac cycle.

- ✓ Coherence of Parameter Values at Equivalent Relative Instants

  It is further assumed that curves acquired at equivalent relative instants within different cardiac cycles (e.g., at 30% of the cycle duration) yield comparable mechanical parameter values. In other words, a mechanical event that always occurs at the same cycle phase, should correspond to similar parameters regardless of the beat number.

  This assumption allows the integration of data acquired over multiple beats into a single continuous representation of the mechanical dynamics.

  Under these assumptions, the remapping procedure allows reconstruction of a complete electro-mechanical trace, describing stiffness evolution over the cardiac cycle.

d) Extraction of dynamic Young's modulus parameters

Following the electro-mechanical remapping procedure described above, the temporal evolution of Young's modulus within a representative cardiac cycle was reconstructed.

To improve signal robustness, the reconstructed trace was smoothed using a moving median filter (to remove outliers), followed by a moving average filter (to reduce noise). The resulting profile typically exhibits a bell-shaped behavior, reflecting the cyclic modulation of cellular stiffness during contraction and relaxation (Fig 2.5).

From this profile, four quantitative descriptors were extracted:

**AUC (Area Under Curve)**: area under the Young's modulus curve above the baseline ($YMbaseline = YMmin$).

**ΔStiffness**: difference between the maximum ($YMmax$) and minimum ($YMmin$) Young's modulus values within the cycle. $\Delta Stiffness = YMmax - YMbaseline$

**YM-Max**: maximum value of the Young's modulus within the cardiac cycle.

**ΔTime**: time interval between the electrical peak and the maximum Young's modulus

These parameters provide quantitative descriptors of the temporal modulation of cellular stiffness during the cardiac cycle.

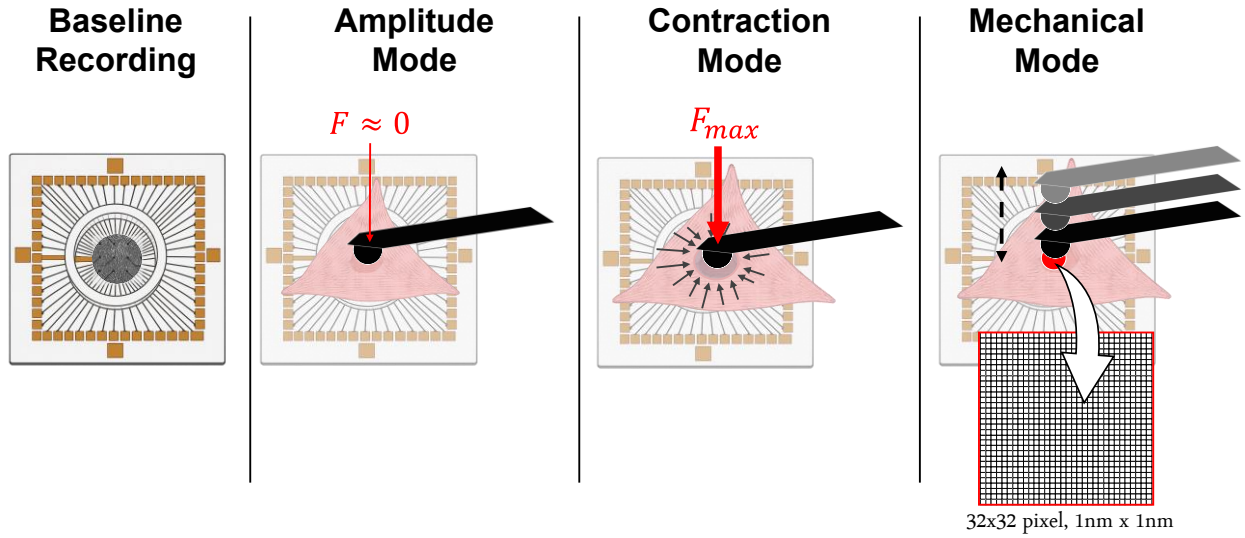


**Fig 2.2 Overview of the acquisition workflow of the AFM–MEA platform**. From left to right: baseline recording, amplitude mode, contraction mode, and mechanical mode. The baseline recording consists of a 1-minute acquisition of extracellular electrical activity to assess cell electrophysiological status and ensure optimal signal quality. During all AFM acquisition modes, electrical (MEA) and mechanical signals are recorded simultaneously from a single cell for 1 minute. In *Amplitude* mode, the cantilever is maintained in contact with the cell with minimal force ($F \approx 0$) to monitor variations in cell height associated with contraction. In *Contraction* mode, the cantilever is pressed against the cell ($Fmax$) to measure the force generated during contraction. In *Mechanical* mode, force spectroscopy is performed to obtain force–distance curves over a localized region of the cell, enabling the extraction of the cell's mechanical properties.

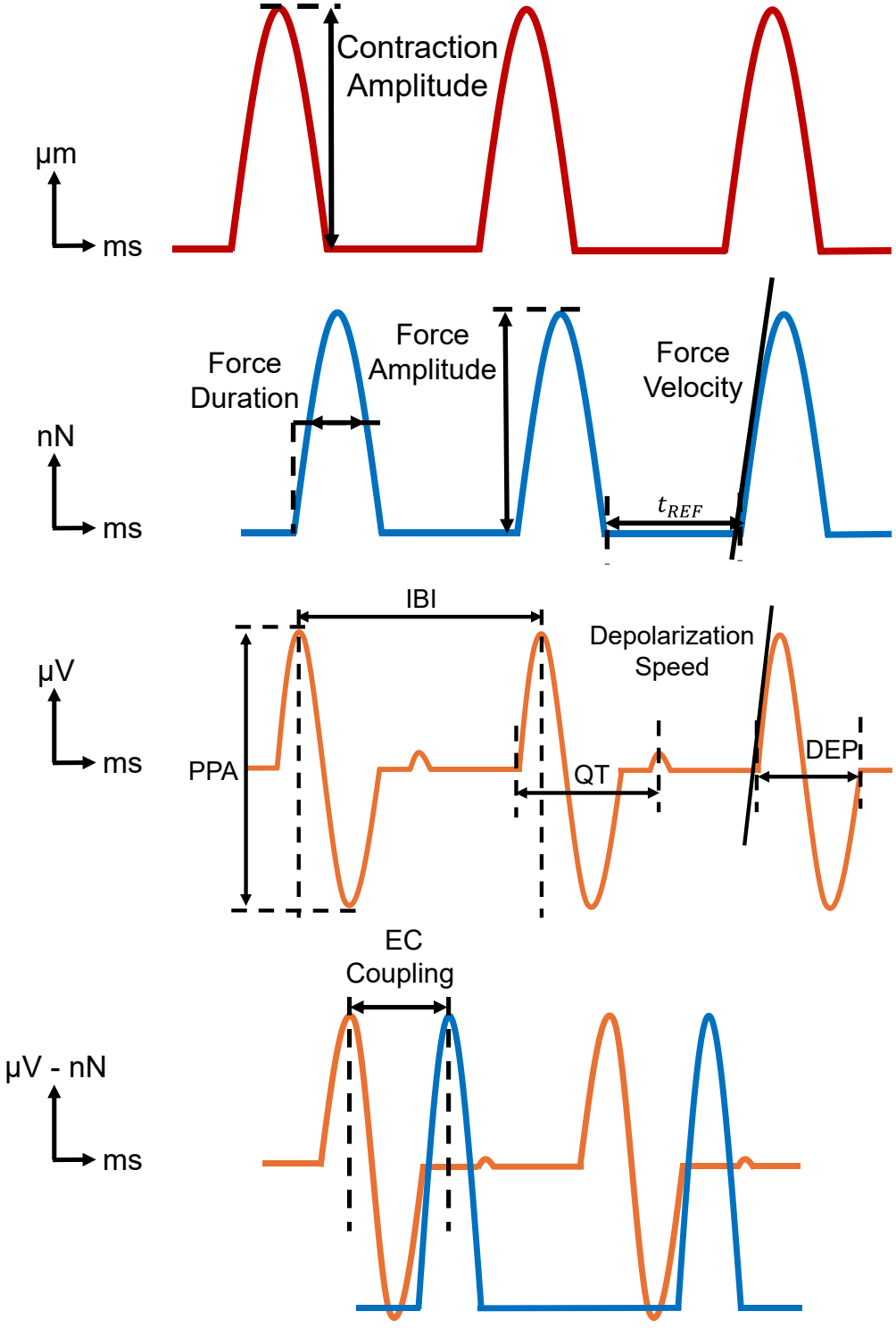


**Fig 2.3 Representative signals acquired from the AFM–MEA platform and corresponding extracted parameters**. The red trace represents amplitude measurements obtained in Amplitude mode, from which the contraction amplitude is derived. The blue trace shows the contractile force signal recorded in Contraction mode, enabling the extraction of parameters such as contraction force amplitude, duration, and velocity and refractory period ($t_{REF}$). The orange trace corresponds to extracellular electrical activity recorded by the MEA, from which electrophysiological parameters including peak-to-peak amplitude (PPA), inter-beat interval (IBI), field potential duration (QT), and depolarization speed and duration (DEP) are obtained. The combined analysis of electrical and contractile signals (bottom panel) enables the extraction of the electro-contractile coupling (EC-Coupling) parameter.

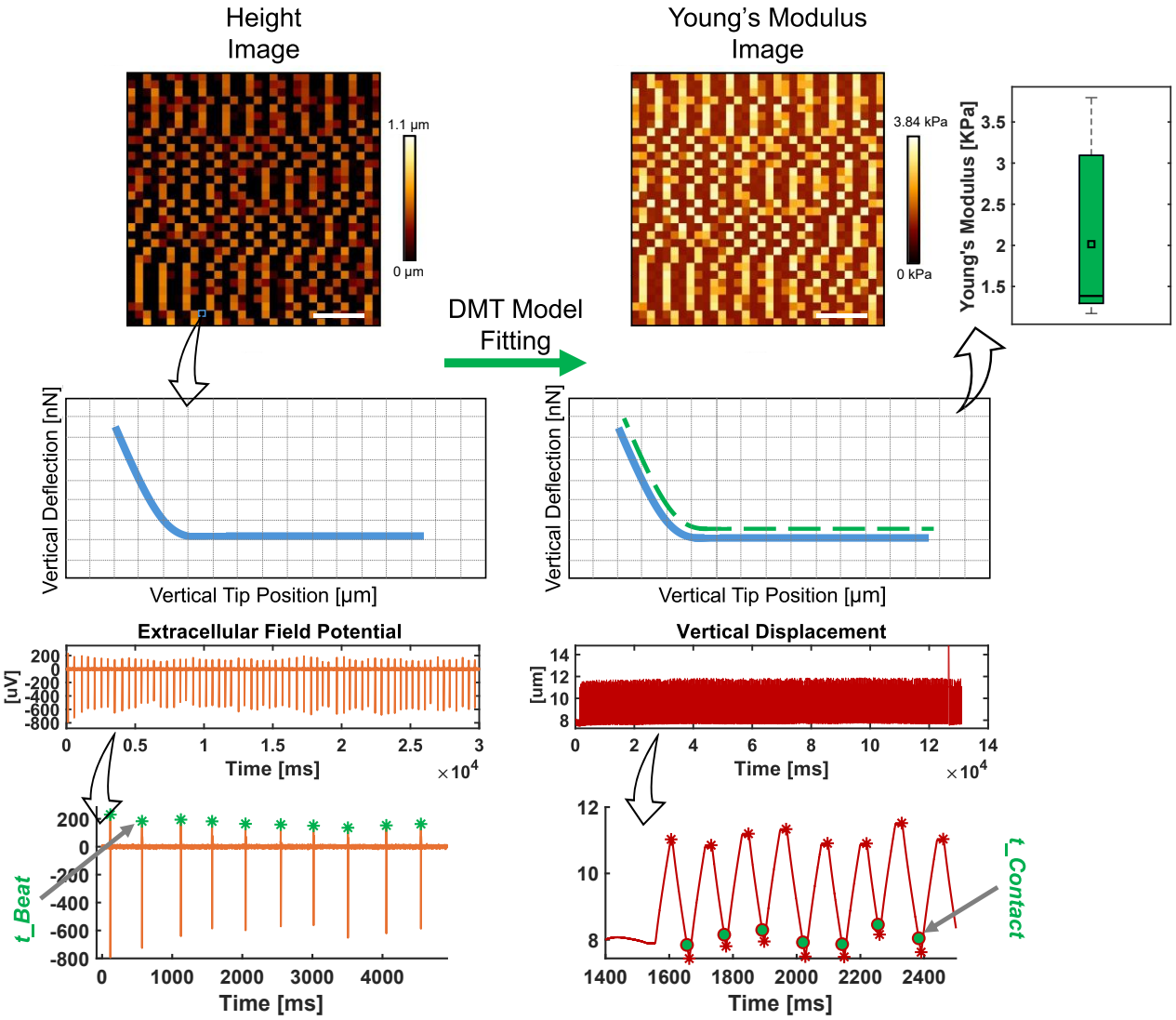


**Fig 2.4 Workflow for the extraction and temporal reconstruction of mechanical properties from AFM measurements and their integration with MEA electrical recordings**. AFM force–distance curves acquired in Mechanical mode over a highly localized region (1 nm × 1 nm), consisting of 1024 curves, are processed and fitted using the DMT model to extract Young's modulus mechanical parameter, generating spatial maps. Scale bar = 200 pm. The inset boxplot shows the distribution of Young's modulus values extracted from all fitted curves, where each point corresponds to an individual curve and the black square indicates the mean value (top). The corresponding force–distance curves and model fitting are shown (middle). Electrical activity recorded by the MEA (field potential) and AFM cantilever vertical displacement signals are analyzed to identify characteristic time points, such as t_Beat and t_Contact (bottom). By synchronizing electrical and mechanical data, each measurement is temporally mapped within a representative heartbeat, enabling the reconstruction of the temporal evolution of cellular stiffness and its correlation with electrical activity.

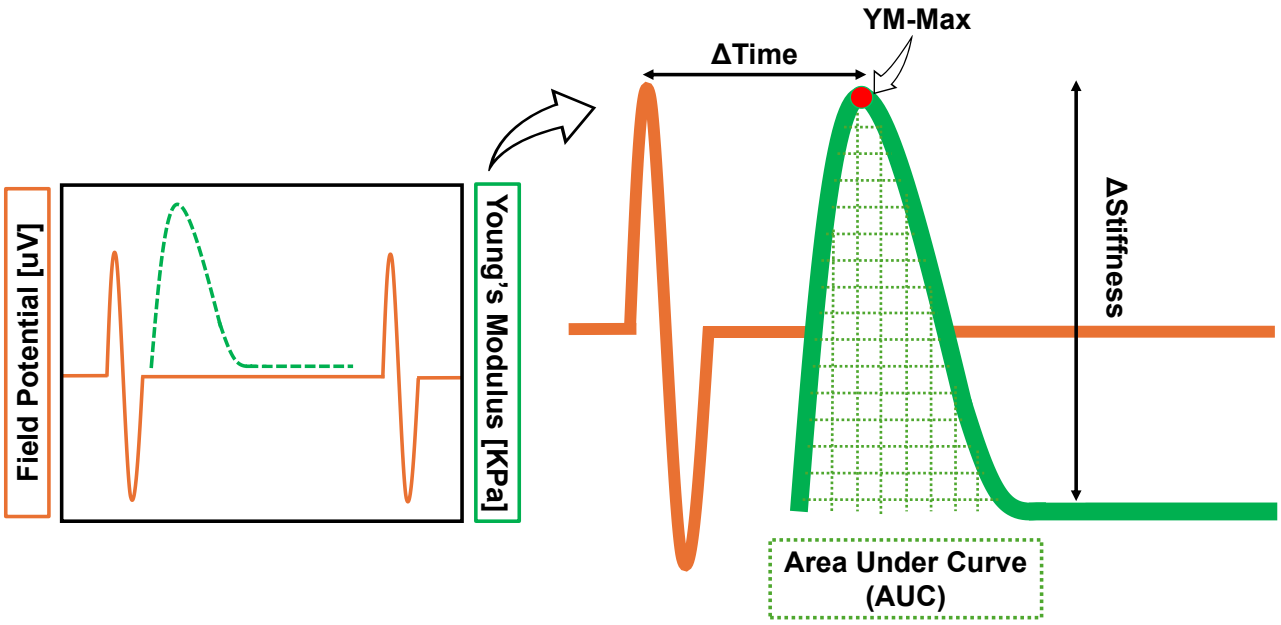


**Fig 2.5 Extraction of dynamic Young's modulus parameters from the reconstructed temporal profile of cellular stiffness during a representative cardiac cycle**. The Young's modulus exhibits a bell-shaped behavior associated with contraction and relaxation phases and is temporally aligned with the extracellular electrical signal. From this profile, four quantitative descriptors are extracted: the maximum Young's modulus (YM-Max), the stiffness variation (ΔStiffness), defined as the difference between maximum and baseline values (define as the as the minimum Young's modulus value within the cycle), the time delay (ΔTime) between the electrical peak and YM-Max, and the area under the curve (AUC), representing the overall modulation of stiffness during the cardiac cycle.

### 2.1.3 Application of the Experimental Platform

The following experiments were performed to illustrate the capability of the integrated AFM–MEA platform to provide stable and reproducible simultaneous measurements of electrical, contractile, and mechanical activity in individual cardiomyocytes. The combined approach allows a comprehensive characterization of cardiomyocyte function by directly correlating electrical excitation with contractile activity and biomechanical properties at the single-cell level.

Before discussing the physiological significance of the extracted parameters, representative recordings are presented to illustrate the acquired signals and their temporal correlation as well as the ability of the system to monitor the same cell across different experimental sessions.

*Simultaneous recording of the electrical and contractile activity*

Fig 2.6 shows representative simultaneous recordings of the extracellular field potential and contraction signals obtained using two different AFM-based acquisition modes.

The extracellular potential signal reflects the depolarization–repolarization cycle of the cell, while the AFM signals provide complementary information about its contractile activity. In “Amplitude” mode, the cantilever remains in gentle contact with the cell surface while the feedback loop maintains a constant (minimal) interaction force. Under these conditions, the vertical displacement of the piezoelectric actuator follows the changes in cell height associated with the contractile cycle, enabling monitoring of the “vertical contraction” amplitude (i.e. the changes in cell height due the longitudinal contraction of the cell). In “Contraction” mode, the cantilever is pushed against the cell up to a given deflection, and the feedback system is disabled. As the cardiomyocyte contracts, the resulting force bends further the cantilever, producing a deflection signal that can be converted into force taking into account the cantilever spring constant (Hooke’s law). This configuration allows the direct measurement of the contractile force generated by the cell. The simultaneous acquisition of these signals reveals a clear temporal relationship between electrical excitation and mechanical contraction. Each electrical depolarization event is followed by a corresponding contractile response, illustrating the excitation–contraction coupling process. The high signal-to-noise ratio of both electrical and contractile recordings enables precise detection of individual beats and accurate extraction of quantitative parameters.

*Longitudinal tracking of the same cardiomyocyte across different culture days*

A key feature of the experimental platform is the possibility of performing repeated measurements on the same cardiomyocyte over multiple experimental sessions, enabling single-cell measurements. The combination of optical imaging and the spatial reference provided by the microelectrode array layout enabled the AFM probe to be repositioned over the same cell during subsequent experiments (Fig 2.7).

To assess the reproducibility and temporal stability of the system, measurements were performed on the same cells across different days *in vitro* (DIV4, DIV5, and DIV6); data are presented in Fig 2.8 and in Fig 2.9.

Representative recordings acquired across different days in culture show consistent electrical and contractile activity; despite the natural biological variability associated with cardiomyocyte maturation, the morphology and temporal structure of the signals remain comparable across measurements. The possibility of tracking the same cell over time (Fig 2.10) enables the investigation of cellular maturation processes, progressive pathological alterations, and pharmacological responses, while minimizing variability arising from cell-to-cell heterogeneity.

*Dynamic mechanical characterization during the cardiac cycle*

Beyond electrophysiological and contractile measurements, the integrated platform enables the investigation of cardiomyocyte mechanical properties through AFM force spectroscopy. In particular, this approach enables the reconstruction of the temporal evolution of cellular stiffness during the cardiac cycle, providing insight into the dynamic mechanical behavior of cardiomyocytes.

During the “Mechanical” acquisition mode, force–distance curves are continuously acquired at a specific location on the cell surface while the electrical activity is simultaneously recorded. Each curve provides a local measurement of the mechanical interaction between the AFM tip and the cell membrane.

The mechanical parameters extracted from the force–distance curves, such as the Young’s modulus, are obtained by fitting the indentation portion of each curve using the Derjaguin–Muller–Toporov (DMT) contact model.

Because the force–distance curves are acquired sequentially while the cell is beating, each mechanical measurement corresponds to a specific time point within the cardiac cycle. By associating the acquisition time of each curve with the electrical reference signal obtained from the MEA, the mechanical parameters can be temporally aligned with the electrical activity.

Through the remapping procedure described in the Data Analysis section above, the mechanical parameters extracted from individual curves are projected onto a normalized interbeat interval. This approach enables the reconstruction of the temporal evolution of cellular mechanical properties during a representative cardiac cycle (Fig 2.11).

The resulting profile of the Young’s modulus reveals dynamic variations in cellular stiffness across the contraction–relaxation cycle, reflecting the changes in intracellular tension and cytoskeletal organization associated with cardiomyocyte activity.

These results demonstrate that the combined AFM–MEA system provides access not only to electrophysiological and contractile information but also offers the additional advantage of investigating the dynamic biomechanical behavior of cardiomyocytes, enabling the direct correlation of changes in cellular mechanical properties with electrical activation.

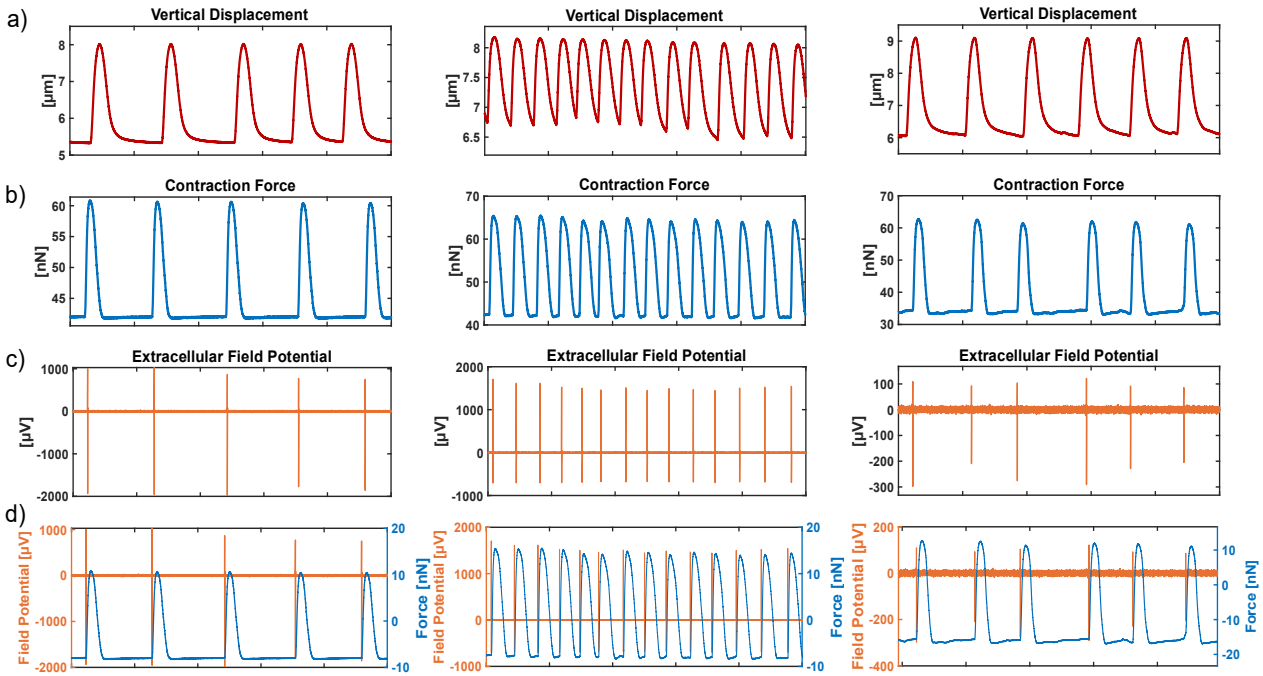


**Fig 2.6 Representative simultaneous AFM–MEA recordings acquired from three different cardiomyocytes over a 5 s time window (time axis in milliseconds)**. Each column corresponds to a different representative cell. (a) Amplitude signals obtained in Amplitude mode, reflecting variations in cell height during contraction. (b) Contractile force signals recorded in Contraction mode, representing the force generated by the cell. (c) Potentials acquired using the MEA, corresponding to the electrical activity of the cardiomyocytes. (d) Overlay of electrical (orange) and contractile (blue) signals, highlighting the temporal relationship between electrical excitation and mechanical contraction. The three cells exhibit different beating frequencies and signal amplitudes, reflecting the intrinsic variability of cardiomyocyte activity. The synchronized recordings demonstrate the capability of the platform to capture electromechanical activity with high signal-to-noise ratio and enable accurate identification of individual beats.

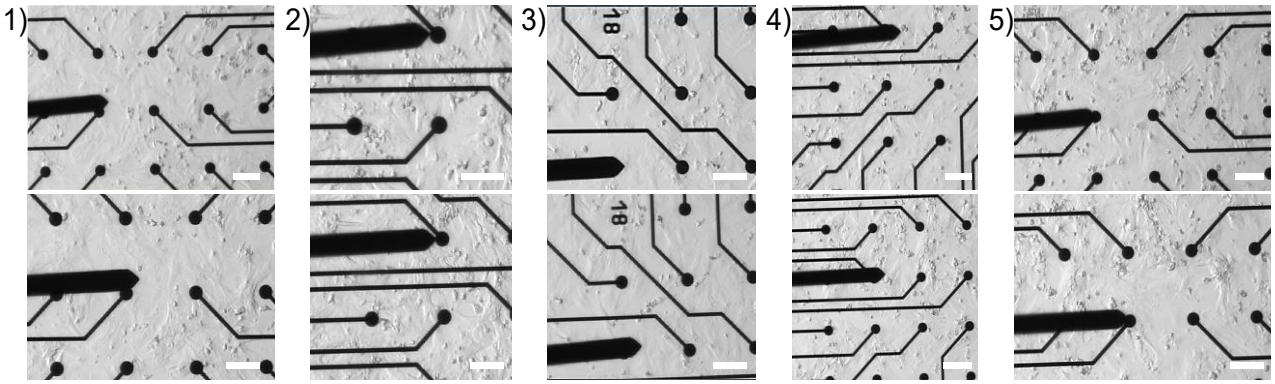


**Fig 2.7 Bright-field images showing the relative positioning of the AFM cantilever with respect to the MEA electrode for five representative cardiomyocytes (1-5)**. For each cell, images acquired at two different time points (top: first measurement day; bottom: second measurement day) demonstrate the ability to reposition the cantilever over the same cell using the MEA grid as a spatial reference. Scale bar: 100 µm.

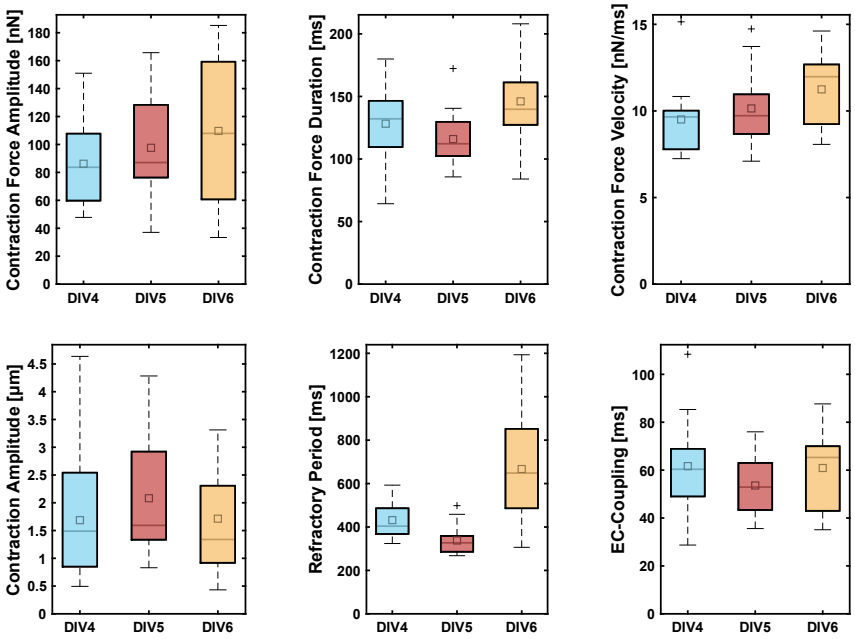


**Fig 2.8 Box plots of electrocontractile parameters extracted from 20 cardiomyocytes measured across different days in vitro (DIV4, DIV5, and DIV6).** The analyzed parameters include contraction force amplitude, contraction force duration, contraction force velocity, contraction amplitude, refractory period, and the excitation–contraction (EC) coupling time. Each boxplot represents the distribution of the parameter across all analyzed cells at a given DIV, where each data point corresponds to the mean value calculated for an individual cell after outlier removal, and the square marker indicates the mean value of the distribution. The results highlight the temporal evolution and variability of contractile and electro-contractile properties during cell maturation, supporting the capability of the platform for longitudinal monitoring of cardiomyocyte functional activity.

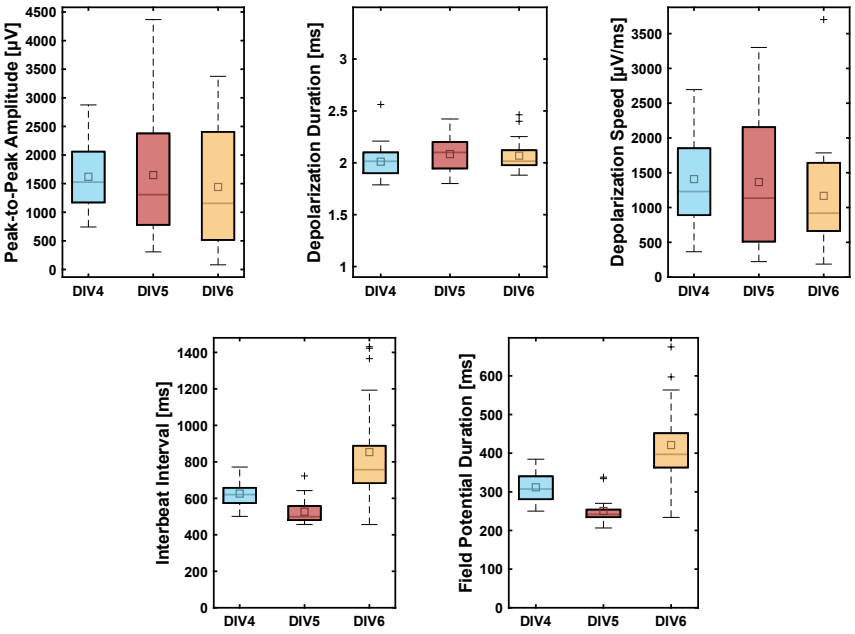


**Fig 2.9 Box plots of electrophysiological parameters extracted from 20 cardiomyocytes measured across different days in vitro (DIV4, DIV5, and DIV6).** The analyzed parameters include peak-to-peak amplitude (PPA), depolarization duration, depolarization speed (DEP), inter-beat interval (IBI), and field potential duration (QT). Each boxplot represents the distribution of the parameter across all analyzed cells at a given DIV, where each data point corresponds to the mean value calculated for an individual cell after outlier removal, and the square marker indicates the mean value of the distribution. The results highlight the temporal evolution and variability of the electrical properties during cell maturation.

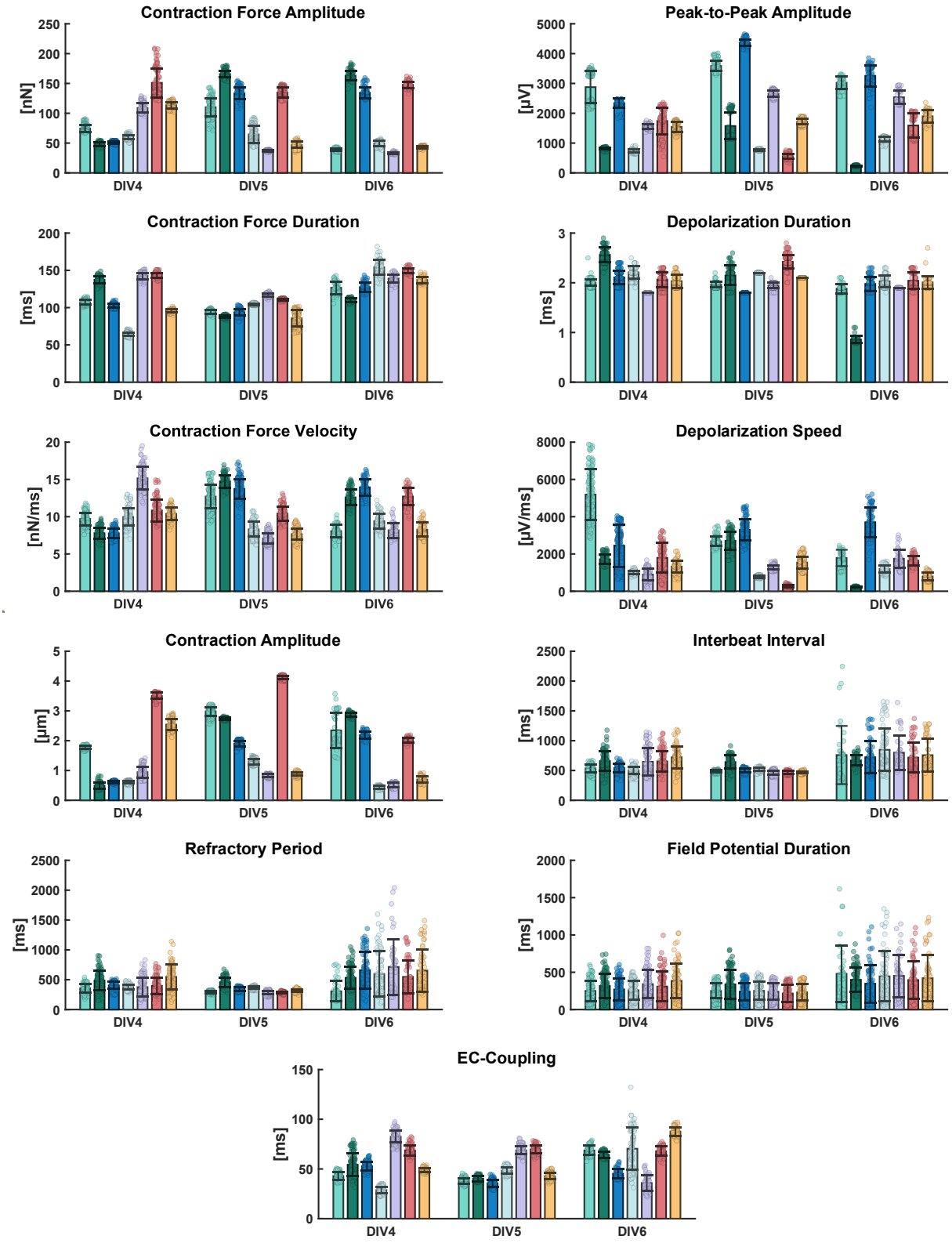


**Fig 2.10 Representation of electrocontractile and electrophysiological parameters measured in six representative cardiomyocytes across three different days *in vitro* (DIV4, DIV5, and DIV6)**. Each panel shows a specific parameter, including contraction force amplitude, contraction force duration, contraction force velocity, contraction amplitude, peak-to-peak amplitude, depolarization duration and speed, inter-beat interval, refractory period, field potential duration, and excitation–contraction (EC) coupling. For each cell, bar plots represent the mean value at each DIV (mean ± SD), with consistent color coding across time points. Individual raw data points are overlaid as dots, illustrating intra-cell variability and measurement reproducibility over time.

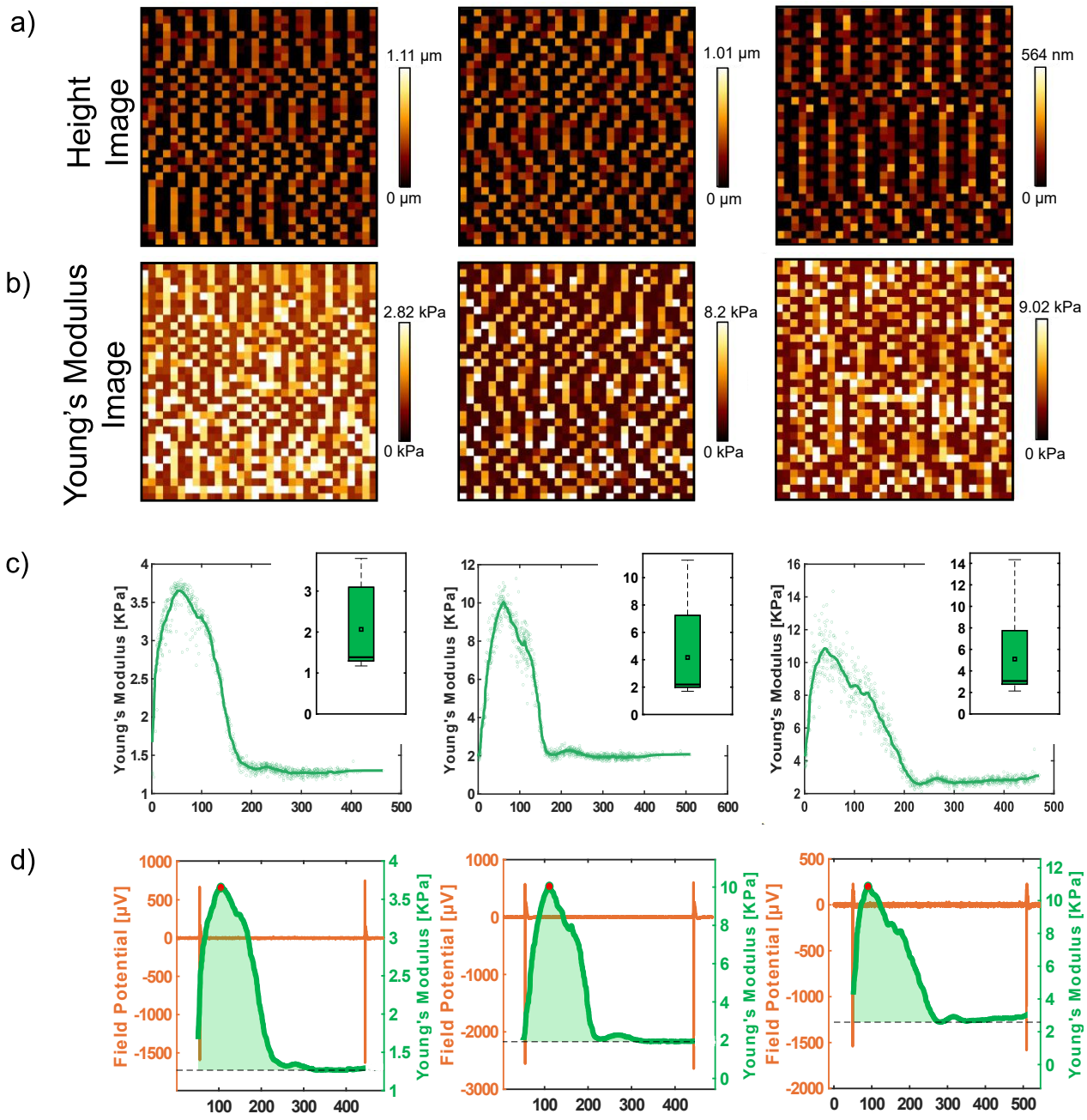


**Fig 2.11 Dynamic mechanical characterization of cardiomyocytes during the cardiac cycle based on AFM force spectroscopy**. Data from three representative cardiomyocytes are shown, with each column corresponding to a different cell. (a) Representative height maps obtained from force–distance curves acquisition over a highly localized region (1 nm × 1 nm), consisting of 1024 force–distance curves. (b) Corresponding Young's modulus maps derived from DMT model fitting of the force–distance curves. (c) Temporal evolution of the Young's modulus over a representative cardiac cycle, obtained by mapping each fitted value to its corresponding time point. Green dots denote the raw data, while the green line represents the smoothed reconstructed trace. The inset boxplot shows the distribution of Young's modulus values extracted from all fitted curves, with the black square indicating the mean value. (d) Representation of Young's modulus as a function of the inter-beat interval (IBI), highlighting the dynamic mechanical parameters that can be extracted. The results illustrate the time-resolved modulation of cellular stiffness during the contraction–relaxation cycle. X axis: time [ms].

*Integration of electrical, contractile, and mechanical parameters*

The representative recordings described above constitute the basis for the extraction of the quantitative parameters. Electrical signals provide descriptors of cardiomyocyte electrophysiological activity, while AFM measurements enable the quantification of both contractile force and biomechanical properties. By combining these complementary dataset, the integrated platform allows a multidimensional characterization of cardiomyocyte function at the single-cell level.

Table 2.1 summarizes how each parameter is derived from its corresponding signal, while the following sections describe their physiological relevance in the context of *in vitro* cardiac research, disease modeling, and pharmacological studies.

Together, these parameters collectively enable the reconstruction of the complex processes underlying excitation, contraction, and electromechanical coupling.

Each serves not only as a marker of cellular maturity and functional competence, but also as a sensitive indicator of pathological alterations and drug-induced effects. Their combined analysis provides a robust framework for disease modeling, safety pharmacology, and preclinical evaluation of novel therapeutic strategies.

Electrophysiological parameters

In *in vitro* studies, analysis of the **Interbeat Interval (IBI)** and derived **beating frequency** provides key insights into cardiomyocyte functional state. Spontaneous beating frequency is a direct reflection of cardiomyocyte maturity and functionality: a stable and reproducible rhythm indicates advanced development, whereas pronounced irregularities may suggest immaturity or electrophysiological instability. Not only the mean frequency, but also the variability of the intervals carries significant biological information. Excessive irregularity can reproduce pathological conditions such as arrhythmias or fibrillation, while persistent shifts toward higher or lower frequencies mimic tachycardia and bradycardia, respectively. For these reasons, IBI monitoring serves as a powerful tool for investigating cardiac pathologies in controlled conditions. Overall, the IBI analysis represents an integrated indicator of cardiomyocyte maturity, functional stability, and electrophysiological behavior, making it a valuable parameter for disease modeling and drug safety evaluation.

**Peak-to-peak Amplitude (PPA)** of the extracellular field potential represents the voltage difference between its negative and positive deflections, capturing the collective extracellular manifestation of cardiomyocyte depolarization and repolarization near the recording electrode. PPA is closely linked to the strength of the underlying action potential and the activity of key ion channels. Higher PPA values generally indicate robust depolarization

currents, reflecting healthy, functionally competent cardiomyocytes and an effective electrical coupling between the cell and the electrode. Conversely, reduced amplitudes may indicate impaired excitability, weaker action potentials, reduced adhesion to the substrate, or early cellular dysfunction. PPA is also sensitive to pathological and pharmacological perturbations: ion channel blockers, toxins, or stress conditions, typically reduce extracellular potential amplitude, making it a direct marker of altered cellular excitability.

The **Field Potential Duration (FPD)** represents the extracellular counterpart of the intracellular Action Potential Duration (APD) and reflects the overall duration of a cardiomyocyte's electrical activity. It extends from the opening of sodium ($Na^+$) channels, which trigger depolarization, to the closure of potassium ($K^+$) channels, marking the end of repolarization. In this way, FPD integrates both phases into a single parameter, reflecting the coordination and balance of ionic currents that regulate cellular excitability. FPD is highly relevant for disease modeling and drug screening. Its prolongation reproduces, *in vitro*, effects analogous to QT interval prolongation *in vivo*, a condition associated with an increased risk of severe ventricular arrhythmias such as Torsade de Pointes [135]. Conversely, a shortened FPD may indicate hyperexcitability or other dysfunctions, which can also be proarrhythmic. For this reason, FPD analysis is widely used to model cardiac channelopathies (e.g., Long QT syndrome) and to assess the effects of stressors such as hypoxia or electrolyte imbalance. Since many drugs can alter the duration of field potentials—particularly through interactions with potassium channels— FPD is considered a key parameter in preclinical pharmacological screening and in the evaluation of drug-induced cardiotoxicity [136],[137]. In summary, FPD is not merely a temporal measure, but an integrated biomarker of ionic function and cardiac excitability, reflects the health, maturity, and stability of cardiomyocytes under both physiological and pathological conditions.

The analysis of sodium currents is essential for understanding the initial phase of cardiomyocytes action potential. Two key parameters describing this process are **Depolarization Speed** and **Depolarization Duration (DEP)**. **Depolarization Speed** reflects the rapidity of the initial depolarization phase and is strongly dependent on the conductance and availability of sodium ($Na^+$) channels. A high upstroke velocity indicates efficient channel activation and rapid signal propagation, typical of healthy and mature cells. Conversely, a reduction may indicate cellular immaturity, the effect of sodium channel–blocking drugs, or genetic defects that impair channel function, such as those associated with Brugada-syndrome [138].

**DEP**, on the other hand, represents the duration of sodium channel activation. Under normal conditions, these channels open and inactivate rapidly; however, alterations in this timing can have important consequences. Prolonged activation may lead to persistent sodium currents and increase the risk of arrhythmias, as observed in Long QT syndrome type 3 [139]. In contrast, excessively short durations can impair proper depolarization and hinder electrical signal propagation .

In summary, depolarization speed and duration capture complementary aspects of sodium channel function - activation efficiency and temporal dynamics. Their analysis provides a robust indicator of cardiomyocyte health, maturity, and electrophysiological stability, and represents a valuable tool in pharmacological research and the study of cardiac channelopathies.

Contractile parameters

The mechanical characterization of cardiomyocytes *in vitro* provides information complementary to electrophysiological measurements, as it directly describes the cell's ability to convert electrical signal into mechanical work. Parameters such as contraction amplitude, duration and velocity are closely linked to the calcium–actin–myosin cycle and to the efficiency of electromechanical coupling.

The **Contraction Amplitude** represents the extent of cellular shortening or displacement during a contractile cycle. Experimentally, it corresponds to the vertical or lateral movement of the cell. *In vitro*, this parameter is strongly correlated with the mechanical force generated by the cell: higher amplitudes indicate stronger contractions, whereas reduced amplitudes may suggest impairment or damage of the contractile machinery.

The **Contraction Force Amplitude** quantifies the real intensity of contraction, representing the maximum force generated by the cell during a contractile cycle. This parameter reflects intracellular calcium availability, the efficiency of the actin–myosin cross-bridge cycle, and the overall energetic state of the cell.

High values indicate strong, efficient contractions characteristic of mature cardiomyocytes with well-developed contractile machinery and effective calcium handling. Reduce amplitudes may indicate cellular immaturity, impaired calcium release or reuptake, metabolic dysfunction, or structural damage.

The **Contraction Force Duration** describes how long the mechanical contraction persists and depends on intracellular calcium dynamics and actin–myosin kinetics. Abnormally short or prolonged durations may indicate altered calcium handling, typical of immature cells or pathological conditions such as cardiomyopathies.

The **Contraction Force Velocity** reflects how rapidly the cell develops force and serves as a sensitive indicator of electromechanical coupling efficiency. Fast, coordinated contractions suggest effective conversion of electrical signals into mechanical output, whereas reduced velocity may indicate impaired signal transmission, limited calcium availability, or signs of cellular fatigue.

**Refractory Period (tREF)** is the time interval between the end of one contraction and the beginning of the next. Physiologically, it corresponds to the time required for the cell to repolarize (via $K^+$ efflux) and restore its ionic balance, enabling a new depolarization ($Na^+$ influx). In other words, it defines the minimum time needed for a cardiomyocyte to become excitable and contractile again. Its duration is crucial: if too short, it may lead to hyperexcitability and increased arrhythmic risk; if prolonged, it may indicate impaired repolarization or difficulty in restoring ionic gradients, as occurs in pathological conditions that reduce recovery capacity (e.g., long QT syndromes). In *in vitro* studies, tREF is therefore an important parameter for evaluating both electrophysiological and contractile stability.

In summary, these parameters enable a comprehensive characterization of cardiomyocyte contractile function *in vitro*, making them essential tools in cardiac physiology research and preclinical studies.

Electro-contractile Coupling

Beyond individual electrical and contractile descriptors, **Electro-Contractile (EC) Coupling**—defined as the delay between the peak of the extracellular electrical signal and the peak of mechanical contraction—represents a key integrative marker of cardiomyocyte function. This latency reflects the efficiency of excitation–contraction coupling, including calcium release from the sarcoplasmic reticulum, binding to troponin, and subsequent actin–myosin cross-bridge formation. A physiological delay indicates proper synchronization between electrical activation and force generation, while prolongation may reveal impaired calcium handling, reduced contractile sensitivity, or early signs of pathological remodeling. Conversely, an abnormally short delay may reflect hyperexcitability or altered calcium dynamics, potentially predisposing cells to arrhythmic risk.

For these reasons, this temporal parameter provides insights that cannot be captured by electrical or mechanical measurements alone. When integrated with other contractile parameters, EC-Coupling offers a comprehensive evaluation of how electrical excitation is translated into mechanical output, making it a key metric for assessing cardiomyocyte maturity, calcium handling, disease modeling, and drug safety *in vitro*.

Mechanical properties

In cardiomyocytes, the analysis of mechanical properties provides valuable insights into cellular maturation, tissue health, and responses to pathological or pharmacological stimuli. Among these, the **Young's Modulus** describes cell stiffness and is directly related to cytoskeletal organization.

Analyzing its **temporal evolution** during the cardiac cycle allows the observation of stiffness changes between contraction and relaxation with high temporal resolution (Fig 2.11). This dynamic approach provides valuable insights into membrane protein dynamics and mechano-sensing mechanisms, offering not just a *static snapshot* of the cell's state but rather a *dynamic trace* of its functional status—one that more closely reflects real physiology and the pathological conditions intended to be reproduced *in vitro*.

Moreover, the reconstruction of the Young's modulus profile over time provides direct insight into the **dynamic mechanical behavior of cardiomyocytes**. Unlike static measurements of stiffness, this approach reveals how cellular mechanical properties evolve during contraction and relaxation.

The **YM-Max** is the maximum stiffness reached during the cardiac cycle, reflecting peak intracellular tension generated by the cytoskeleton and contractile apparatus. Higher values may indicate stronger mechanical engagement of the cytoskeletal network, whereas lower values may suggest impaired contractility or structural alterations.

**ΔStiffness** represent the difference between the maximum and minimum Young's modulus values within the cardiac cycle. This parameter quantifies the amplitude of stiffness modulation between relaxation and contraction, thereby reflecting the cell's dynamic mechanical responsiveness. Lower values may indicate reduce adaptability.

The **AUC (Area Under Curve)** integrates Young's modulus variations over the entire cardiac cycle, capturing the overall mechanical activity of the cell by combining magnitude and duration of cellular stiffening.

Finally, **ΔTime** is defined as the delay between the peak of electrical activation and the maximum YM value. It provides information on the timing of the electromechanical response, offering additional insight into the dynamics of excitation–contraction coupling and its efficiency at the mechanical level.

Together, these parameters provide a comprehensive description of the temporal evolution of cardiomyocyte stiffness, enabling analysis of both the magnitude and timing of mechanical responses relative to electrical activation.

| Parameter Name | Description |
|---|---|
| **Interbeat Interval (IBI)** | Time interval between one peak of the electrical/contractile signal and the next. |
| **Peak-to-Peak Amplitude (PPA)** | Amplitude difference between the maximum positive and the minimum negative peak of the extracellular field potential signal. |
| **Field Potential Duration (QT)** | Time interval between the initial depolarization peak and the subsequent repolarization wave of the extracellular field potential signal. |
| **Depolarization Speed** | Maximum derivative (dV/dt) of the rising phase of the depolarization peak of the extracellular field potential signal. |
| **Depolarization Duration (DEP)** | Time interval from the onset of the positive peak to the end of the negative peak during the depolarization phase of the extracellular field potential signal. |
| **Contraction Amplitude** | Maximum amplitude of the piezoelectric actuator displacement signal along the z-axis (“Amplitude” mode), representing the maximum vertical displacement of the cell during contraction. |
| **Refractory Period (tREF)** | Time interval between the end of one contraction and the beginning of the next one. |
| **Contraction Force Amplitude** | Maximum amplitude of the cantilever vertical deflection signal (“Contraction” mode), reflecting the maximum force exerted by the cell during contraction. |
| **Contraction Force Duration** | Time interval at half of the peak contraction force amplitude (FWHM = Full Width Half Maximum). |
| **Contraction Force Velocity** | Maximum derivative (dF/dt) of the rising phase of the contractile signal. |
| **Electro-Contractile Coupling (EC Coupling)** | Time interval between the peak of the electrical signal and the peak of the corresponding contractile signal. |
| **Mechanical Parameters Temporal Behavior** | Changes and progression of cellular mechanical properties obtained from the remapping of each force–distance curve within a single IBI. |

**Table 2.1 Summary of the electrical, contractile, and mechanical parameters extracted from AFM–MEA measurements, including their definitions and corresponding signal sources.** Electrical parameters are derived from MEA recordings, while contractile and mechanical parameters are obtained from AFM measurements, as detailed in the ‘Acquisition Mode’ section. Each parameter provides quantitative descriptors of specific aspects of cardiomyocyte activity, including electrophysiological behavior, contractile dynamics, and biomechanical properties. The integration of these descriptors enables a comprehensive, multidimensional characterization of cardiomyocyte function at the single-cell level and supports the investigation of cellular maturation, functional variability, and responses to external stimuli.

Overall, the combined analysis of electrical, contractile, and mechanical parameters enables a comprehensive characterization of cardiomyocyte functional behavior at the single-cell level. By integrating information on electrophysiology, force generation, and dynamic mechanical properties, the AFM–MEA platform provides a multidimensional framework for interpreting cardiomyocyte function. This integrated approach represents a powerful tool for investigating cardiac physiology, modeling disease-related alterations, and evaluating the effects of pharmacological compounds *in vitro*.

### 2.1.4 Discussion

This chapter presented the optimized development of an experimental platform integrating microelectrode arrays (MEA) and atomic force microscopy (AFM) for the *in vitro* investigation of cardiomyocyte electro-contractile-mechanical activity. The simultaneous acquisition of electrical and contractile signals at the single-cell level represents a significant methodological advance for the analysis of *in vitro* cardiac models. By combining electrophysiological recordings with measurements of contractile force and biomechanical properties, the platform enables a comprehensive functional characterization of cardiomyocytes, allowing the investigation of excitation dynamics, mechanical contraction, and their electromechanical coupling.

The integration of multiple experimental parameters captures distinct yet complementary aspects of cellular physiology, providing a multidimensional perspective on cardiomyocyte maturation, functional stability, and overall cellular performance. Electrical descriptors primarily reflect the activity of ion channels and ionic currents, particularly those mediated by sodium ($Na^+$) and potassium ($K^+$) ions, which govern the depolarization and repolarization phases of the action potential. Contractile parameters, on the other hand, provide insights into calcium ($Ca^{2+}$) handling and the efficiency of the actin–myosin contractile machinery. In addition, AFM-based measurements of cellular stiffness properties offer further information on cytoskeletal organization and the mechanical competence of the cell. Taken together, these measurements provide a comprehensive picture of cardiomyocyte physiology and enable the identification of functional biomarkers relevant for both basic research and preclinical investigations.

**Added value of the AFM–MEA single-cell approach**

A key strength of the integrated AFM–MEA approach lies in the possibility of directly quantifying electro-contractile coupling with high temporal resolution. This parameter reflects the efficiency with which electrical excitation is translated into mechanical

contraction, encompassing intracellular calcium release, troponin activation, and cross-bridge formation within the contractile apparatus. Alterations in this coupling could indicate impaired calcium handling, dysfunction of the contractile machinery, or early stages of pathological remodeling [140]. Such alterations are difficult to detect when electrical and contractile-mechanical measurements are performed separately, highlighting the importance of synchronized multimodal measurements for a more complete understanding of cardiomyocyte function.

A key advantage of the proposed platform is its ability to perform longitudinal measurements at the single-cell level, enabling repeated interrogation of the same cardiomyocyte across multiple experimental sessions. Unlike conventional cardiac models based on multicellular preparations or engineered tissues—which provide valuable information on collective behavior but may obscure intrinsic cellular heterogeneity—this approach allows direct investigation of individual cardiomyocyte properties without confounding cell–cell interactions. By leveraging the spatial reference provided by the MEA electrode grid, the AFM cantilever can be reliably repositioned over the same cell across different days *in vitro*, enabling continuous tracking of electromechanical properties over time. This combined single-cell and longitudinal capability allows a more precise characterization of electrophysiological and mechanical functionality, facilitates the study of temporal changes associated with cellular maturation or experimental treatments, and reduces variability arising from cell-to-cell heterogeneity.

Beyond the simultaneous measurement of electrical activity and contractile force, the AFM-based component of the system enables the investigation of dynamic mechanical properties of cardiomyocytes. In particular, the reconstruction of the temporal evolution of the Young's modulus during the cardiac cycle provides insight into how cellular stiffness changes during contraction and relaxation. Unlike static measurements of mechanical stiffness, this approach allows the characterization of the dynamic biomechanical behavior of the cell and its relation to electrical activation [141].

Such information may contribute to the identification of subtle mechanical alterations associated with pathological conditions, cytoskeletal remodeling, or drug-induced cardiotoxicity [142],[143].

The sensitivity of the extracted parameters to pathological and pharmacological perturbations makes the platform particularly suitable for disease modeling and preclinical safety testing. For example, the prolongation of field potential duration can reproduce phenomena analogous to QT interval prolongation observed in clinical settings, whereas

irregularities in inter-beat intervals can mimic arrhythmic conditions [136],[137]. Similarly, alterations in mechanical parameters such as reduced contraction force amplitude or abnormal cellular stiffness may serve as early indicators of cardiotoxicity, cardiomyopathy, fibrosis, or cytoskeletal remodeling. In this context, the integrated AFM–MEA approach may represent a valuable bridge between fundamental cellular investigations and translational research, offering a controlled experimental environment for evaluating disease mechanisms and therapeutic responses, with high spatial and temporal resolution.

**Platform improvements**

The development of the present platform builds upon previous studies carried out by our research group ([92],[93],[94]) and introduces several methodological improvements.

Earlier configurations relied heavily on custom-built hardware and software components and involved a relatively large number of elements, which increased system complexity. In contrast, the setup described in this work is based predominantly on commercially available components, resulting in a simpler and more user-friendly configuration that may also improve reliability and reproducibility due to the use of standardized instrumentation. Another important improvement concerns the quantitative assessment of cardiomyocyte contractility. In previous studies, contraction was mainly evaluated qualitatively, whereas the present approach enables the direct measurement of contractile force. Quantitative force measurements provide objective and reproducible data on cellular functionality, allowing precise comparisons across different experimental conditions and facilitating the detection of subtle variations in contractile performance.

Furthermore, the custom data analysis pipeline developed in this work enables the simultaneous processing of electrical, contractile, and mechanical signals at the single-cell level. Compared with earlier analyses, this approach allows the extraction of a larger set of parameters and enables a more comprehensive characterization of cardiomyocyte functionality. In particular, the quantification of the electrocontractile coupling parameter provides essential information on the temporal relationship between electrical activation and mechanical contraction, a fundamental aspect of cardiomyocyte physiology with important implications for both normal cardiac function and pathological conditions.

**Platform limitations**

Despite its advantages, the methodology also presents limitations that should be considered. The experimental setup is relatively complex and requires operators trained in

both MEA and AFM techniques. The system requires careful calibration and stabilization to ensure reliable and reproducible measurements.

The duration of measurements is inherently constrained by the viability of cells outside the incubator. Future improvements could include the integration of environmental control systems capable of maintaining, not only physiological temperature (37 °C), but also appropriate $CO_2$ concentration and humidity. Such improvements would improve experimental stability and enable longer observation periods, extending the applicability of the methodology to studies requiring prolonged observation.

Finally, AFM-based measurements involve physical contact between the cantilever and the cell surface, which may potentially perturb cellular behavior. In the present study, the applied forces were minimized and acquisition parameters were optimized to reduce mechanical perturbation and preserve the physiological contractile dynamics of the cells. Nevertheless, this aspect should always be considered when interpreting AFM-derived measurements.

Lastly, interrogating a single cell at a time using the AFM inherently limits the throughput of the approach. While this method provides high-resolution and precise functional measurements, this limitation may restrict its applicability.

Overall, the integrated AFM–MEA platform developed in this work provides a powerful tool for the multidimensional characterization of cardiomyocyte electromechanical activity at the single-cell level. By combining electrophysiological, contractile, and biomechanical measurements within a single experimental framework, this approach enables a more complete understanding of cardiomyocyte function and provides a robust methodological foundation for future studies in cardiac physiology, disease modeling, and pharmacological research.

The integrated AFM–MEA platform presented in this chapter enables the simultaneous quantification of electrical activity, contractile dynamics, and biomechanical properties of individual cardiomyocytes. By providing a multidimensional characterization of cardiomyocyte electromechanical function, this methodology represents a powerful tool for investigating physiological and pathological alterations in cardiac cells.

Building on this methodological framework, the next paragraph applies these quantitative descriptors to the study of drug-induced alterations in cardiomyocyte function, focusing on doxorubicin-induced cardiotoxicity and on the potential cardioprotective effects of extracellular vesicles derived from human amniotic fluid stem cells.

## 2.2 Cardioprotective Assay

I employed the AFM-MEA combined platform described in the previous paragraph to examine the cardiotoxic effects of the chemotherapy drug Doxorubicin (Dox) on a two-dimensional *in vitro* model of postnatal murine cardiac cells, and evaluate the cardioprotective potential of extracellular vesicles (EVs) separated and concentrated from the secretome of human amniotic fluid stem cells (hAFSC). In particular, the study investigated whether hAFSC-EVs could promote the functional recovery of *in vitro* cardiac cells in this Dox-induced cardiotoxicity.

This work was carried out in collaboration with the research group of Prof. Sveva Bollini (Department of Experimental Medicine, DIMES, University of Genova), with specific experimental support from Dr. Pietro Arnaldi in cardiomyocyte culture and imaging.

### 2.2.1 Introduction

The following chapter reports the experimental findings on the cardioprotective role of EVs released by human amniotic fluid-derived stem cells (hAFSC-EVs) in primary cardiomyocytes *in vitro*. The model system consists of a two-dimensional cardiac culture, whose functional activity was quantitatively assessed through a combined approach integrating microelectrode arrays (MEA) and atomic force microscopy (AFM), enabling simultaneous evaluation of electrical and contractile-mechanical properties.

Building on the parameters defined in Section 2.1, the analysis examines both the extent of Dox-induced cardiotoxicity and the degree of functional recovery mediated by hAFSC-EVs.

*Cancer-related Cardiotoxicity*

Cardiotoxicity associated with anticancer drugs is a well-known and widely documented phenomenon [144],[145]. This awareness has led to the development of cardio-oncology, an interdisciplinary field dedicated to studying the molecular and clinical changes affecting the cardiovascular system following cancer therapy. Among these, the cardiotoxic effects of anthracyclines and monoclonal antibodies targeting HER2 are well known, although their mechanisms of action are not yet fully understood [146]. In particular, we will focus on a specific type of anthracycline: Doxorubicin (Dox). This drug acts as an intercalating agent, inserting itself between DNA bases and thereby blocking DNA synthesis and transcription, while also inhibiting the activity of the enzyme topoisomerase II, making it a highly effective chemotherapeutic agent against various types of cancer, especially solid tumors and hematologic malignancies [147]. Unfortunately, since its discovery, doxorubicin has been associated with cardiac damage [148],[149]. Cardiotoxicity is among the most severe side

effects of this drug, presenting as electrocardiographic abnormalities, arrhythmias, contractile impairment, cardiomyopathy, and congestive heart failure, which may appear even years after treatment has ended [150]. At the molecular and cellular levels, the mechanisms involved remain complex and only partially understood. Nonetheless, numerous studies suggest that doxorubicin increases oxidative stress through the production of reactive oxygen species (ROS), impairs mitochondrial function, activates pro-inflammatory pathways, disrupts electrical conduction, alters intracellular calcium handling, and causes DNA damage, ultimately leading to cell death, primarily through apoptosis [151],[152],[153].

Recent studies have shown that the administration of Doxorubicin (Dox) in *in vitro* cardiac models causes functional alterations in cardiomyocytes, which manifest as a reduced heart rate, increased rhythm irregularity, decreased extracellular field potential amplitude, and a decline in both contractile strength and contraction amplitude [154],[155],[156],[157].

*Extracellular Vesicles*

Extracellular vesicles (EVs) are nano-sized, lipid bilayer-enclosed particles released by virtually all cells into the extracellular space. They act as key mediators of intercellular communication through their cargo, which is enriched with bioactive molecules such as small peptides, lipids, and non-coding RNAs, particularly microRNAs. Human amniotic fluid stem cells (hAFSC) are fetal mesenchymal progenitor cells that can be easily isolated from residual amniotic fluid samples obtained, with informed consent from healthy donors, during routine prenatal procedures, including second-trimester amniocentesis or scheduled cesarean sections at term. These cells exhibit high self-renewal capacity and strong paracrine activity both *in vitro* and *in vivo* [158],[159]. The soluble factors released by hAFSCs into their conditioned medium (hAFSC-CM), collectively referred to as the secretome, have demonstrated pro-resolving effects in several preclinical models of inflammatory diseases. This supports the concept of exploiting the hAFSC secretome as a powerful, cell-free therapeutic strategy with significant potential in regenerative medicine, particularly for cardiac injury [160].

Extracellular vesicles isolated and concentrated from hAFSC-CM (hAFSC-EVs) have been shown to recapitulate most of the biological effects of the total secretome, including the promotion of cell survival, proliferation, angiogenesis, and the attenuation of inflammation. Notably, hypoxic preconditioning of hAFSCs enhances the release of EVs enriched in cardioactive factors, thereby increasing their therapeutic efficacy [161],[162].

In preclinical *in vitro* and *in vivo* models of doxorubicin-induced cardiotoxicity, priming cardiac cells with the hAFSC secretome resulted in marked cardioprotective effects. These include reduced DNA damage and cellular senescence, along with preservation of cardiomyocyte and cardiac stromal cell (CPC) viability [163],[162]. Mechanistically, these effects were linked to upregulation of protective signaling pathways (e.g., PI3K/Akt), increased expression of drug-efflux transporters like Abcb1b, and modulation of cytokines such as IL-6 and CXCL1. These effects support cardiac repair and functional recovery, including improved myocardial perfusion and reduced infarct size [164].

Compared to adult mesenchymal stem cells (MSCs), hAFSCs may offer superior paracrine potential, easier isolation from otherwise discarded clinical samples, and greater scalability due to their resilience to cryopreservation. Importantly, hAFSC-derived EVs provide a promising alternative to traditional cell-based therapies, potentially overcoming associated risks such as immune rejection while retaining therapeutic efficacy through their secreted vesicles [163],[162].

In conclusion, hAFSC-derived EVs represent a novel, ethically sound, and highly effective cell-derived yet cell-free therapeutic approach for regenerative medicine. Their application is particularly promising in counteracting chemotherapy-induced cardiotoxicity and promoting endogenous cardiac repair mechanisms, marking a significant advancement in the development of paracrine-based strategies for cardiovascular regeneration.

In section 2.2.2 – Materials and methods, the experimental protocol is described in detail, including the cellular model, treatment conditions, and data acquisition procedures. In paragraph 2.2.3 – Results, the cardiotoxic effects of Doxorubicin and the potential cardioprotective properties of extracellular vesicles derived from hAFSCs on the electro-mechanical and contractile parameters of interest are presented and discussed.

### 2.2.2 Materials and Methods

*1. In vitro Cell Culture*

Primary cultures of mouse neonatal ventricular cardiomyocytes (mNVCM) were kindly provided by Prof. Sveva Bollini's laboratory. Briefly, mNVCM were obtained from wild type C57Bl6/J 2-days-old mouse pup cardiac tissue via enzymatic digestion, in compliance with national and European international standards of animal care and according to the required authorization from the Italian Ministry of Health (animal license n. 147/2023-PR).

mNVCMs were obtained using the Pierce Primary Cardiomyocyte Isolation Kit (Thermo Fisher Scientific, Monza, Italy), according to the manufacturer's instructions. The enzymatic

digestion protocol involved incubating the murine cardiac tissue at 37 °C for 30 minutes in the digestive enzymes papain and thermolysin. The tissue was then washed in HBSS to remove enzymatic and blood components, and subsequently resuspended in culture medium. The complete culture medium consisted of Dulbecco's Modified Eagle Medium (DMEM) supplemented with 10% Fetal Bovine Serum (FBS) and 1% penicillin/streptomycin (all from Gibco–Thermo Fisher Scientific, Monza, Italy) (complete-DMEM). The tissue was then mechanically dissociated by pipetting, in order to obtain a single-cell suspension.

The isolated mNVCMs were plated on microelectrode arrays (MEAs) coated by a fibronectin and gelatin solution at a density of 1500 cells/mm². This density was chosen to ensure the formation of a functional syncytium while still allowing single-cell measurements.

Preparation of the MEAs before seeding involved the following steps:

- Washing with deionized water (Milli-Q) and detergent (Extran® MA 01, alkaline cleaner).
- Sterilization in oven at 120 °C for 3 hours.
- Overnight coating at 37 °C with adhesion factor: 0.2% gelatin (Sigma-Aldrich, Merck, Darmstadt, Germany) and fibronectin (Sigma-Aldrich, Merck, Darmstadt, Germany, dilution 1/40).
- Protocol of cell seeding on MEA:

  **DIV0**: Cell were seeded at 1500 cell/mm² through 60 µl of cell suspension for 4-5 h, followed by flooding the MEA substrate with complete-DMEM to a final volume of 1.5 ml.

  **DIV1**: Complete matrix's washing to remove dead cells and general cleaning of the substrate, followed by medium replacement with complete-DMEM supplemented with 1/1000 Growth Supplement (GS) (DMEM-GS) to inhibit fibroblast overgrowth.

  **DIV2**: If needed, a second complete matrix washing and medium replacement were performed to remove residual debris that could affect AFM measurements.

  **DIV3**: Cells left to rest.

  **DIV4**: Baseline recordings, followed by treatments.

  **DIV5**: Recordings under the different experimental conditions (as shown below).
- Cells were maintained in culture under standard conditions (37 °C, 5% $CO_2$ and 20% $O_2$) and allowed to adhere and recover before experimental measurements.

*2. hAFSC - Extracellular Vesicles*

hAFSC-EVs were generously provided by Prof. Bollini's lab. hAFSC were obtained from discarded and leftover samples of human amniotic fluid collected during routine prenatal diagnosis procedures, following written informed consent from healthy donors, in

compliance with the specific approval from the local Ethics Committee and with the corresponding authorization (P.R. 428REG2015 from Comitato Etico Regione Liguria). Briefly, adherent stromal cells were isolated from human amniotic fluid (hAF) through immuno-magnetic selection for the c-KIT antigen, generating primary hAFSC cultures, as previously described by Prof. Bollini's group [165],[166],[167].

Extracellular vesicles were subsequently isolated and concentrated from the *in vitro* hAFSC secretome using standardized protocols in accordance with MISEV guidelines [160],[159],[168].

Briefly, hAFSC-CM was collected from hAFSC preconditioned under hypoxic conditions (1% $O_2$, 5% $CO_2$, 37°C) for 24 hours in a serum-free medium (SF: DMEM medium supplemented with 1% l-glutamine and 1% penicillin/streptomycin; all from Gibco—Thermo Fisher Scientific). EVs contained in the conditioned medium were isolated and concentrated through a combination of serial ultracentrifugation and size exclusion chromatography (SEC). Their size distribution and concentration were assessed by nanoparticle tracking analysis (NTA) using a Nanosight NS300 instrument (Malvern Panalytical, UK). The isolated hAFSC-EVs were then resuspended in phosphate-buffered saline (PBS) and stored at −80°C until further use.

For experimental applications, EV suspensions were diluted in complete culture medium to reach the desired working concentration prior to administration to cardiomyocyte cultures.

*3. Treatment Protocol*

The experimental protocol was designed to include four different conditions:

1. Condition 1 (C): Cells in control condition
   Control cells (not subjected to any treatment) were analyzed to ensure that any variation in specific parameters observed in treated cells could be attributed to the treatment itself, rather than to spontaneous physiological changes. After baseline measurements, the culture medium was replaced with complete-DMEM medium.
2. Condition 2 (D): Cells exposed to pro-apoptotic and cardiotoxic Dox dosage
   Following baseline measurements, fresh complete-DMEM medium supplemented with Dox (final concentration: 1 μM) was prepared and used as culture medium.
   The effects of the chemotherapeutic agent were evaluated after 21 hours of incubation. Variations in the parameters of interest were assessed by comparing the measurements obtained under basal conditions (DIV4) with those recorded after 21 hours of treatment (DIV5).

3. Condition 3 (E): Cells primed by hAFSC-EVs

   Following baseline measurements, fresh complete-DMEM supplemented with hAFSC-EVs (final concentration: $100k/mm^2$ ) was prepared and used as the culture medium. Each matrix was initially incubated with $100k/mm^2$ EVs in 700 µL of medium for 3 hours to promote efficient extracellular vesicle uptake by the cells. Following EV priming, 800 µL of complete-DMEM was added to reach the final volume of 1,500 µL required for proper experimental measurements, and left for the following 21 hours.

   The effects of EVs alone were evaluated after 24 hours of incubation to determine whether the vesicles themselves had any influence on cardiomyocyte functional activity.

4. Condition 4 (ED): Cells primed by hAFSC-EVs and exposed to pro-apoptotic and cardiotoxic Dox dosage

   Following baseline measurements, fresh complete-DMEM supplemented with hAFSC-EVs (final concentration: $100k/mm^2$) was prepared and used as the culture medium. Each matrix was initially incubated with $100k/mm^2$ EVs in 700 µL of medium for 3 hours to promote efficient extracellular vesicle uptake by the cells.

   Following EV priming, 800 µL of complete-DMEM supplemented with 1 µM Dox was added and left for the following 21 hours.

   In this condition, extracellular vesicles were administered 3 hours prior to Dox treatment, for a total of 24 hours. This approach was designed to assess whether pre-treatment with EVs could exert a protective effect against Dox-induced damage.

A schematic representation of the experimental timeline and treatment protocol is shown in Fig 2.12.

The experimental design aimed to evaluate the functional impact of Dox on mNVCMs by comparing the results obtained from Dox-treated cells (Condition 2) with those of the control group (Condition 1). This comparison allowed assessment of the drug's effects on cell health and identification of the parameters most affected by treatment.

Subsequently, these findings were compared with those from cells subjected to the combined treatment (EV + Dox; Condition 4), in order to determine whether EV pre-treatment could mitigate Dox-induced damage.

Finally, cells treated exclusively with EV (Condition 3) provided insights into whether vesicles alone could alter cardiomyocyte physiology.

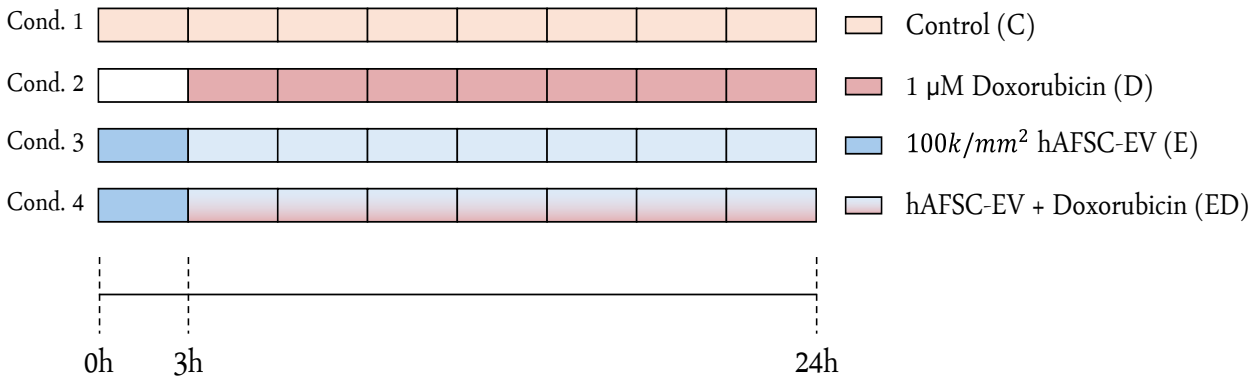


**Fig 2.12 Schematic representation of the experimental treatment protocol and timeline for the four treatment conditions**. From top to bottom: control (C), doxorubicin-treated cells (D, 1 μM), extracellular vesicle-treated cells (E, 100k/mm² hAFSC-EVs), and combined treatment (ED, hAFSC-EVs + doxorubicin). After baseline measurements (0 h), the culture medium was replaced with treatment-specific media, and cells were maintained under these conditions until the final measurements at 24 h. In the combined condition (ED), hAFSC-EVs were administered 3 h prior to doxorubicin treatment to evaluate their potential protective effect against drug-induced cardiotoxicity.

*4. Experimental Procedure*

Overview

Each experimental session was carried out in the following phases:

**Experimental Setup Preparation**

All components required for the measurements were positioned and connected. This included cable connections, assembly of the JPK NanoWizard 4.0 AFM system (Bruker Corp., Berlin, Germany) — insertion of the cantilever into the holder and placement of the holder into the AFM head — and activation of the thermostat.

**AFM Calibration**

AFM calibration was performed as described in Section 2.1:

- Cantilever spring constant determination: The *Thermal Noise* method was used. The same cantilever was employed for all experiments (Biosphere B2000-FM: k = 1.6 N/m, tip = 4 μm spherical probe). At the end of each daily session, the cantilever was rinsed with water and soap to remove any residual cellular material that might have adhered to the tip.
- Optical system sensitivity determination: A force–distance curve map was acquired on a petri dish in culture medium (scan area = 15 μm × 15 μm; resolution = 16 × 16 pixels; Set Point = 1.5 V; Z-Length = 300 nm; Z-Speed = 2 μm/s). Sensitivity was obtained by fitting the contact region of the force–distance curve with a straight line and calculating the inverse of the slope.

**Sample Preparation**

The substrate (MEA) designated for measurement was removed from the incubator, placed into the MEA2100-Mini-Systems headstage, positioned beneath the AFM head, and the AFM cantilever was positioned onto the matrix.

**Equilibration Period**

A waiting time of 5 minutes was allowed to ensure equilibrium conditions.

**Preliminary Sample Assessment**

Optical inspection of the sample was performed, followed by a 1-minute recording of the electrical activity across the entire matrix. Electrodes with the best signal-to-noise ratio (SNR), and on which clearly identifiable cell bodies were present, were selected for subsequent measurements. Selected cell/electrode sites were approached sequentially.

**Simultaneous AFM–MEA Measurements**

For each selected electrode, the AFM cantilever was positioned over the cell of interest. An optical image documenting the relative positioning of the cell and cantilever was acquired. Three acquisition modalities (AFM) of contractile and mechanical activity were then performed, with simultaneous recording of the electrical activity (MEA). Each acquisition was saved in the Multi Channel Suite – Experimenter software with a dedicated file name corresponding to the acquisition mode and the selected electrode number.

At the end of each measurement sequence on a given electrode-cell, the cantilever was retracted and raised to a height of 10 µm above the sample surface. This precaution ensured safe navigation within the MEA system, preventing accidental contact with other regions of the sample during lateral (x–y) movement. A new target cell was then selected, and the acquisition procedure was repeated under identical conditions.

To preserve proper cellular function and prevent impairment due to suboptimal culture conditions (i.e., lack of appropriate $CO_2$ and humidity levels), the substrate was never kept outside the incubator for more than 30–40 minutes. Within this time frame, an average of five cells per substrate could typically be acquired.

Upon completion of baseline data acquisition (on all available MEAs), the quality of the recordings (evaluated in real time during the measurements) was used to determine which substrates were assigned to each of the four treatment conditions (previously described). Treatments corresponding to conditions 2, 3 and 4 were then applied accordingly.

On the following day (DIV5), the same experimental procedure was repeated.

The only difference was that the optical images acquired on the previous day (DIV4) were used to reposition the cantilever precisely at the same location on the same cell acquired before, thereby enabling direct single-cell comparisons across experimental days.

Data Acquisition

Once the cell of interest was selected, measurements were performed in three sequential acquisition modes. In each case, the electrical signal (MEA) was recorded simultaneously with the contractile–mechanical signal (AFM), and thus both were acquired for the same duration.

**1. Amplitude mode**

The cantilever was brought into contact with the cell surface in *Contact Mode–Constant Force*, with a minimal set point sufficient to maintain stable tip–cell contact throughout the measurement (Set Point = 3 nN). The signal from the piezoelectric actuator controlling the vertical position of the cantilever was monitored in real time, and feedback parameters were adjusted to optimize the signal-to-noise ratio (typically IGain = 50 Hz, PGain = 0.0001).

The signal was then recorded for 60 s, producing a displacement profile corresponding to the cell's contractile activity. From this profile, the *Contraction Amplitude* was extracted as the primary parameter.

At the end of the recording, the cantilever was retracted 5 µm above the cell surface while maintaining its lateral (x–y) position, before proceeding to the next acquisition mode.

**2. Contraction mode**

The cantilever was brought back into contact with the cell in *Contact Mode–Constant Force*, this time using a higher set point (Set Point = 10 nN) to apply sufficient force to counteract the cell's vertical excursion during contraction. Immediately after contact, the feedback gains were set to zero (IGain = 0 Hz, PGain = 0), thereby fixing the cantilever's position relative to the cell surface. In this configuration, the vertical deflection of the cantilever was recorded for 60 s, and subsequently converted into force by multiplying the deflection signal (in nm) by the cantilever's spring constant, yielding the parameter defined as *Contraction Force*.

Following the acquisition, the cantilever was lifted again by 5 µm above the cell surface before proceeding to the final measurement mode.

**3. Mechanical mode**

Mechanical characterization was performed in *Force Spectroscopy Mode*, acquiring force–distance (F–D) curves to extract the mechanical parameters of interest. Acquisition parameters were set as follows:

- Set Point: 5 nN

- Z-Length: 3 µm
- Z-Speed: 60 µm/s
- Resolution (# pixels): 32 × 32 pixels
- Scan Area: 1 nm × 1 nm
- Total curves per map: 1024

These parameters were optimized to ensure high-quality force–distance curves, generate a sufficiently large dataset for subsequent analysis, and complete each map within a reasonable timeframe. This strategy enabled the analysis of a large number of cells per matrix while minimizing the time samples spent outside the incubator.

A scan area of 1 nm × 1 nm was chosen to focus on the temporal evolution of the parameters. Such a small area can be considered equivalent to a single point, allowing the acquisition to be treated as a point measurement of the parameter over time.

A set point of 5 nN produced indentations of approximately 500 nm, which is appropriate for applying the DMT model (tip shape = sphere, tip radius = 2 µm, Poisson ratio = 0.5), as it requires indentations not exceeding ~5–10% of the sample height.

The Z-length was selected to ensure complete detachment of the cantilever from the cell throughout the entire cardiac cycle, both at maximum contraction (greater cell height) and at relaxation (reduced cell height). Longer Z-Lengths would have unnecessarily increased acquisition times, while shorter ones would have risked incomplete detachment.

Furthermore, the choice of resolution (number of pixels) and Z-speed allowed the overall acquisition time to be minimized while still ensuring that a sufficient number of curves, with good SNR, were collected to accurately capture the temporal dynamics of the parameters of interest.

Under these acquisition conditions (ZL = 3 µm, ZS = 60 µm/s → 50 ms/curve), the mechanical measurement could be completed in approximately 90 seconds, yielding 1,024 force–distance curves per cell, all acquired at the same location. At a beating frequency of approximately 3 Hz, this corresponds to about four curves being recorded between successive beats.

A total of six independent experimental sessions were performed.

In each session, 12 MEA substrates were prepared, corresponding to 3 substrates per experimental condition (Control, Doxorubicin, hAFSC-EVs, and hAFSC-EVs+ Doxorubicin). For measurements combining MEA recordings with AFM *amplitude* and *contraction* modes, for each MEA substrate, approximately 5 individual cardiomyocytes were selected, resulting

in an average of ~15 cells acquired per condition per experimental session. Overall, the dataset comprised approximately 90 cells per treatment group (6 experiments × 3 MEAs × ~5 cells), providing a robust sample size for statistical analysis.

In contrast, measurements involving mechanical characterization (MEA recordings and AFM *mechanical* mode) were performed in a single experimental session. In this case, approximately 15 cells per condition were analyzed, resulting in a reduced sample size compared to the other acquisition modalities.

Data Analysis

Signal processing and parameter extraction were performed according to the procedures described in paragraph 2.1. The same electrical, contractile, and mechanical descriptors were quantified to enable direct comparison across treatment conditions.

*5. Immunostaining Analysis*

Immunostaining analysis was carried out in collaboration with Dr. Pietro Arnaldi. Cells cultured on MEAS were fixed with 4% paraformaldehyde (PFA) for 10 minutes at room temperature and subsequently washed twice with phosphate-buffered saline (PBS). Cells were then permeabilized with PBS containing 0.1% Triton X-100 (PBST) for 5 minutes, followed by incubation for 1 hour in a blocking solution containing bovine serum albumin (BSA). Cardiomyocytes were identified within the cultures using a primary antibody against α-sarcomeric actinin (ab9465, Abcam), which enables the detection of sarcomeric structures. This was followed by incubation with an Alexa Fluor 564-conjugated secondary antibody (Life Technologies Italy—Thermo Fisher Scientific, Monza, Italy). Nuclei were counterstained using Hoechst 33342 solution. Imaging of cardiomyocytes was performed using a spinning disk confocal microscope (IXplore Spin, Evident Scientific) equipped with a 10× objective. Image acquisition was conducted using CellVivo software.

*6. Statistical Analysis*

Statistical analyses were performed using MATLAB (The MathWorks, Natick, MA, USA). To evaluate treatment effects over time, linear mixed-effects models were applied to each parameter of interest using two complementary approaches.

Treatment effects were primarily evaluated at the single-cell level by analyzing relative variations between time points, to specifically capture cell-resolved dynamic responses over time, allowing a robust assessment of treatment-induced changes while preserving single-cell variability. For each parameter, the relative percentage change (Δ%) between DIV4 and DIV5 was computed for each cardiomyocyte. Linear mixed-effects models were then applied

to these Δ% values, including experimental condition (C, D, ED, E) as a fixed effect. To account for the hierarchical structure of the data, random intercepts for experiment, MEA substrate (well), and individual cell were included in the model. Planned contrasts were used to compare treatment effects across conditions (D vs C, ED vs D, ED vs C, and E vs C).

To complement this analysis, population-level statistical evaluation was performed on raw values using linear mixed-effects models including time (DIV4 vs DIV5), experimental condition, and their interaction as fixed effects. Random intercepts for experiment, MEA substrate, and cell were included to account for variability between experiments and substrates as well as repeated measurements within the same cardiomyocyte across time. Planned contrasts were used to compare temporal changes (Δ = DIV5 − DIV4) across experimental groups.

All statistical tests were two-sided and statistical significance was defined as $p < 0.05$. Cardiotoxicity was defined as a statistically significant difference in temporal change between the doxorubicin-treated and control groups (D vs C). Evidence of cardioprotection by extracellular vesicles was defined as the presence of cardiotoxicity together with a significant difference between the ED and D groups and the absence of a significant difference between the ED and C groups, indicating recovery toward the control condition.

### 2.2.3 Results

The cardiotoxic effects of doxorubicin and the potential cardioprotective action of extracellular vesicles derived from human amniotic fluid stem cells (hAFSC-EVs) were investigated using the integrated AFM–MEA platform described in paragraph 2.1.

To evaluate the impact of cardioprotective treatments, six independent experimental sessions were performed. In each session, baseline measurements (described in the Materials and Methods section) were first obtained from cardiomyocytes under physiological conditions at DIV4. The different MEAs were then divided into four experimental groups corresponding to the following conditions:

- untreated control cells (C),
- cells exposed to doxorubicin (D),
- cells primed with hAFSC-EVs alone (E), and
- cells primed with hAFSC-EVs prior to doxorubicin exposure (ED).

Measurements were repeated at DIV5, allowing direct comparison of the functional state of the same cells before (DIV4) and after (DIV5) the treatment, whenever possible. The

analysis focused on parameters describing electrical activity, contractile performance, electro-contractile coupling, and cell mechanical properties.

Given the single-cell resolution of the experimental platform, results were primarily analyzed at the individual cell level, enabling longitudinal tracking of the same cardiomyocyte over time and direct quantification of its functional response. Single-cell results are expressed as relative changes (Δ%) between DIV4 and DIV5, providing a normalized measure of the dynamic response of each cell.

For each cell, the relative variation was calculated using the following expression:

$$\Delta\% = \frac{Mean_{DIV5} - Mean_{DIV4}}{Mean_{DIV4}} \times 100$$

where $Mean_{DIV4}$ and $Mean_{DIV5}$ represent the average values of the parameter resulting from the measurements on that cell at DIV4 and DIV5, respectively. This calculation provides a normalized measure of the relative change in the parameter over time.

To provide a comprehensive and robust characterization, population-level analyses were also performed by evaluating the distributions of parameter values at the two time points, allowing complementary statistical assessment of treatment effects.

Although a larger number of cells were initially recorded in each experimental condition, only cells exhibiting stable, high-quality signals across both measurement days were included in the analysis. As a result, the number of analyzed cells varies across conditions (C: n = 60; D: n = 62; ED: n = 57; E: n = 40).

*Effects of Doxorubicin and hAFSC-EVs on contractile parameters*

Contractile activity was characterized by analyzing contraction amplitude, contraction force amplitude, contraction force velocity, contraction force duration, and refractory period. Single-cell analysis revealed a functional impairment induced by doxorubicin treatment (Fig 2.13), as evidenced by the relative variations (Δ%) between DIV4 and DIV5.

In particular, compared to control cells, Dox-treated cardiomyocytes showed a significant reduction in **contraction force amplitude** (C-D, p = 0.03), **contraction force velocity** (C-D, p = 0.001), and **contraction amplitude** (C-D, p = 0.03), together with an increase in the **refractory period** (C-D, p = 0.02). These findings indicate a deterioration of cardiomyocyte contractile performance following doxorubicin exposure.

The reduction in contraction force and velocity reflects a decreased capacity of the cells to generate and develop mechanical force, while the decrease in contraction amplitude indicates a reduced vertical displacement of the cell surface during the contractile cycle. The increase in the refractory period suggests that cardiomyocytes require more time to recover

after a contraction before initiating the next contractile event, indicating impaired cellular recovery mechanisms following Dox exposure. Single-cell statistical analysis showed that hAFSC-EVs treatment significantly attenuated the Dox-induced alterations in contraction force amplitude (D-ED, $p = 0.01$), contraction force velocity (D-ED, $p = 0.009$), and contraction amplitude (D-ED, $p = 0.03$), with no differences observed between control and ED groups (C–ED: contraction force amplitude, $p = 0.78$; contraction force velocity, $p = 0.58$; contraction amplitude, $p = 0.96$).

Regarding the refractory period, significant differences were observed between C and D groups, suggesting a cardiotoxic effect of doxorubicin. However, EV pretreatment did not significantly mitigate this alteration (D–ED, $p = 0.65$; C–ED, $p = 0.006$).

No statistically significant differences were detected for the **contraction force duration** parameter. Only small variations were detected between the two time points, indicating minimal modulation of this parameter across conditions.

These findings were further supported by population-level analysis, which showed consistent shifts in the distributions of the measured parameters across conditions. In particular, Dox-treated cells exhibited a general reduction in contractile parameters and an increase in refractory period, while the ED group displayed a partial shift toward values closer to control conditions, confirming the trends observed at the single-cell level (Fig 2.13). Overall, the agreement between single-cell and population-level analyses confirms that doxorubicin impairs both the magnitude and the dynamics of cardiomyocyte contractility, while hAFSC-EVs exert a partial protective effect.

*Effects of Doxorubicin and hAFSC-EVs on electrophysiological parameters*

Electrical parameters derived from MEA recordings were analyzed to evaluate the electrophysiological effects of doxorubicin treatment and the potential protective action of hAFSC-EVs (Fig 2.14). Several descriptors of cardiomyocyte electrical activity were quantified, including field potential amplitude (PPA), interbeat interval (IBI), field potential duration (FPD/QT), and depolarization kinetics.

Single-cell analysis revealed that doxorubicin treatment induced significant alterations in multiple electrophysiological parameters. In particular, a significant reduction in field potential amplitude (C–D, $p = 0.008$) was observed, together with significant changes in interbeat interval (C–D, $p = 0.008$), field potential duration (C–D, $p = 0.01$), and depolarization speed (C–D, $p = 0.04$), indicating an overall alteration of cardiomyocyte electrophysiological behavior.

Field Potential (FP) amplitude decreased across all experimental conditions, with a more pronounced reduction observed in Dox-treated cells and in those pretreated with hAFSC-EVs. Conversely, both interbeat interval (IBI) and field potential duration (QT) decreased in the Control and hAFSC-EVs groups, whereas an increase was observed in the D and ED groups, indicating a reduction in heart rate in Dox-treated conditions.

Regarding depolarization kinetics, no statistically significant differences were detected for depolarization duration, which remained relatively stable across all conditions, as indicated by the small relative variations between DIV4 and DIV5.

In contrast, depolarization speed showed a stable behavior in the Control and EV-treated groups, while a marked decrease was observed in Dox-treated conditions (D and ED).

However, in contrast to the contractile parameters, hAFSC-EVs treatment did not produce a clear restoration of the electrophysiological alterations induced by doxorubicin. The values observed in the ED group remained closer to those measured in Dox-treated cells than to those observed in control cells (FP amplitude: D–ED $p = 0.39$, C–ED $p = 0.07$; interbeat interval: D–ED $p = 0.63$, C–ED $p = 0.001$; FP duration: D–ED $p = 0.58$, C–ED $p = 0.002$; depolarization speed: D–ED $p = 0.50$, C–ED $p = 0.10$).

These findings were further supported by population-level analysis, which showed that Dox-treated cells exhibited reduced electrical activity and altered timing parameters, while the ED group remained closer to the D condition than to control, confirming the limited electrophysiological recovery observed at the single-cell level (Fig 2.14).

Overall, the agreement between single-cell and population-level analyses indicates that doxorubicin significantly impairs cardiomyocyte electrophysiological activity. In contrast to its effects on contractile parameters, hAFSC-EVs treatment doesn’t exert a protective effect on the electrical properties of cardiomyocytes.

It is important to mention that, although QT values are reported, the estimation of this parameter may be affected by analysis artefacts. In the majority of the acquired recordings, the T-wave (corresponding to the repolarization phase) was not evident in the signal trace, which limited the reliability of automated QT detection. For this reason, the Field Potential Duration (QT) values presented here should be interpreted with caution and considered

alongside other electrophysiological descriptors, which together provide a more comprehensive overview and robust characterization of cardiomyocytes electrical behavior.

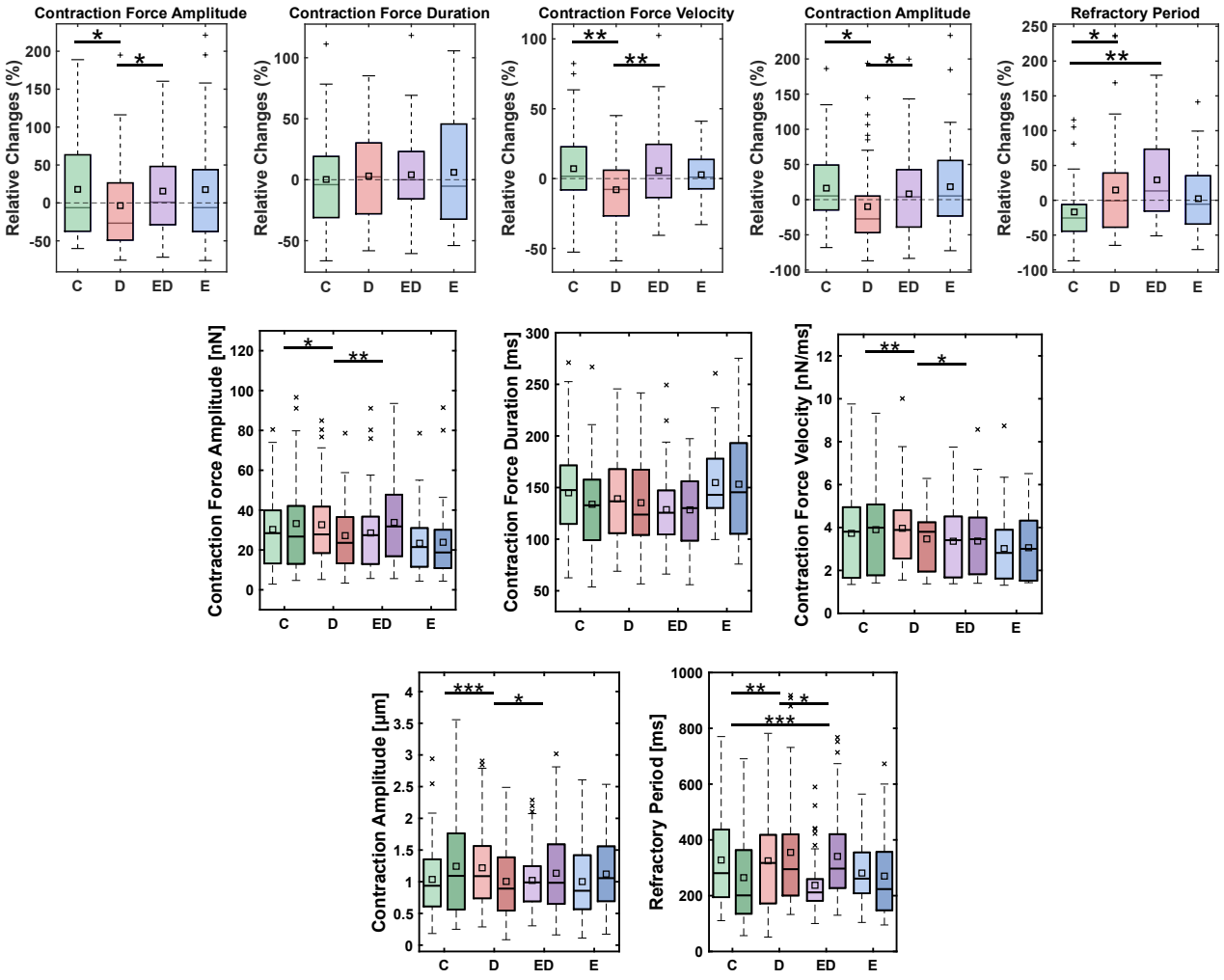


**Fig 2.13 Effects of different treatment conditions on contractile parameters of cardiomyocytes**. The figure shows contraction force amplitude, contraction force duration, contraction force velocity, contraction amplitude, and refractory period under control (C), doxorubicin-treated (D), EV-pretreated followed by doxorubicin exposure (ED), and hAFSC-EVs–treated (E) conditions. (top panels) Relative variations (Δ%) between DIV4 and DIV5 at the single-cell level, representing the dynamic response of individual cardiomyocytes. Each boxplot summarizes the distribution of Δ% values across analyzed cells (C: n = 60, D: n = 62, ED: n = 57, E: n = 40), with the square marker indicating the mean value. (middle and bottom panels) Population-level distributions of parameter values measured at DIV4 and DIV5. Each boxplot represents the distribution of values across analyzed cells. Individual data points correspond to the mean value of each cell after outlier removal, while the square marker indicates the mean of the distribution.
Statistical significance is indicated as follows: *p < 0.05, **p < 0.01, ***p < 0.001.

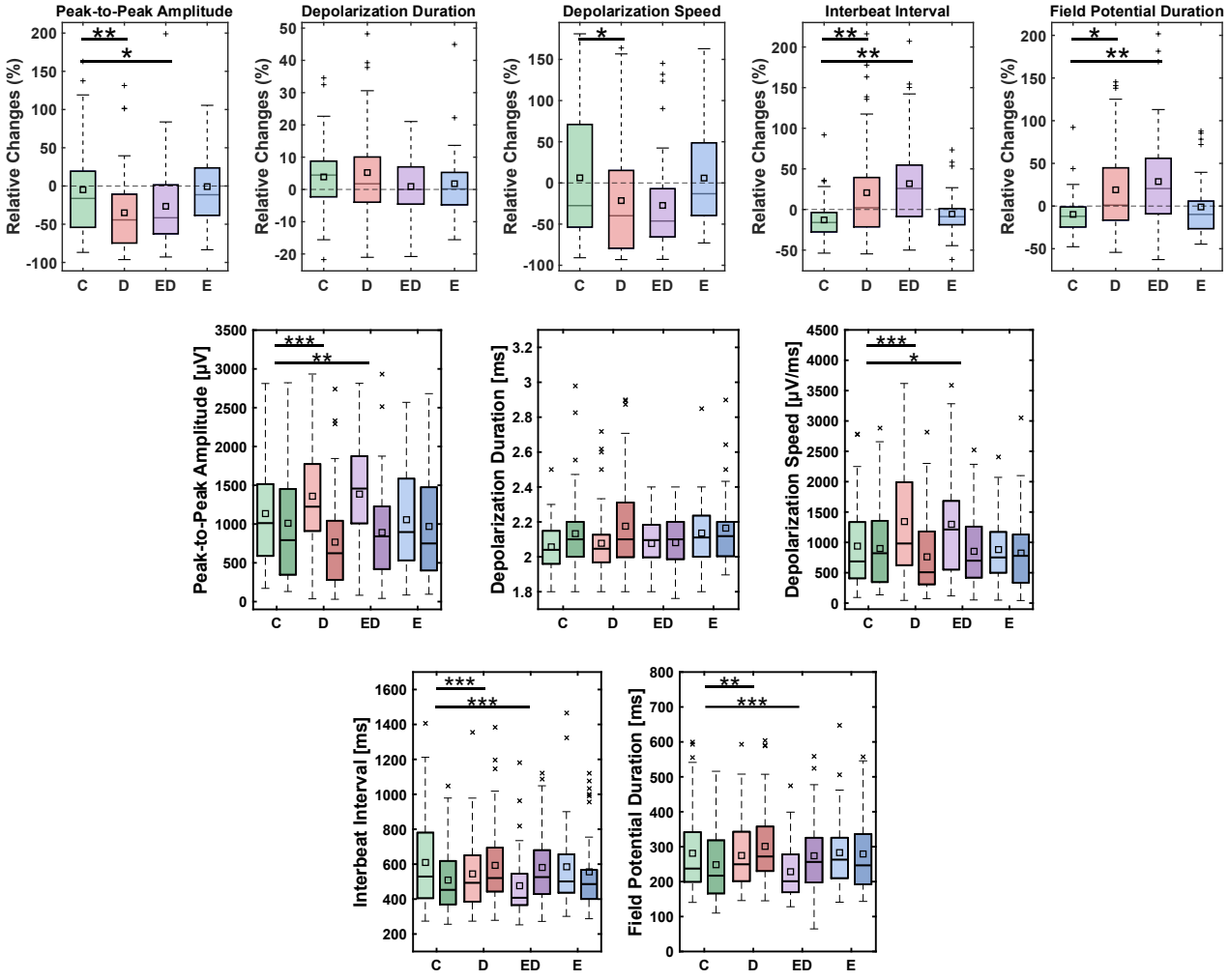


**Fig 2.14 Effects of different treatment conditions on electrophysiological parameters of cardiomyocytes**. The figure shows peak-to-peak amplitude (PPA), depolarization duration, depolarization speed, interbeat interval (IBI), and field potential duration (QT) under control (C), doxorubicin-treated (D), EV-pretreated followed by doxorubicin exposure (ED), and hAFSC-EVs–treated (E) conditions. (top panels) Relative variations (Δ%) between DIV4 and DIV5 at the single-cell level, representing the dynamic electrophysiological response of individual cardiomyocytes. Each boxplot summarizes the distribution of Δ% values across analyzed cells (C: n = 60; D: n = 62; ED: n = 57; E: n = 40), with the square marker indicating the mean value. (middle and bottom panels) Population-level distributions of parameter values measured at DIV4 and DIV5. Each boxplot represents the distribution of values across analyzed cells. Individual data points correspond to the mean value of each cell after outlier removal, while the square marker indicates the mean of the distribution.
Statistical significance is indicated as follows: *p < 0.05, **p < 0.01, ***p < 0.001.

*Effects of Doxorubicin and hAFSC-EVs on electro-contractile coupling*

In addition to direct contractile and electrical descriptors, the electro-contractile coupling (EC-Coupling) was analyzed to evaluate the temporal relationship between electrical activation and mechanical contraction in cardiomyocytes (Fig 2.15).

This parameter represents the delay between the peak of the extracellular electrical signal and the peak of the mechanical contraction measured by AFM, providing an indication of how electrical excitation is translated into mechanical contraction.

Single-cell analysis revealed that doxorubicin treatment alters EC-coupling dynamics, as evidenced by the relative variations (Δ%) between DIV4 and DIV5. While Control cells showed a general tendency toward stable or slightly decreasing values, Dox-treated groups (D and ED) exhibited a shift toward increased EC-coupling time. In particular, compared to control cells, Dox-treated cardiomyocytes showed a significant increase in EC-coupling time (C–D, $p = 0.01$), indicating a reduced efficiency in the conversion of electrical activation into mechanical contraction and supporting evidence of doxorubicin-induced cardiotoxicity.

However, pre-treatment with hAFSC-EVs did not significantly mitigate this alteration, as no significant difference was observed between D and ED groups (D–ED, $p = 0.28$).

These findings were further supported by population-level analysis, which showed a consistent increase in EC-coupling time in Dox-treated conditions and a similar distribution pattern between D and ED groups, confirming that EV treatment does not restore the temporal coordination between electrical activation and mechanical contraction (Fig 2.15).

Overall, these results indicate that doxorubicin impairs electro-contractile coupling efficiency, while hAFSC-EVs do not exert a detectable protective effect on this parameter under the tested conditions.

*Effects of Doxorubicin and hAFSC-EVs on mechanical properties of cardiomyocytes*

Mechanical parameters could be evaluated only in one experimental session, for a limited number of cells (C: n = 15; D: n = 10; ED: n = 17; E: n = 19). Therefore, no formal statistical analysis was performed for this parameter and the following results should be interpreted with caution due to the relatively limited dataset compared with the other analyses presented in this study and should be considered as exploratory observations providing preliminary insights into the mechanical response of cardiomyocytes to doxorubicin and hAFSC-EVs treatment.

**Young's Modulus (YM) Variation**

AFM force spectroscopy measurements enabled the extraction of the **Young's modulus** (YM), which provides information on the mechanical stiffness of the cardiomyocytes.

Comparison of YM values between DIV4 and DIV5 revealed variability across the experimental conditions (Fig 2.15). Distinct trends emerged among the groups. Control cells exhibited an increase in mean YM over time, which may reflect mechanical remodeling associated with culture maturation. In contrast, cardiomyocytes treated with doxorubicin showed a decrease in stiffness between DIV4 and DIV5, suggesting that doxorubicin may negatively affect the structural integrity or cytoskeletal organization of cardiomyocytes.

hAFSC-EVs–treated cells displayed a trend toward increased stiffness, similar to that observed in control cells. Notably, this behavior was observed both in EV-primed cells (E) and in EV-primed cells subsequently exposed to doxorubicin (ED).

These trends were observed in both single-cell and population-level representations, suggesting that hAFSC-EVs may promote a form of mechanical stabilization or preconditioning that could partially counteract doxorubicin-induced alterations.

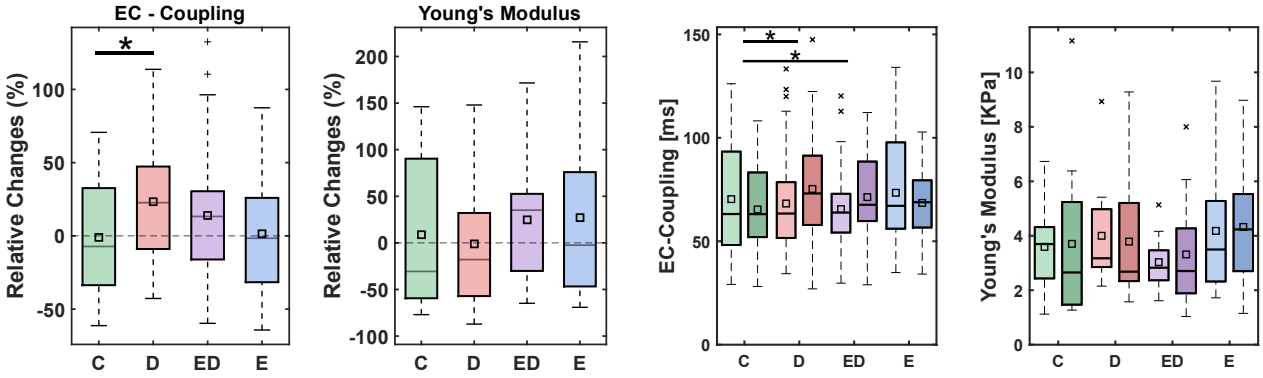


**Fig 2.15 Effects of different treatment conditions on electro-contractile coupling (EC-coupling) and mechanical properties (Young's modulus) of cardiomyocytes.** The figure shows EC-coupling time and Young's modulus (YM) under control (C), doxorubicin-treated (D), EV-pretreated followed by doxorubicin exposure (ED) and hAFSC-EVs–treated (E) conditions.
(left panels) Relative variations (Δ%) between DIV4 and DIV5 at the single-cell level, representing the dynamic response of individual cardiomyocytes. Each boxplot summarizes the distribution of Δ% values across analyzed cells, with the square marker indicating the mean value. (right panels) Population-level distributions of parameter values measured at DIV4 and DIV5. Each boxplot represents the distribution of values across analyzed cells. Individual data points correspond to the mean value of each cell after outlier removal, while the square marker indicates the mean of the distribution. Statistical significance is indicated as follows: *p < 0.05, **p < 0.01, ***p < 0.001.

**Dynamic Stiffness Parameter Variation**

The analysis of dynamic stiffness parameters requires that several conditions are satisfied, including stable and regular electrical activity, consistent mechanical measurements across cycles, and successful temporal remapping of AFM data onto the cardiac cycle. As a result, these parameters were computed on a reduced subset of cells (C: n = 9; D: n = 3; ED: n = 2; E: n = 5) compared to those used for the estimation of the YM.

To investigate how cardiomyocyte mechanical properties evolve over time and under different treatments, the relative variation (Δ%) of the mean of the dynamic parameters between DIV4 and DIV5 was calculated for each cell (Fig 2.16).

For the parameters **AUC**, **ΔStiffness**, and **YM-Max**, control cells showed rather heterogeneous variations between DIV4 and DIV5: while some cells exhibited changes close to zero or moderately negative changes, others displayed large positive variations, resulting in a broad dispersion of responses. A similar heterogeneous pattern was observed in EV-treated cells, where both positive and negative variations were present across the analyzed cells. Overall, the distribution appeared comparable to that observed in the control condition, suggesting that hAFSC-EVs treatment alone does not induce a consistent alteration of the dynamic stiffness parameters.

In contrast, doxorubicin-treated cells displayed a markedly different pattern, with all three parameters showing consistently negative variations.

Cells pretreated with EVs prior to doxorubicin exposure (ED) exhibited an intermediate behavior. While the AUC parameter showed positive variations in both analyzed cells, ΔStiffness and YM-Max displayed heterogeneous responses, with one cell showing positive and the other negative variations.

Overall, these observations suggest that doxorubicin induces a more uniform response across cells, characterized by a consistent reduction in the magnitude of the dynamic stiffness parameters, whereas control and EV-treated cells display greater variability in their responses, and cells primed with EVs prior to doxorubicin exposure tend to exhibit intermediate trends.

Finally, the ΔTime parameter exhibited a pattern distinct from the other mechanical descriptors. Control cells showed highly heterogeneous variations, whereas doxorubicin-treated cells (D, ED) displayed predominantly positive changes. In contrast, EV-treated cells mainly exhibited negative variations, with four out of five cells showing a reduction in ΔTime. This trend may suggest a modulation in the timing of the electromechanical response, potentially reflecting alterations similar to those observed in excitation–contraction coupling

dynamics, where Dox exposure has been associated with a prolongation of the electrocontractile delay.

Fig 2.17 shows representative dynamic signals obtained from four different cardiomyocytes, one for each experimental treatment condition.

Given the limited number of analyzed cells and the fact that mechanical measurements were obtained from a single experimental session, these observations should be considered exploratory and interpreted with caution.

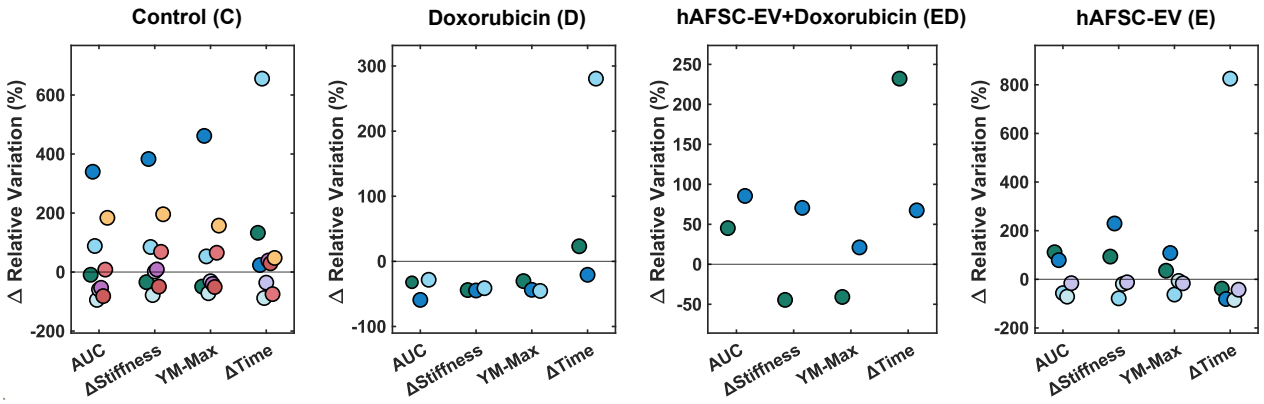


**Fig 2.16 Relative percentage variation (Δ%) of dynamic stiffness parameters between DIV4 and DIV5 for individual cardiomyocytes under different treatment conditions**. Each panel corresponds to a specific condition: control (C), doxorubicin-treated (D), hAFSC-EVs pretreated and doxorubicin-treated (ED), and hAFSC-EVs-treated (E). The variation is calculated for each parameter (AUC, ΔStiffness, YM-Max, and ΔTime). Each dot represents an individual cell, consistently identified by the same color across parameters. Only cells with reliable mechanical measurements at both time points were included in the analysis (C: n = 9; D: n = 3; ED: n = 2; E: n = 5). Doxorubicin-treated cells exhibit predominantly negative variations in dynamic stiffness parameters, except for the increase in the ΔTime parameter, while control and EV-treated cells show more heterogeneous responses. The ED condition displays intermediate behavior. Given the limited sample size and the single experimental session, these results should be considered exploratory and interpreted with caution.

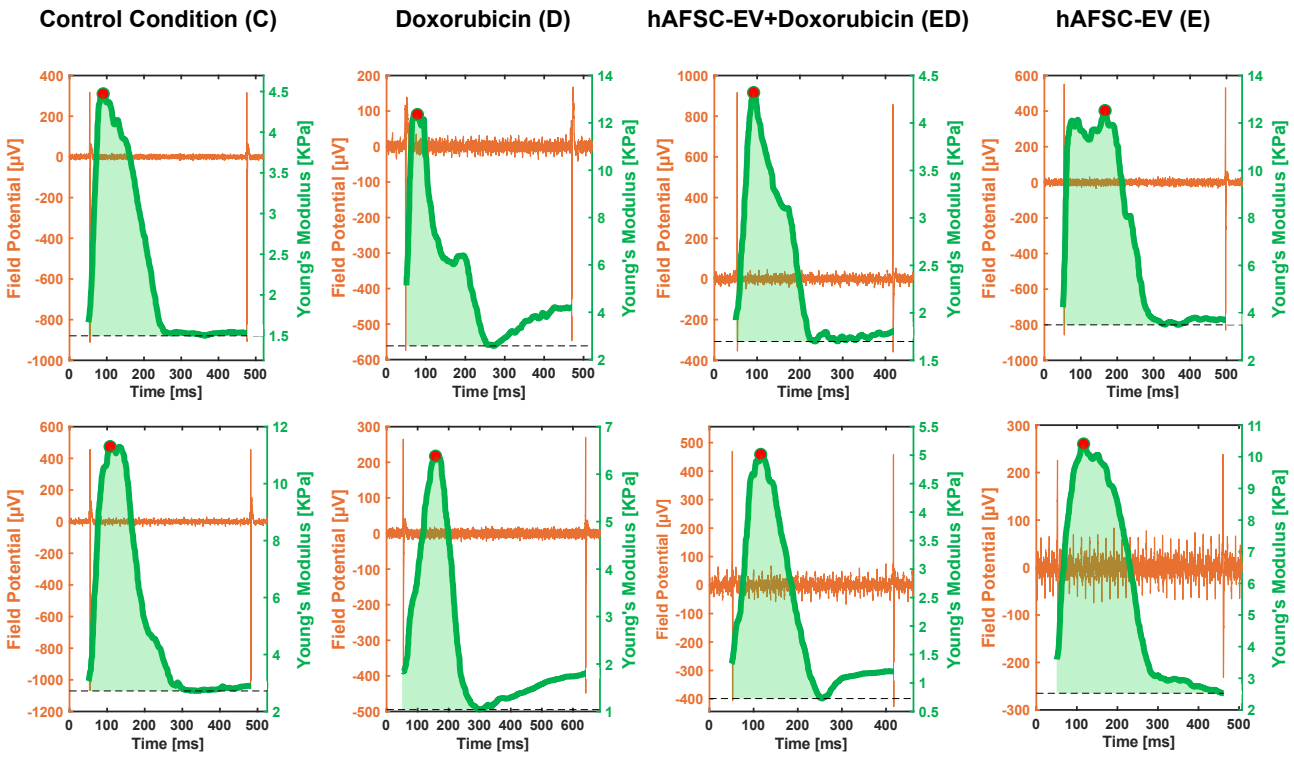


**Fig 2.17 Representative simultaneous electrical and mechanical recordings from four cardiomyocytes, each corresponding to a different experimental condition**: control (C), doxorubicin-treated (D), hAFSC-EVs pretreated and doxorubicin-treated (ED), and hAFSC-EVs-treated (E). The first row shows baseline measurements (DIV4), while the second row shows measurements after treatment (DIV5). Electrical activity recorded by the MEA (orange) is displayed together with the corresponding temporal evolution of the Young's modulus (green), highlighting the relationship between electrical excitation and mechanical response under each condition, allowing direct comparison of treatment-induced changes.

Table 2.2 summarizes the mean and standard deviation values of contractile, electrical, and mechanical parameters measured at DIV4 and DIV5 for each experimental condition (C, D, ED, and E).

| CONDITION | | | | | | | | | | | | | | | | | |
|---|---|---|---|---|---|---|---|---|---|---|---|---|---|---|---|---|---|
| **PARAMETER** | ***Control (C)*** | | | | ***Doxorubicin (D)*** | | | | ***hAFSC-EVs + Doxorubicin (ED)*** | | | | ***hAFSC-EVs (E)*** | | | | |
| | Mean | | Std | | Mean | | Std | | Mean | | Std | | Mean | | Std | | |
| | DIV4 | DIV5 | DIV4 | DIV5 | DIV4 | DIV5 | DIV4 | DIV5 | DIV4 | DIV5 | DIV4 | DIV5 | DIV4 | DIV5 | DIV4 | DIV5 | |
| **Contraction Force Amplitude [nN]** | 30,29 | 33,24 | 19,88 | 23,58 | 32,66 | 27,19 | 19,68 | 16,78 | 28,53 | 33,81 | 18,27 | 21,17 | 23,36 | 23,85 | 16,00 | 18,91 | |
| **Contraction Force Duration [ms]** | 144,94 | 133,81 | 46,69 | 42,61 | 139,15 | 135,28 | 41,74 | 45,10 | 128,60 | 128,40 | 34,55 | 36,82 | 154,78 | 153,22 | 39,78 | 55,57 | |
| **Contraction Force Velocity [nN/ms]** | 3,74 | 3,91 | 2,01 | 2,07 | 3,97 | 3,48 | 1,76 | 1,25 | 3,37 | 3,38 | 1,75 | 1,62 | 3,03 | 3,07 | 1,63 | 1,55 | |
| **Refractory Period [ms]** | 328,80 | 265,52 | 174,18 | 168,87 | 325,81 | 356,02 | 175,68 | 203,26 | 238,21 | 341,71 | 107,23 | 164,03 | 282,04 | 271,09 | 110,52 | 153,08 | |
| **Contraction Amplitude [µm]** | 1,04 | 1,25 | 0,57 | 0,81 | 1,22 | 1,01 | 0,71 | 0,60 | 1,02 | 1,14 | 0,50 | 0,68 | 1,01 | 1,13 | 0,57 | 0,60 | |
| **EC-Coupling [ms]** | 70,58 | 70,15 | 26,98 | 23,69 | 68,24 | 75,29 | 23,64 | 22,63 | 65,54 | 71,34 | 17,95 | 21,65 | 73,44 | 68,55 | 27,00 | 16,59 | |
| **Peak-to-Peak Amplitude [µV]** | 1134,85 | 1010,17 | 641,81 | 717,79 | 1358,60 | 767,14 | 705,92 | 606,60 | 1385,79 | 891,35 | 709,55 | 597,48 | 1055,68 | 969,06 | 696,46 | 691,42 | |
| **Depolarization Duration [ms]** | 2,06 | 2,13 | 0,13 | 0,23 | 2,08 | 2,18 | 0,20 | 0,27 | 2,08 | 2,08 | 0,15 | 0,15 | 2,14 | 2,16 | 0,20 | 0,22 | |
| **Depolarization Speed [µv/ms]** | 938,59 | 899,28 | 654,25 | 675,15 | 1342,87 | 761,59 | 882,45 | 631,11 | 1297,71 | 852,67 | 870,93 | 623,60 | 881,34 | 823,50 | 611,72 | 627,52 | |
| **Interbeat Interval [ms]** | 609,63 | 508,92 | 266,73 | 204,15 | 544,25 | 593,10 | 209,29 | 239,79 | 476,31 | 580,99 | 173,68 | 216,75 | 584,92 | 556,02 | 253,43 | 234,91 | |
| **Field Potential Duration [ms]** | 281,88 | 249,11 | 117,84 | 105,68 | 275,49 | 301,75 | 101,54 | 112,47 | 229,08 | 274,65 | 77,98 | 106,42 | 283,76 | 279,91 | 109,54 | 114,53 | |
| **Young's Modulus [KPa]** | 3,59 | 3,70 | 1,58 | 2,74 | 3,99 | 3,78 | 2,03 | 2,43 | 3,03 | 3,31 | 0,85 | 1,87 | 4,18 | 4,32 | 2,32 | 2,09 | |

**Table 2.2 Summary of mean and standard deviation values of contractile, electrical, and mechanical parameters across the two measurement time points (DIV4 and DIV5) for each experimental condition (C, D, ED, and E).** For each parameter, the mean value was first computed at the single-cell level for each DIV within each experiment. These values were then pooled by condition across all experiments to calculate the overall mean and standard deviation.

*Cardiomyocytes Immunostaining Characterization*

Immunostaining was performed to assess cardiomyocyte morphology under the different experimental conditions. Representative fluorescence images for each considered group (Control, Doxorubicin, hAFSC-EVs, and hAFSC-EVs + Doxorubicin) at DIV5 are shown Fig 2.18.

No major qualitative differences in overall cellular morphology were observed between the different treatment conditions. These observations suggest that, within the timeframe of the experiment, the treatments did not induce evident large-scale structural alterations detectable by immunofluorescence imaging. This also indicates that AFM–MEA analysis was essential to detect functional changes in electrophysiological and contractile behavior.

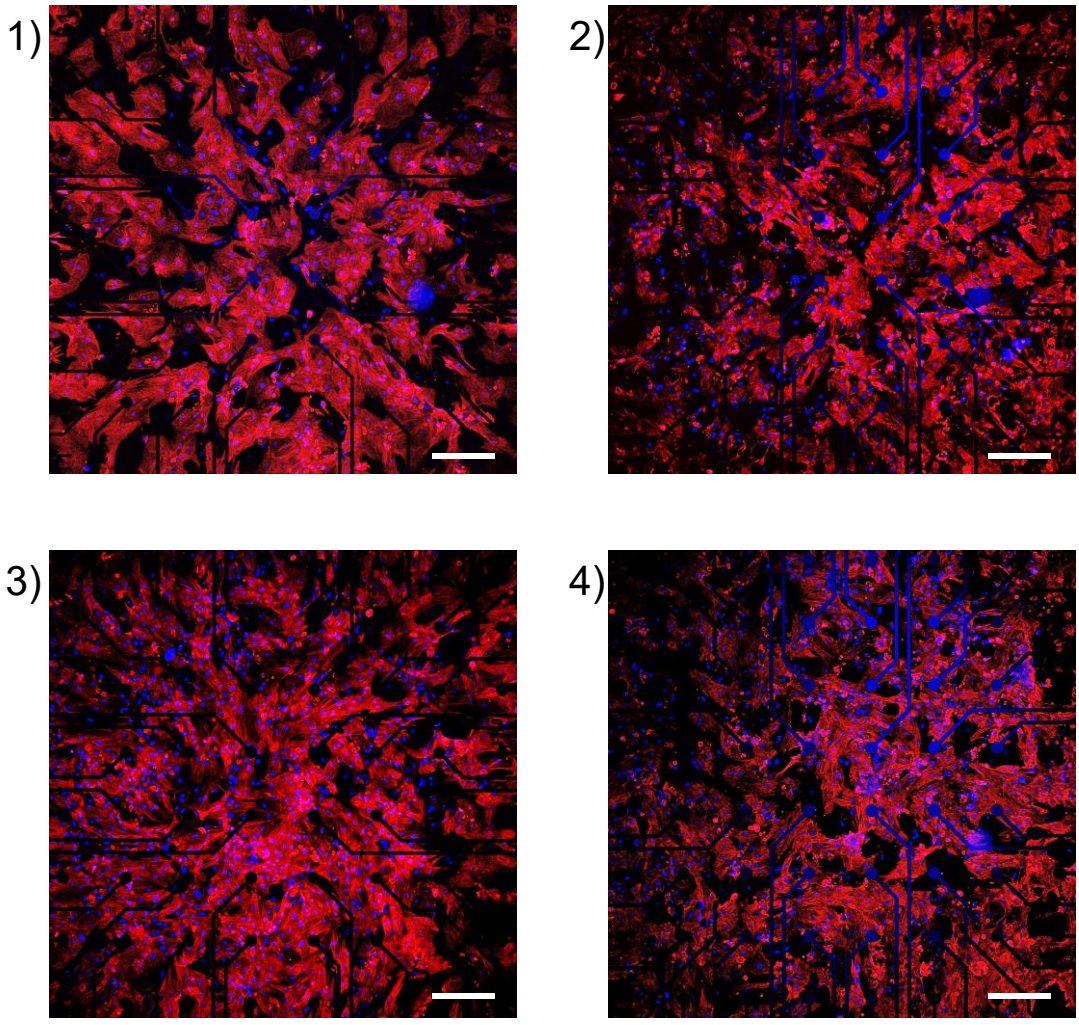


**Fig 2.18 Representative immunofluorescence images of cardiomyocytes cultured on MEAs under different experimental conditions**. 1) control (C), 2) doxorubicin-treated (D), 3) hAFSC-EVs-treated (E), and 4) combined treatment (ED). Cells were stained for α-sarcomeric actinin (red) to visualize sarcomeric organization and with Hoechst 33342 (blue) to label cell nuclei. No major qualitative differences in overall cellular morphology or sarcomeric structure are observed among the different conditions within the experimental timeframe. Scale bar: 200 μm.

### 2.2.4 Discussion

In this paragraph, the AFM–MEA platform described in paragraph 2.1 was employed to evaluate the cardioprotective effects of extracellular vesicles derived from human amniotic fluid stem cells (hAFSC-EV) against doxorubicin (Dox)-induced cardiotoxicity, in an *in vitro* murine cardiac model, where Doxo was administered at a pro-apoptotic concentration of 1 μM for 21 hours.

The results demonstrate that doxorubicin induces significant functional alterations in cardiomyocytes, affecting both electrophysiological and mechanical aspects of cellular activity. In particular, Dox treatment significantly altered contraction force amplitude, contraction velocity, contraction amplitude, refractory period, field potential amplitude, inter-beat interval, field potential duration, and depolarization speed. These alterations are consistent with the well-known cardiotoxic effects of doxorubicin, which has been reported to impair cardiomyocyte contractility and electrical stability through mechanisms involving oxidative stress, mitochondrial dysfunction, and alterations in calcium handling [151].

Importantly, the obtained results show that hAFSC-EVs exert a measurable cardioprotective effect in this model. In particular, EV treatment significantly mitigated the Dox-induced impairment of the contractile parameters, restoring values of contraction force amplitude, contraction velocity, and contraction amplitude closer to those observed in control cells. These findings suggest that the protective action of hAFSC-EVs primarily targets mechanisms involved in mechanical contraction and intracellular force generation.

No evidence of an effect of EV treatment on electrophysiological activity was observed, suggesting that the hAFSC-EVs cardioprotective effect predominantly involves the contractile function of cardiomyocytes.

Regarding the cardiotoxic effects of Dox and the potential cardioprotective role of hAFSC-EVs on cardiomyocyte mechanical properties, the limited number of analyzed cells does not allow drawing statistically robust conclusions. At this stage, the results should therefore be interpreted as descriptive, highlighting observed trends rather than definitive effects.

Nonetheless, we consider the ability to probe these mechanical (dynamic) parameters highly valuable. Further investigation in this direction could provide a more comprehensive and integrated understanding of cardiotoxicity, ultimately contributing to more robust assessments of both damage mechanisms and potential protective strategies.

**Mechanism of EV-mediated cadioprotection**

Taken together, these observations suggest that hAFSC-EVs may support cardiomyocyte resilience primarily by preserving contractile performance even in the presence of persistent electrophysiological alterations.

A possible explanation for this differential effect may lie in the cellular mechanisms targeted by extracellular vesicles. Doxorubicin is known to induce mitochondrial damage and increase the production of reactive oxygen species (ROS), leading to impaired ATP production and energetic failure [162]. Because cardiomyocyte contraction is an energy-demanding process, preservation of mitochondrial function could allow cells to maintain mechanical performance despite electrophysiological disturbances. Extracellular vesicles are known to carry bioactive molecules, including microRNAs, proteins, and signaling factors, which can modulate intracellular pathways involved in oxidative stress response and metabolic regulation [163].

In addition, cardiomyocyte contraction critically depends on efficient calcium cycling within the cell. Doxorubicin has been shown to disrupt calcium handling by affecting proteins such as SERCA pumps and ryanodine receptors, leading to impaired excitation–contraction coupling [169],[170]. EV-derived molecules may help support calcium homeostasis and improve the efficiency of calcium cycling, thereby contributing to the preservation of contractile force generation. Furthermore, doxorubicin has been reported to induce structural alterations in the cytoskeleton and sarcomeric organization of cardiomyocytes [171],[172],[173]. EV-mediated stabilization of cytoskeletal structures and sarcomeric components could therefore contribute to maintaining mechanical shortening and force development during contraction.

**Added value of the AFM–MEA single-cell approach**

With the proposed combine measurement approach it was possible to simultaneously and synchronously monitor electrical activity and mechanical contraction of the same individual cardiomyocyte. This allowed the identification of a dissociation between electrophysiological alterations and contractile recovery in EV-treated cells, highlighting that cardiomyocyte contractile function may be partially preserved even when electrical parameters remain altered.

This approach also allows direct observation of how electrical excitation is translated into mechanical contraction in individual cardiomyocytes. In heterogeneous cell cultures, the functional properties of cardiomyocytes may vary substantially due to differences in maturation state, metabolic condition, or microenvironment. Population-level measurements

inherently average these differences, potentially masking important functional behaviors. By contrast, single-cell measurements allow to capture the intrinsic variability of cellular responses and detect subtle functional alterations that may not be visible in averaged measurements. At the same time, robust interpretation of cardiotoxic and cardioprotective effects requires the integration of data from multiple cells. For this reason, a complementary analysis was performed at both the single-cell and population levels. While measurements were acquired at single-cell resolution to capture cell-to-cell variability, the responses were also integrated across all cells within the same experimental condition and across independent experiments to ensure statistical reliability. This strategy combines the strengths of both approaches: the *high-resolution insight of single-cell analysis* and the *statistical robustness of population-level evaluation*.

**Model limitations and future perspectives**

A factor to consider in the interpretation of the results is the intrinsic biological variability of the cellular model I employed. Although primarily composed of ventricular cardiomyocytes, primary cultures derived from neonatal mouse hearts represent a heterogeneous population that may also include atrial cardiomyocytes, which exhibit distinct electrophysiological and contractile properties. Furthermore, differences between individual animals used for cell isolation may contribute to variability between experimental sessions. The extracellular vesicles used in this study were also derived from human amniotic fluid stem cells obtained from different donors, and variations in donor characteristics may influence the molecular cargo of the vesicles. By pooling measurements obtained from multiple cells and independent experimental sessions, the analysis captures overall functional trends rather than the behavior of isolated experimental replicates, providing a more robust assessment of the cardiotoxic and cardioprotective effects under investigation.

Another aspect to take into account is the use of murine cardiomyocytes. They represent a widely used and experimentally robust system for studying the cellular mechanisms underlying cardiac physiology and drug-induced cardiotoxicity. Primary neonatal mouse cardiomyocytes exhibit stable culture conditions, spontaneous contractile activity, and reliable electrophysiological signals, making them particularly suitable for approaches that require precise mechanical and electrical measurements at the single-cell level.

However, murine cardiomyocytes differ from human cardiomyocytes in several physiological aspects, including beating frequency and ion channel expression profiles. As a consequence, while murine models provide valuable mechanistic insights, their direct translational relevance to human cardiac physiology may be limited [25],[26]. Human cardiac

models based on induced pluripotent stem cell-derived cardiomyocytes (hiPSC-CMs) are increasingly used in cardiotoxicity studies because they allow investigation of human-specific responses and patient-specific genetic backgrounds. Nevertheless, hiPSC-derived cardiomyocytes also present limitations related to incomplete maturation and functional variability. In this context, the use of primary murine cardiomyocytes in the present work provided a reliable platform for developing and applying the AFM–MEA methodology, which could in future studies be extended to human-derived cardiac models.

Finally, the present study was conducted using a planar (2D) culture of cardiomyocytes. While three-dimensional cardiac tissues and engineered heart constructs offer improved physiological resemblance to native myocardium, the use of a 2D system was dictated by the requirements of the AFM–MEA platform [174]. The combined AFM–MEA approach requires direct mechanical access to individual cells in order to perform simultaneous electrical and mechanical measurements. In a monolayer culture, cardiomyocytes remain accessible to the AFM probe while their electrical activity can be recorded through the underlying planar microelectrodes. This configuration allows precise positioning of the cantilever and high-resolution characterization of electromechanical behavior at the single-cell level. In thicker three-dimensional tissues, direct interrogation of individual cells using AFM becomes considerably more challenging because the probe can only access superficial layers of the construct. Nevertheless, future developments may explore the integration of AFM–MEA measurements with three-dimensional cardiac tissues, potentially enabling the investigation of tissue-level electromechanical behavior while still preserving some degree of mechanical characterization at the surface.

# Chapter 3 - Integrated TFT-MEA/MPA Platform for *In Vitro* Cardiac Studies

The AFM–MEA platform described in the previous chapter enables a detailed investigation of cardiomyocyte electromechanical activity at the single-cell level. While this approach provides highly precise functional characterization, it is inherently limited in terms of throughput.

To address this aspect - with the loss of single cell resolution – this chapter introduces an alternative experimental strategy based on the integration of Thin-Film-Transistor Microelectrode Arrays (TFT-MEA) with Micro-Pillar Arrays (MPAs). This combined platform is designed to enable the simultaneous and quantitative assessment of both electrical and contractile activity across multiple cells within the same culture.

This chapter presents the experimental system I developed during a six-months research visit to the laboratory of Professor Agnès Tixier-Mita at the Institute of Industrial Science (IIS), University of Tokyo. In addition, few preliminary results are reported to verify the feasibility of simultaneously measuring the electrical and contractile activity of cardiomyocytes in a two-dimensional *in vitro* model.

In particular, my work primarily focuses on the integration and implementation of the MPA component within the TFT-MEA device already developed by Prof. Tixier-Mita's group [175],[176].

## 3.1 Introduction

In the following paragraphs the principles of TFT and MPA technologies are first briefly described, then the integrated TFT-MEA/MPA platform is presented.

*Thin-Film Transistor (TFT)*

Thin-film transistors (TFTs) are a class of metal–oxide–semiconductor field-effect transistors (MOSFETs) fabricated by depositing thin layers of semiconducting and insulating materials onto a substrate [177]. The first TFT was demonstrated in 1962, only two years after the invention of the MOSFET, but its development and optimization saw a breakthrough in the late 1970s with the development of hydrogenated amorphous silicon (a-Si:H), which enabled stable, uniform large-area devices.

This innovation later allowed the commercialization of the first active-matrix liquid crystal displays (TFT-LCDs) in 1989 [178]. From then on, TFTs underwent several improvements thanks to the adoption of new semiconducting materials such as polycrystalline silicon (poly-Si), organic semiconductors, and indium gallium zinc oxide (IGZO), which combines high mobility, optical transparency, and reduced power consumption [179].

From a technological perspective, TFTs offer several advantages: their fabrication relies on relatively simple, low-temperature processes, enabling large-scale production at low cost, and the possibility to fabricate them on transparent and flexible substrates, such as glass and plastic, broadens their applicability. Furthermore, TFTs are produced exclusively through deposition steps, unlike CMOS technology, which relies on crystalline substrates and high-temperature processes [176],[180]. Their main limitation, however, lies in the reduced carrier mobility compared with CMOS transistors, due to the amorphous or polycrystalline nature of deposited semiconductor films, which limits their speed and current drive.

Such drawbacks are less critical in large-area and low-power applications, where transparency and substrate flexibility are prioritized [181].

Nowadays, TFTs have become key components for display, physical, and chemical sensing technologies. They are applied in various fields: in displays (especially TFT-LCDs and high-resolution X-ray detectors) [182], in physical sensors (touch screens, e-skin for robotics, IR sensors for thermal imaging and environmental monitoring), and in (bio-)chemical sensors (functionalized OTFTs, ISFETs for pH measurements, conductive polymer sensors for gases and “electronic noses”) [183],[184].

In particular, thanks to their transparency, scalability, and addressability, TFTs present unique opportunities for integration with biological systems and have recently emerged as promising platforms in bioelectronics research [185],[180].

*Micro-Pillar Arrays (MPAs)*

Micro-Pillar arrays are structured surfaces composed of numerous pillars with nano-, micro-, or sub-millimeter dimensions, arranged either in regular or custom patterns depending on the application. They were first introduced in 2003 by Tan et al. to address a fundamental question in mechanobiology: how do cells generate and transmit forces to their substrate, and how are these forces distributed and correlated with cell adhesion and morphology [186]. The most common use of MPAs is the quantitative measurement of cellular forces: cells are cultured on the arrays, and the forces they exert cause individual pillars to deflect. By the measurement of pillar deflection it is then possible to estimate the force [187],[53]. A prominent application involves assessing the contractile forces generated by cardiomyocytes during contraction. MPAs thus represent a powerful tool for evaluating cardiomyocyte functionality [188],[52]. Moreover, since the shape, geometry, spacing, and stiffness of the pillars can be precisely tuned, micropillar arrays allow researchers to

reproduce *in vitro* the mechanical conditions that cells encounter *in vivo* and quantitatively analyze how cells respond to different mechanical cues [189]. Among their mechano-sensing applications, these devices are widely used to study focal adhesions and associated proteins, which play a critical role in force transmission and mechano-transduction within cells. Other applications include investigating hemodynamic and trans-endothelial flow–associated forces acting on epithelial cells [190], as well as exploring cell migration, morphogenesis, and proliferation. MPAs influence cell shape and organization, providing a model for studying morphogenetic processes [191]; they enable modulation of substrate mechanical properties and quantitative analysis of how such properties regulate proliferation via mechanosensitive signaling pathways [192]; finally, they also allow detailed investigation of migration mechanisms by revealing how topography guides and directs cell movement [193].

Most MPAs are fabricated from elastomers such as PDMS, thanks to its excellent biocompatibility and mechanical properties that closely resemble those of biological tissues, creating a favorable environment for cells [194],[195]. Replica molding is one of the most widely used fabrication methods for these devices due to its simplicity, cost-effectiveness, and flexibility [196],[197]. However, other fabrication techniques have also been employed, including inkjet printing, which is highly versatile and compatible with a broad range of materials beyond polymers (such as metals and ceramics) [198], photopolymerization [199], and electrochemical deposition methods [200].

In Section 3.2 – Materials and Methods, the main components of the experimental set-up are presented, including the two principal modules for acquiring electrical and contractile properties, along with the procedures for data acquisition, analysis, and experimental measurements. In Section 3.3 – Results, the functionalities of the new contractile recording module are presented, together with preliminary experimental results obtained using the hybrid device.

## 3.2 Materials and Methods

The experimental platform developed and tested combines a Thin-Film-Transistor Microelectrode Array (TFT-MEA) with Micro-Pillar Arrays (MPAs) to enable the simultaneous measurement of electrical and contractile activity in a two-dimensional *in vitro* cardiac model. The system integrates electrical and optical acquisition components within a controlled environmental chamber, allowing stable and reproducible measurements under physiological conditions.

1. Set-Up Components

In addition to the core component of the platform—the hybrid TFT-MEA/MPA device—the setup includes the following elements:

- **Mini-incubator**: custom chamber designed to maintain stable environmental conditions during measurements.
- **Temperature Controller**: used to maintain the temperature of the mini-incubator at 37 °C, ensuring physiological conditions for cardiomyocyte viability and function.
- **$CO_2$ supply system** : used to regulate the gaseous environment inside the mini-incubator, maintaining appropriate $CO_2$ levels and physiological conditions, particularly during long-term experiments.
- **Inverted microscope (Olympus® IX71)**: used for optical visualization of the culture and acquisition of contractile activity.
- **Photometrics Cascade II:512**: black and white camera, used for real-time imaging and video recording of micropillar displacement.
- **Multi Channel Systems USB-ME32-FAI**: acquisition unit allowing electrical recordings from up to 32 channels at a sampling frequency of 10 kHz. Signals are transferred to the host computer via USB 2.0. The device is connected to the TFT-MEA source terminals for recording cellular electrical activity.
- **MC_Rack Software**: proprietary MCS software platform for data acquisition and analysis, allowing real-time visualization and storage of signals recorded via the USB-ME32-FAI in *.mcd* format.
- **JAPASTIM Control Card**: custom electronic interface developed by the research group of Prof. Tixier-Mita, enabling sequential addressing of the different TFT-MEA transistors, by controlling the on/off state of the gate lines.

**Thin Film Transistor – Microelectrode Array (TFT-MEA)**

The electrical TFT-MEA component of the hybrid platform was developed and described in previous studies (Fig 3.1) [185],[175], and consists of a 22,500 transparent Indium Tin Oxide (ITO) microelectrodes (Sharp® Corporation, Japan), fabricated on a 27 mm × 25 mm glass substrate. Each electrode has the size of 100 µm × 100 µm, forming a 150 × 150 pixel matrix that covers an active area of 15 mm × 15 mm. Each electrode is individually addressed and controlled by an integrated thin-film transistor (TFT).

The TFTs have a channel length of 3.63 µm and a channel width of 4.65 µm.

Each transistor displays a low-pass filter characteristic with a cut-off frequency of approximately 7 kHz when a gate voltage of 12 V is applied. The impedance of each channel is approximately 2 MΩ [201],[202].

The TFT-MEA substrate is mounted onto a custom-designed Printed Circuit Board (PCB), perforated at the center to accommodate the glass substrate while preserving optical transparency of the final device. Electrical connections between the TFT pads and the PCB pads are established via wire bonding. To protect the bonding wires, a layer of polydimethylsiloxane (PDMS) is applied, which also serves as an adhesive for attaching a square-shaped PDMS chamber (2 cm × 2 cm) with a central circular well (diameter 1.6 cm) for cell culture containment.

Each TFT consists of three terminals: gate, source, and drain. Gate terminals are column-parallel connected, while source terminals are row-parallel connected. The drain terminal of each transistor is directly connected to the corresponding ITO electrode (Fig 3.2). By applying a voltage (12 V) to a selected gate line (column), all TFTs in that column are switched ON.

When a recording or stimulation system is connected to the source lines (rows), this configuration allows sensing or stimulation at the intersection of the selected gate–source lines, through the drain-connected microelectrode. This configuration enables independent addressing of each electrode within the array.

The JAPASTIM control board, connected to the gate lines, regulates the ON/OFF status of each gate channel by sequentially addressing them at a frequency of 0.2 Hz. When operating in sensing mode, electrical signals detected at the ITO electrodes are acquired through the USB-ME32-FAI system, connected with the source lines.

**Micro-Pillar Array (MPA)**

The MPA component was fabricated in polydimethylsiloxane (PDMS), using a 3D printing technique based on two-photon polymerization (2PP, Nanoscribe GmbH), by Dr. Gilgueng Hwang (Dept. of Electrical Engineering and Information Systems, The University of Tokyo), based on the design developed within this work.

Specifically, a photopolymerizable PDMS-based resin (IP-PDMS) was directly deposited onto the TFT-MEA substrate. The final structure was then precisely printed by following a CAD-defined trajectory of the laser focal point. Each array consisted of a 16 × 16 (256) matrix of micropillars (diameter Ø = 4 μm, height H = 12 μm, distance D = 18 μm), anchored to a 5 μm-thick PDMS base layer to improve adhesion to the underlying TFT-MEA device.

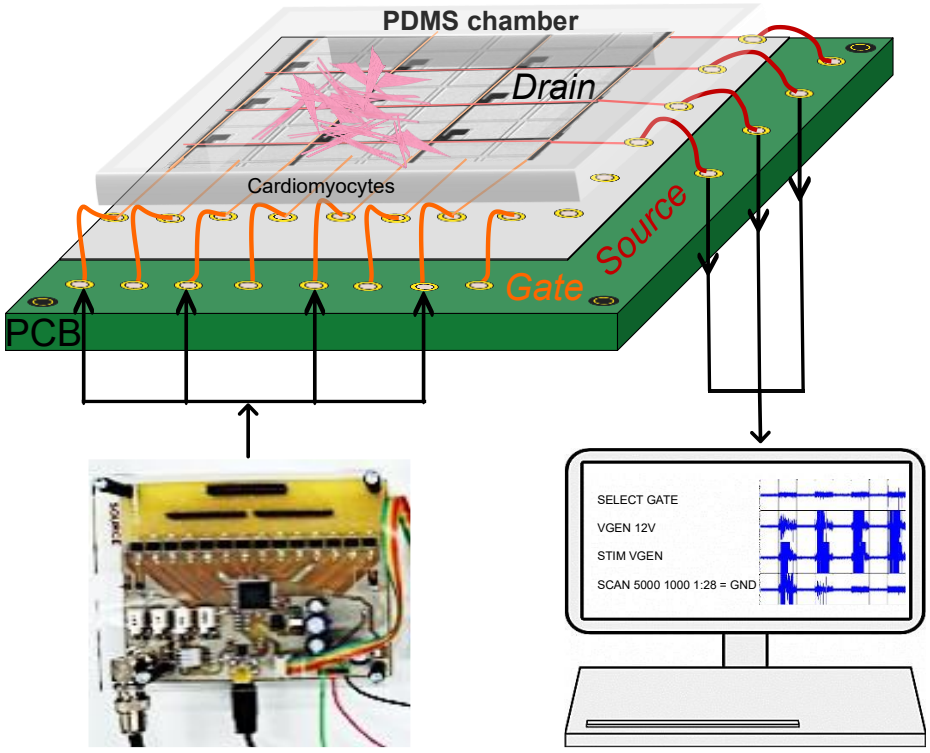


**Fig 3.2 Schematic representation of the TFT-MEA experimental platform.** The system consists of a hybrid TFT-MEA device integrated on a printed circuit board (PCB) with a PDMS chamber for cell culture, allowing the growth and measurement of cardiomyocytes. Each electrode is addressed through the thin-film transistor architecture via gate and source lines, enabling sequential activation and signal acquisition. Electrical activity is recorded through the USB-ME32 FAI system (Multi Channel Systems), while the JAPASTIM control board is used to drive the gate lines and control the activation of the array. This configuration enables multiplexed electrophysiological recordings from the TFT-MEA platform.

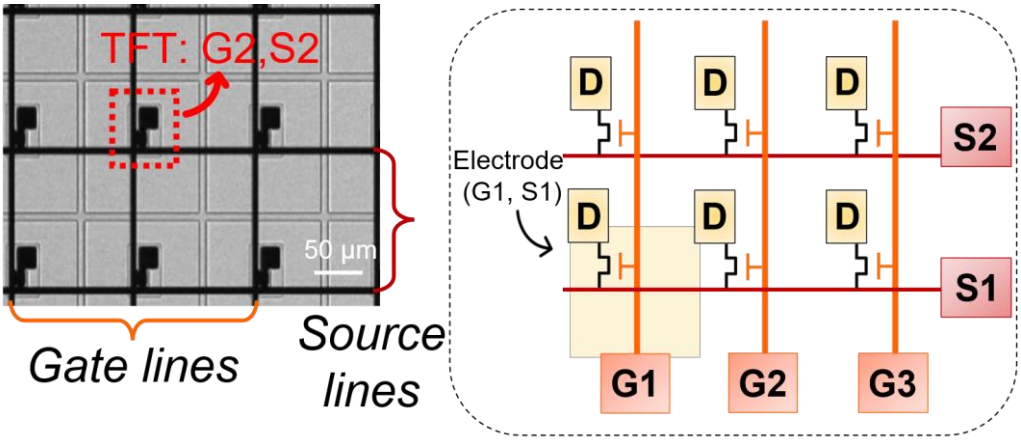


**Fig 3.1 Optical image (left) and schematic representation (right) of the TFT-MEA architecture.** The optical image highlights the arrangement of microelectrodes and thin-film transistors, with gate and source lines defining the matrix structure. The schematic illustrates the addressing principle of the array: gate lines (G) are column-connected, while source lines (S) are row-connected, and each electrode is connected to the drain terminal of a transistor. By activating a selected gate line and reading from a specific source line, individual electrodes at the gate–source intersection can be selectively addressed, enabling multiplexed recording from the array.

The mechanical properties of individual micropillars were estimated by applying beam bending theory, which describes the deflection of cantilever-like structures subjected to lateral loads [203]. In this framework, the spring constant *k* of each micropillar is given by:

$$k = \frac{3\pi E Ø^4}{64H^3},$$

where *E* is the Young's modulus of the material, *H* the pillar height (12 µm), and Ø the pillar diameter (4 µm). In this work, a soft and highly flexible PDMS-based resin (Nanoscribe GmbH), with a reported Young's modulus of *E* = 15 MPa was used for fabrication.

Fig 3.3 shows representative images of the MPAs at different magnifications, together with their geometric layout.

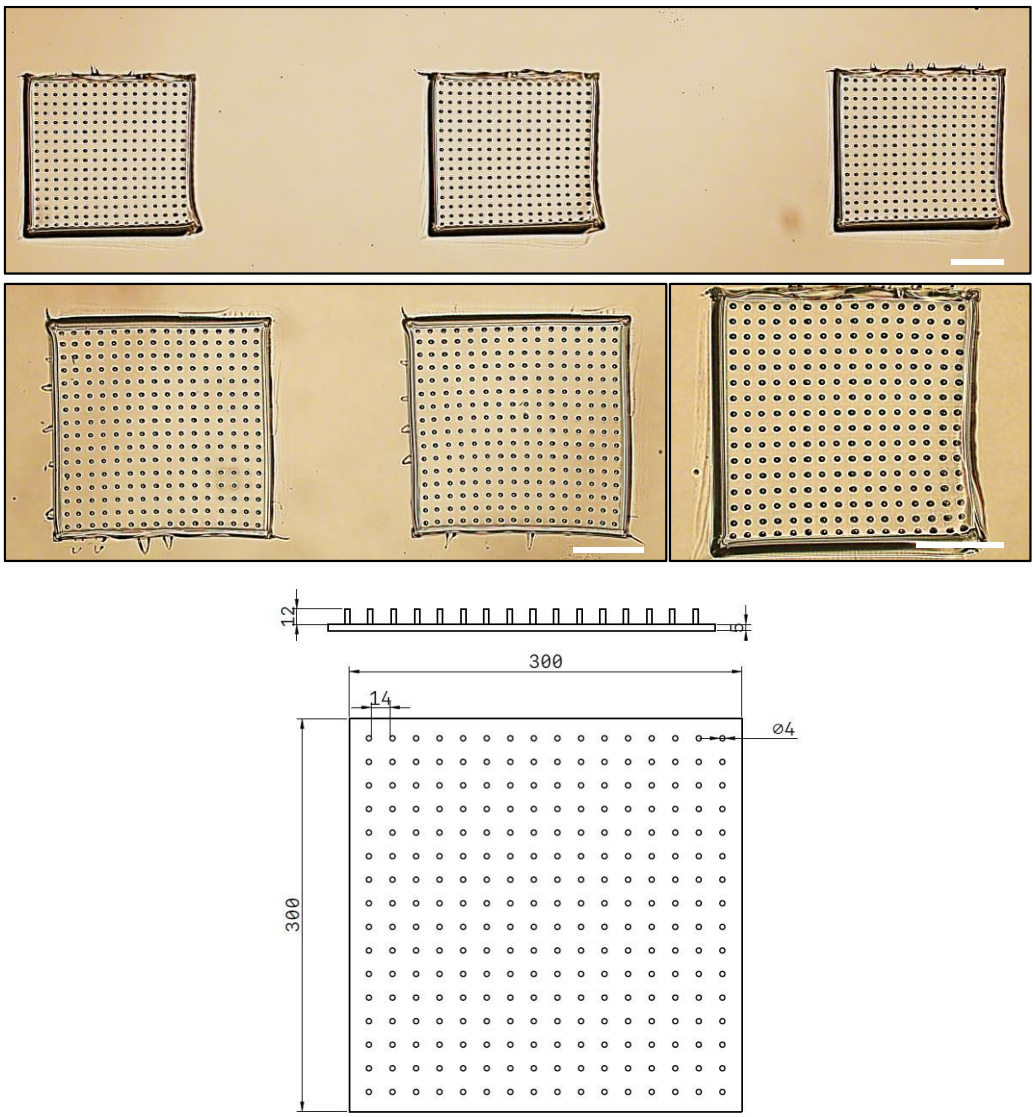


**Fig 3.3 Representative optical images of the PDMS micropillar arrays at different magnifications (top), and schematic illustration of their geometric layout (bottom).** The arrays consist of a regular 16 × 16 matrix of micropillars fabricated by two-photon polymerization, each characterized by a diameter of 4 µm, a height of 12 µm, and an inter-pillar spacing of 18 µm. The micropillars are anchored to a thin 5 µm PDMS base layer to ensure stable integration with the underlying substrate. Scale bars: 100 µm.

2. Cell Culture

To test the experimental platform, a two-dimensional *in vitro* cardiac model was employed. The isolation of cardiomyocytes was performed at the University of Tokyo Hospital, thanks to the collaboration with Prof. Katsuhito Fujiu and Prof. Junichi Sugita of the Department of Cardiology. Briefly, cardiomyocytes were isolated from neonatal mouse hearts and dissociated into a single-cell suspension. Cardiac tissue was enzymatically digested using the Pierce™ Primary Cardiomyocyte Isolation Kit (Thermo Scientific Pierce), which degrades the extracellular matrix and facilitates cell dissociation. This step was followed by gentle mechanical dissociation using a MACS Dissociator.

The resulting cell suspension was filtered to remove residual tissue fragments and subjected to red blood cell lysis. Isolated cardiomyocytes were then resuspended in complete culture medium and seeded onto the TFT-MEA/MPA device.

The complete culture medium consisted of Dulbecco's Modified Eagle Medium (DMEM, Gibco, Thermo Fisher Scientific), supplemented with 9% Fetal Bovine Serum (FBS, Sigma-Aldrich), and 1% Penicillin-Streptomycin (Pen/Strep, Gibco, Thermo Fisher Scientific) to prevent bacterial contamination.

Substrate preparation and cell seeding

Before seeding, the hybrid TFT-MEA/MPA platform underwent cleaning, surface activation, sterilization and coating procedures:

- *Surface activation*: The platform was rinsed with deionized water and treated with oxygen plasma for 1 minute to increase the hydrophilicity of the PDMS micropillars. Plasma exposure was confined to the active recording area (see "Data acquisition" below) by placing a PDMS mask with a ~6 mm diameter central opening onto the device, thereby limiting activation to the region containing the MPAs and the selected electrodes.
- *Sterilization:* The device was sterilized by immersion in 70% ethanol for 30 minutes, followed by 1h of ultraviolet (UV) exposure.
- *Adhesion coating*: To improve cell attachment, the device was incubated overnight at 4 °C with a fibronectin solution (1:20 in PBS). A 60 µL drop of the coating solution was applied to the active region of the platform.
- *Cell seeding*: After removing the coating solution, a 60 µL droplet of cell suspension was deposited onto the active area at a density of 3500 cells/mm². This density was chosen to promote the formation of a functional syncytium and uniform coverage across both the TFT-MEA and MPA regions.

- *Initial incubation*: five hours after seeding, once cells had adhered, 900 µL of complete medium was added and the device was returned to the incubator.
- *Medium exchange*: after 24 hours, the culture was washed with fresh medium to remove debris and dead cells. Subsequently, the medium was replaced every two days.
- Cells were maintained under standard culture conditions (37 °C, 5% $CO_2$, 20% $O_2$) and allowed to fully adhere and recover prior to experimental measurements.

3. Experimental Measurements

3.1. Micro-Pillar Arrays (MPAs)

Prior to fabricating the MPAs directly onto the TFT-MEA substrate, preliminary tests were performed on MPAs fabricated on ITO-coated glass substrates. These trials allowed validation of the MPA component and provided datasets for the development of the dedicated analysis algorithm (see subsequent section). Substrate preparation followed the same protocol used for TFT-MEA/MPA device, as describe in section 2 (Cell Culture).

Optical measurements were taken using the inverted microscope with a 40× objective. The focal plane was set on the top surface of the micropillars, and videos were acquired using the Olympus DP23 camera (30 fps) for each MPA within the ITO-coated glass substrate.

The microscope stage was temperature-controlled and maintained at 37 °C to ensure proper cellular function.

Pharmacological testing was performed using isoprenaline, a non-selective β-adrenergic agonist known for its positive chronotropic and inotropic effects [204],[205].

Data were collected at DIV6 under the following condition:

- ***Untreated***: The basal activity of the cells was recorded for one minute in order to evaluate their initial functional state.
- ***Treated***: The cells were treated with 60 nM Isoprenaline.

Following isoprenaline administration, new measurements were performed after 3 minutes, to allow the compound to evenly diffuse through the medium and for the cells to reach a new equilibrium.

3.2. Thin Film Transistor – Microelectrode Array / Micro-Pillar Array (MPA)

Before measurements, the mini-incubator was filled with water and connected to the temperature controller (37 °C) and $CO_2$ supply to maintain physiological conditions. The system was allowed to equilibrate for 5 minutes prior to data acquisition. During this equilibration period, all instrumentation required for the measurements was powered on, including the JAPASTIM control board and the MCS data acquisition system. The device

was subsequently removed from the incubator and mounted onto the mini-incubator using two screws to secure the platform in place, ensuring mechanical stability for subsequent cable connections (gate and source lines) and reducing external noise. An external reference electrode made of gold, was inserted into the culture medium prior to recording.

Once the platform was secured, the TFT-MEA/MPA system was connected to the instrumentation through the dedicated gate and source cables. The scanning of the gate channels was enabled while simultaneously recording data via MC_Rack. For these experiments, a total of 28 gate lines and 28 source lines were connected to the JAPASTIM control card and acquisition system, respectively, enabling electrophysiological recordings from 784 (28 × 28) electrodes. The selected electrodes were chosen to be adjacent to the micropillar arrays (MPAs), allowing the simultaneous recording of electrical and contractile activity from the same cell populations.

Within this TFT array system, each gate line was sequentially activated. The JAPASTIM control card was programmed to scan the 28 gate lines by switching them ON and OFF sequentially, with the following parameters: 5000 ms ON-time per gate channel, and a 1000 ms OFF interval between the deactivation of one gate channel and the activation of the next. During the entire gate scanning period, electrical signals were recorded through the MCS acquisition system, at 10 kHz sampling rate, and stored via MC_Rack. In this configuration, 5 seconds of electrical activity were recorded from 784 distinct recording sites. Pre-processing in MC_Rack applied the following filters to the raw data:

- FILTER 1: Bandstop Resonator (f = 50 Hz, Q = 1.0)
- FILTER 2: Butterworth 2$^{nd}$ order (High Pass, f = 5 Hz)
- FILTER 3: Butterworth 2$^{nd}$ order (Low Pass, f = 1500 Hz)

Simultaneously with electrical recordings, optical displacement of the micropillars was acquired. Using the IX71 inverted microscope (Olympus® Corporation) with a 60× objective, the focal plane was set on the free ends (top surface) of the micropillars within the current MPA region. Videos were captured with the Photometrics Cascade II:512 camera (10 fps), providing optical recordings for each MPA within the TFT-MEA array.

Data were collected at DIV6 under the following conditions:

- ***Untreated*:** The basal activity of the cells was recorded for one minute in order to evaluate their initial functional state.
- ***Treated*:** The cells were treated with 20 nM Isoprenaline.

Following drug administration, a 3-minute equilibration period was allowed to ensure homogeneous diffusion of the compound and stabilization of the cells before subsequent measurements.

4. Data Analysis

Electrical Signal

Raw data acquired with MC_Rack (.mcd format) were converted into ASCII format using Multichannel Suite DataManager and then imported into MATLAB for further processing. Each file contained a time vector and multiple voltage traces corresponding to the selected source channels (up to 32 channels).

For each source channel, signals corresponding to sequentially scanned gate lines were extracted, allowing reconstruction of electrode-specific recordings.

Each signal contained artifacts associated with the commutation of the corresponding gate line, which were identified to allow isolation of electrode-specific signals. Signals were processed using custom-developed MATLAB routines (The MathWorks, Natick, MA, USA): signal was segmented to isolate individual electrode recordings and converted to the desired units (time [ms], voltage [μV]). This resulted in 784 (28 × 28) recording sites with their associated extracellular field potential signals. From the extracellular field potential signal the following electrical parameters (as defined in paragraph 2.1) were extracted:

- Interbeat Interval – Electrical (IBI-E)
- Field Potential Peak-to-Peak Amplitude (PPA)
- Field Potential Duration (QT)
- Depolarization Speed
- Depolarization Duration.

Optical Signal

**Calibration of MPA image**

A reference image of the MPA (without cell) was processed in MATLAB through the following steps:

a) enhancement of pillar visibility, relative to the background.
b) identification of the centroid coordinates (x, y) of each pillar.
c) calculation of the Euclidean distance between neighboring centroids, expressed in pixels.
d) calculation of a pixel to μm conversion factor by comparing the measured inter-centroid distance in pixels with the inter-pillar spacing (known by design, D = 18 μm).

In more details, a reference image of the MPA without cells was first acquired to estimate the pixel-to-micrometer conversion factor. The image was then converted to a grayscale

image, normalized, and processed using frequency-domain filtering to remove low-frequency background components and enhance high-frequency details. Micropillars were automatically detected using a circular Hough transform (imfindcircles function in MATLAB), allowing identification of pillar centroids. A manual validation step was then performed to remove false positives. For the validated centroids, pairwise Euclidean distances were computed, and the distance to the nearest neighbor was extracted for each pillar.

Given the known inter-pillar spacing (D = 18 µm), the mean nearest-neighbor distance in pixels was used to determine the scale factor

$$s = \mu m/pixel$$

and consequently its reciprocal in pixels per micrometer (Fig 3.4).

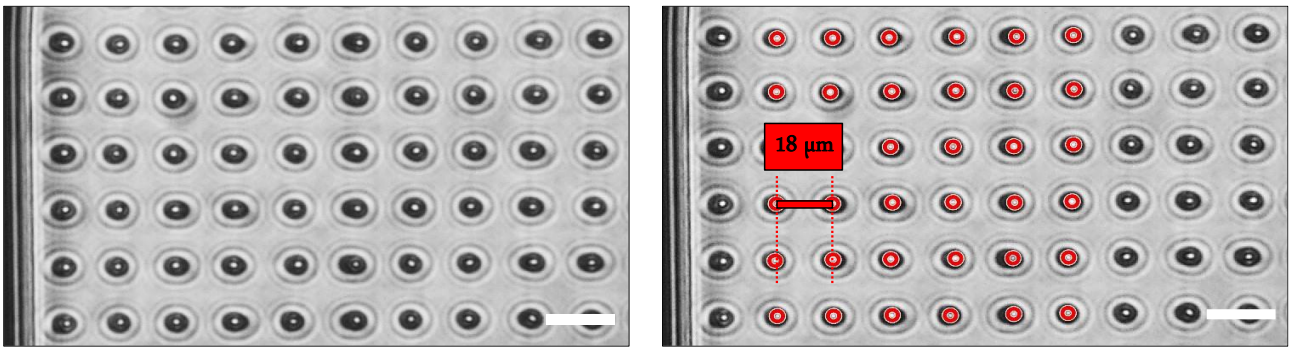


**Fig 3.4 Pixel-to-micrometer calibration procedure performed on a reference MPA image without cells**. After image preprocessing (grayscale conversion, normalization, and frequency domain filtering), micropillars are automatically detected using a circular Hough transform, and their centroids are identified. Pairwise Euclidean distances between neighboring centroids are computed, and the nearest-neighbor distance is used to derive the conversion factor (µm/pixel) based on the known inter-pillar spacing (D = 18 µm). Scale bar: 20 µm.

**Extraction of force signal from the recorded MPA video**

The analysis of the videos recorded during experiments to extract the force signals exerted on each micropillar was done through the following steps:

a) Importation of video recordings in *.avi* format.

b) Selection of the total number of frames to analyze.

c) Frame-by-frame analysis with image filtering to enhance contrast and highlight the top surfaces of the pillars relative to the background (substrate + cells).

d) Tracking of the centroid position of each pillar across frames.

e) *Calculation of displacement signal*: for each pillar, the Euclidean distance in pixels between its current centroid position and the centroid position in a reference resting frame was calculated. This displacement was then converted from pixels to micrometers using the previously determined calibration factor.

f) Time axis converted from frames to seconds.

g) *Calculation of force signal*: displacement (x) was converted into force (F) by applying Hooke's law (F = k·x), using the elastic constant *k* (k = 0.33 N/m) of the individual pillars.

In more details, video recordings were imported and analyzed frame by frame. Each frame was processed using filtering procedures (background subtraction, high-pass filtering, normalization, and contrast enhancement) to ensure reliable pillar detection.

As in the calibration step, false positives were manually removed in the first frame, leaving only the markers corresponding to real pillars (Fig 3.5).

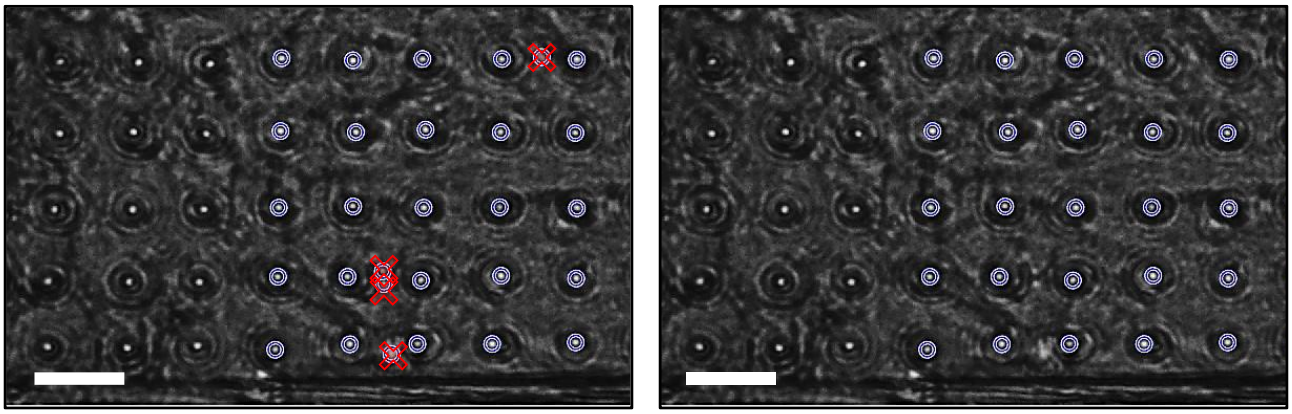

**Fig 3.5 Pillar detection and validation in video recordings of cardiomyocytes cultured on the MPA**. Following image filtering (background subtraction, normalization, and contrast enhancement), micropillars are automatically detected and their centroids identified. A manual validation step is performed in the first frame to remove false positives, retaining only reliable pillars for subsequent frame-by-frame tracking. The validated centroids are then used to compute displacement signals over time. Scale bar: 20 µm.

Pillar tracking was performed using a frame-by-frame approach: for each pillar, the centroid detected in the current frame was associated with the closest centroid in the previous frame, provided that the displacement was below a predefined threshold (10 px). This procedure yielded the trajectory of each pillar over time: $r(f) = [x(f), y(f)]$.

For each pillar, a reference resting frame was identified as the frame with minimal displacement. The corresponding resting position $\mathrm{r}_0$ was then used to compute the displacement amplitude $\Delta r = \| \mathrm{r}(f) - \mathrm{r}_0 \|$.

Displacements were converted from pixels to micrometers using the calibration factor, and the time axis was converted from frames to seconds.

Finally, the displacement signal was converted into force using Hooke's law $F(t) = k \cdot \delta(t)$, assuming a spring constant $k = 0.33$ N/m, derived from beam bending theory (Fig 3.6). Among all detected pillars, only those exhibiting a high signal-to-noise ratio (SNR) were retained for subsequent analysis.

The contraction force signal of each pillar was analyzed using the same algorithm described in paragraph 2.1 in order to extract the following parameters that describe the cell contraction:

- Contraction Force Amplitude
- Contraction Force Duration
- Contraction Force Velocity
- Refractory Period (tREF)
- Interbeat Interval – Contractile (IBI-C).

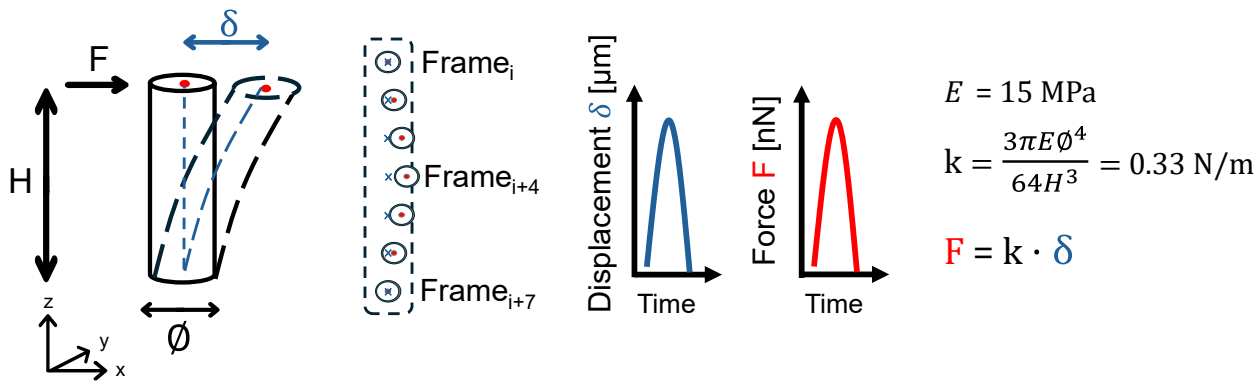


**Fig 3.6 Schematic representation of the micropillar-based force measurement principle**. A lateral force generated by cardiomyocyte contraction induces a deflection (δ) of the micropillar, modeled as a cantilever beam. The pillar displacement is tracked over time to obtain the displacement signal, which is then converted into force using Hooke's law (F = k·δ), where k is the spring constant of the pillar (k ≈ 0.33 N/m). This approach enables the reconstruction of time-resolved contractile force signals from pillar deflection.

## 3.3 Results

1. Preliminary Test with Micro-Pillar Arrays (MPAs)

Preliminary measurements were carried out with cardiomyocytes seeded onto PDMS MPAs fabricated onto indium tin oxide (ITO)-coated glass substrates in order to verify the possibility to monitor the contractile activity through micropillar deflection. Cells were cultured on the MPA substrate as described in the "Cell Culture" section. Cardiomyocytes successfully adhered to both the indium tin oxide (ITO) surface and the PDMS micropillars (Fig 3.7), generating measurable pillar deflections during their spontaneous contractile activity.

Cell Contraction Response to Isoprenaline Acute Exposure

To evaluate the capability of the MPA system to quantify changes in forces exerted by the cells, a simple pharmacological assay was performed. Cardiomyocytes were treated with 60 nM isoprenaline, and contractile activity was analyzed before and after drug administration following a 3-minute equilibration period.

Video recordings were processed to extract force signals from individual micropillars. Representative traces from three selected pillars are shown in Fig 3.8. One can observe a clear increase in the beating frequency after isoprenaline administration, consistent with its known positive chronotropic effect.

Quantitative analysis was performed on three different MPAs (MPA-1, MPA-2, and MPA-3) within the same culture. For each MPA, contractile parameters were extracted from all detected pillars, approximately 40 pillar per MPA, and represented as boxplots (Fig 3.9).

Differences in parameter distributions were observed both within individual MPAs (*intra-MPA* variability) and across different arrays (*inter-MPA* variability), indicating variability in contractile responses both across individual pillars and across different regions of the same culture.

To better represent the overall behavior of the culture, contractile parameters were also calculated by pooling all detected pillars within the same sample.

In particular, a marked reduction in the mean interbeat interval and refractory period was observed, together with a mean increase in contraction force amplitude and velocity, and a decrease in contraction force duration.

Moreover, isoprenaline administration induced a significant regularization of the *inter-MPA* behavior for the frequency-related parameters IBI and $t_{REF}$, resulting in a variability reduction of approximately 80% in both values. Conversely, the parameters derived from waveform morphology—namely amplitude, velocity, and duration—exhibited a lower degree of regularization. Variability reductions did not exceed 20% for contraction amplitude and duration, while contraction velocity, rather than becoming more regular, showed an increase in variability of approximately 25% (Table 3.1).

Similarly, regarding *intra-MPA* behavior, the positive chronotropic agent decreased the variability of the IBI and $t_{REF}$ parameters, while no corresponding reduction was observed for the parameters describing contraction amplitude, velocity, and duration.

Overall, these results demonstrate that the MPA platform enables reliable quantification of cardiomyocyte contractile dynamics and is sensitive to pharmacologically induced functional modulation.

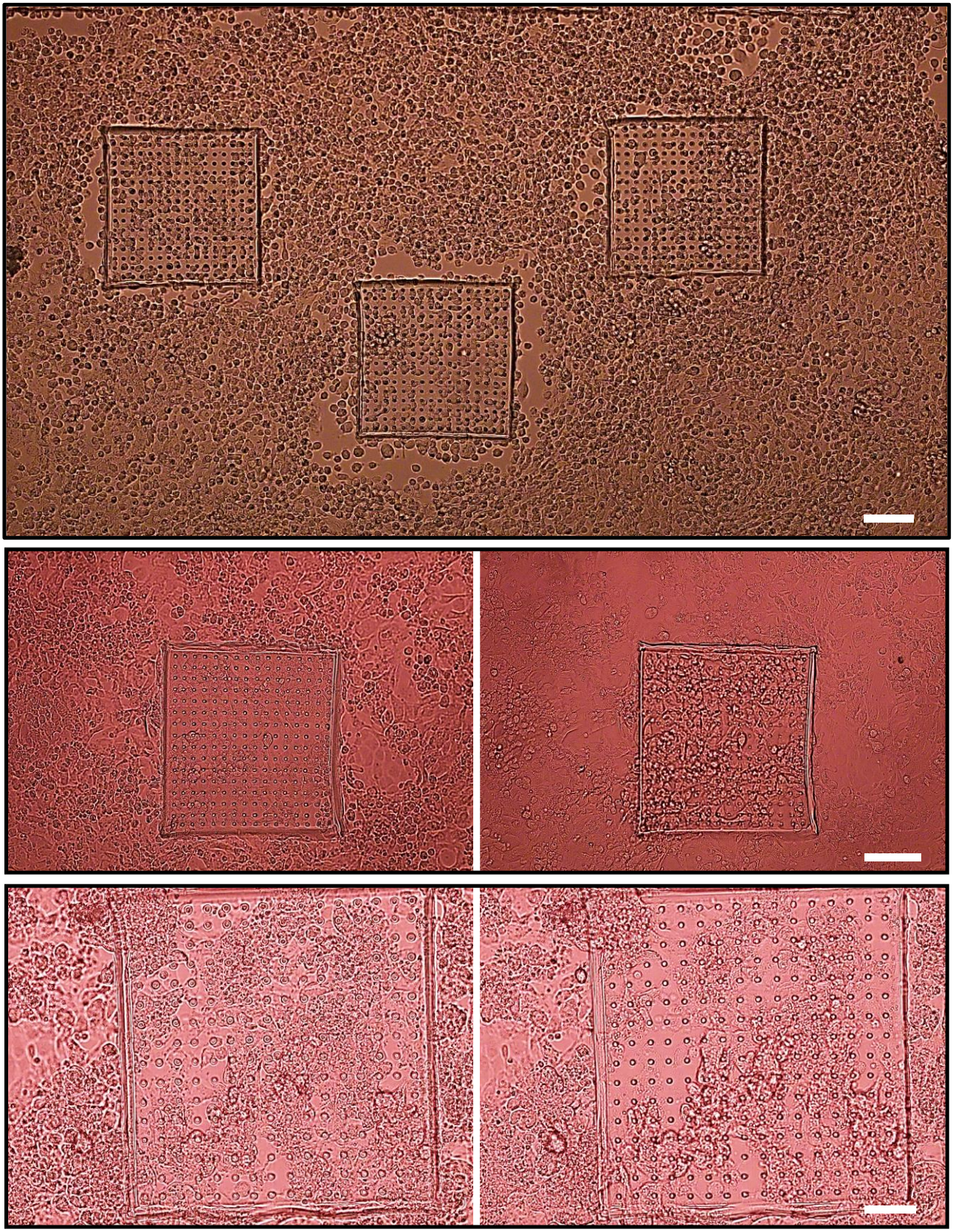

**Fig 3.7 Representative optical images of cardiomyocytes cultured on the PDMS micropillar arrays at different magnifications**. The images show the spatial distribution of cells across the array, highlighting how cardiomyocytes adhere and spread both on top of the micropillars and in the inter-pillar regions. This heterogeneous distribution reflects the interaction between cells and the underlying micro-structured substrate and contributes to variability in contractile responses across different regions of the array. Scale bars: top and middle panel, 100 μm – bottom panel, 50 μm.

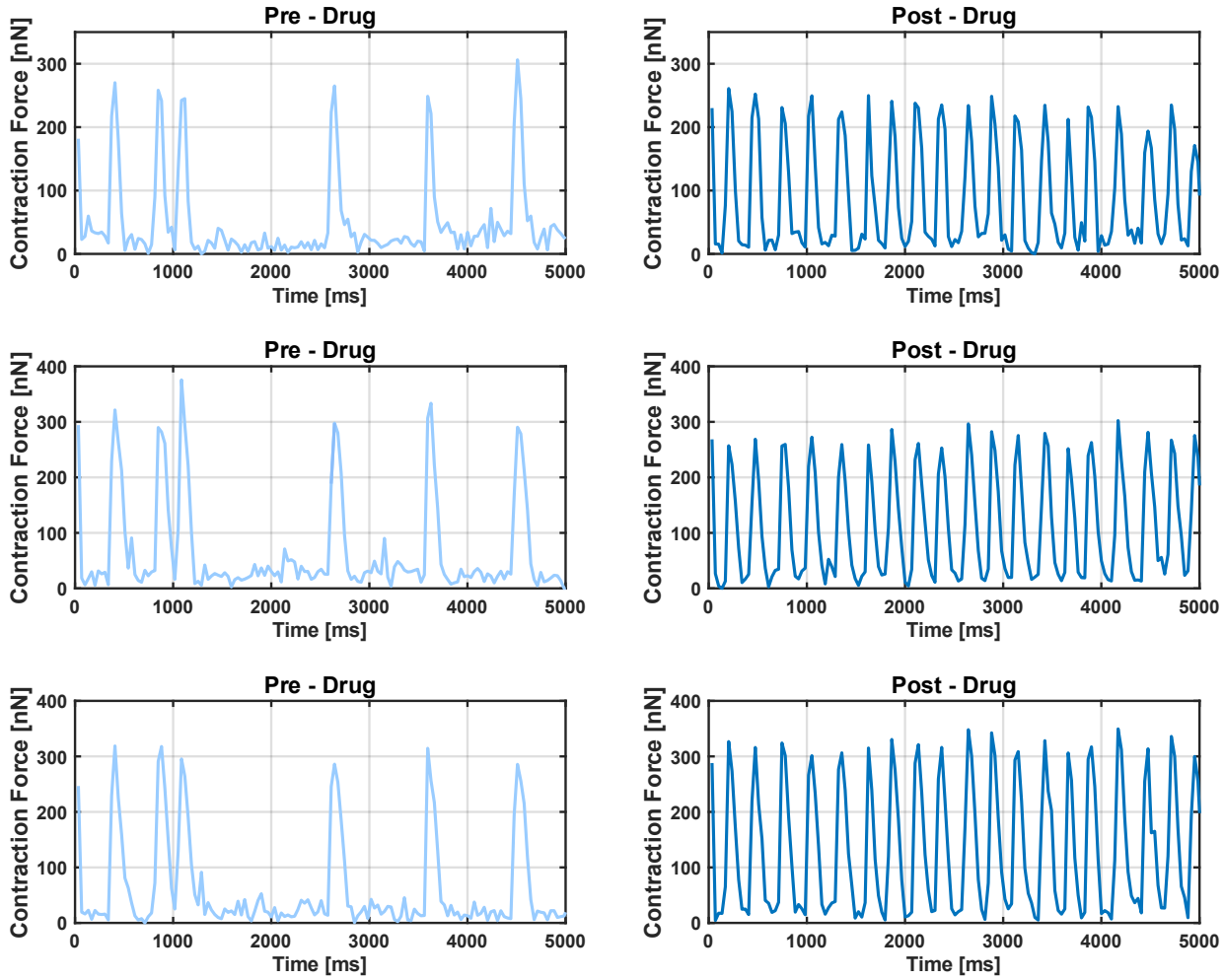


**Fig 3.8 Representative contractile force traces extracted from three individual micropillars before (Pre-Drug) and after (Post-Drug) administration of isoprenaline (60 nM).** Each row corresponds to a different micropillar, illustrating the variability of contractile activity within the same culture. Following drug administration, an increase in beating frequency and a more regular contractile pattern can be observed, consistent with the positive chronotropic effect of isoprenaline.

| PARAMETER | CONDITION | | | | RELATIVE VARIATION (%) | |
|---|---|---|---|---|---|---|
| | *Pre - Drug* | | *Post - Drug* | | | |
| | Mean | Std | Mean | Std | ΔMean (%) | ΔStd (%) |
| **Contraction Force Amplitude [nN]** | 206.13 | 84.86 | 211.86 | 68.54 | 2.78 | -19.22 |
| **Contraction Force Duration [ms]** | 97.77 | 25.79 | 81.02 | 21.98 | -17.13 | -14.75 |
| **Contraction Force Velocity [nN/ms]** | 2.67 | 2.22 | 4.01 | 2.78 | 49.78 | 25.97 |
| **Interbeat Interval (IBI_C) [ms]** | 694.93 | 381.21 | 248.36 | 39.47 | -64.26 | -89.64 |
| **Refractory Period (tREF) [ms]** | 527.57 | 383.01 | 101.42 | 46.44 | -80.77 | -87.87 |

**Table 3.1 Summary of contractile parameters extracted from micropillar (MPA) measurements before (PRE) and after (POST) 60 nM isoprenaline administration**. Reported values are mean ± standard deviation calculated across all analyzed micropillars. Relative variations (Δ %) between conditions are also reported. The results highlight the increase in contraction force amplitude and velocity, together with the reduction in interbeat interval and refractory period following drug stimulation. $\Delta\ (\%) = \frac{Value_{POST} - Value_{PRE}}{Value_{PRE}} \times 100$.

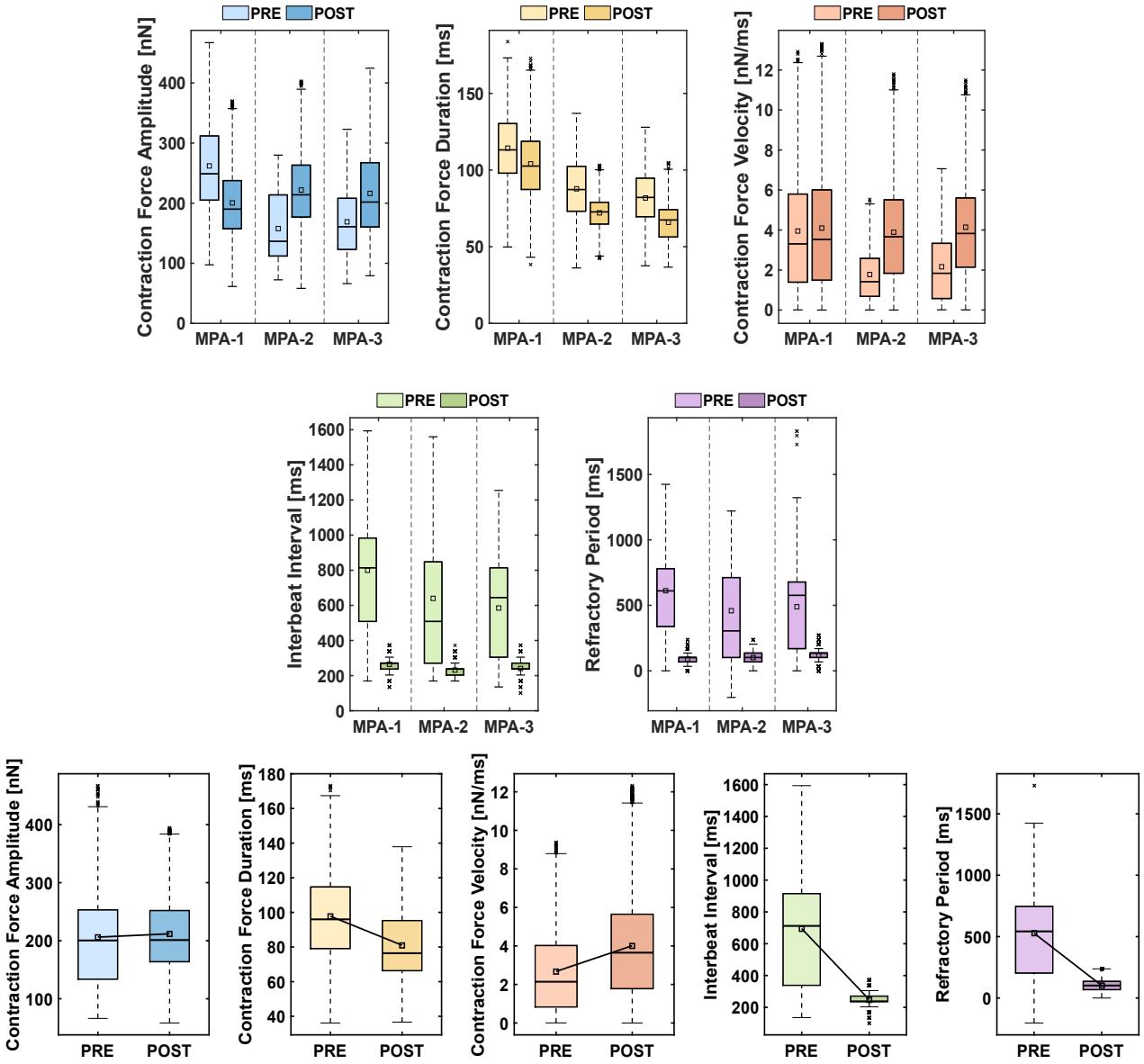


**Fig 3.9 Contractile parameter analysis before and after 60 nM isoprenaline administration**. Boxplots show the distribution of contractile parameters extracted from three different micropillar arrays (MPA 1, MPA-2, MPA-3) within the same cardiomyocyte culture, comparing baseline (PRE) and post treatment (POST) conditions following administration of 60 nM isoprenaline. In the upper panels, each boxplot includes data from all detected pillars within the corresponding MPA (MPA-1: $N_1$ = 50, MPA-2: $N_2$ = 30, MPA-3: $N_3$ = 30), with square markers indicating the mean value and data dispersion reflecting intra-MPA variability. In the lower panels, data are pooled across all MPAs to describe the overall culture response; square markers indicate mean values, while solid lines connecting PRE and POST conditions highlight the treatment-induced shifts in parameter means, with dispersion reflecting inter-MPA variability.

2. Combined TFT-MEA/MPA Set-Up

Fig 3.10 provides a schematic overview of the combined platform, highlighting its main components and their functional integration. The system combines:

❖ **Electrical recording module (TFT-MEA):**

- Source and gate lines connected to the Multi Channel Systems USB-ME32-FAI acquisition system and JAPASTIM stimulation unit, respectively.
- Drain-electrodes for extracellular potential recording.
- A PDMS chamber for cell culture and medium containment.

❖ **Contractile recording module (MPA):**

- Array of micropillars designed to transduce the mechanical activity of contracting cardiomyocytes.

❖ **Optical microscope** used to visualize micropillar deflection.

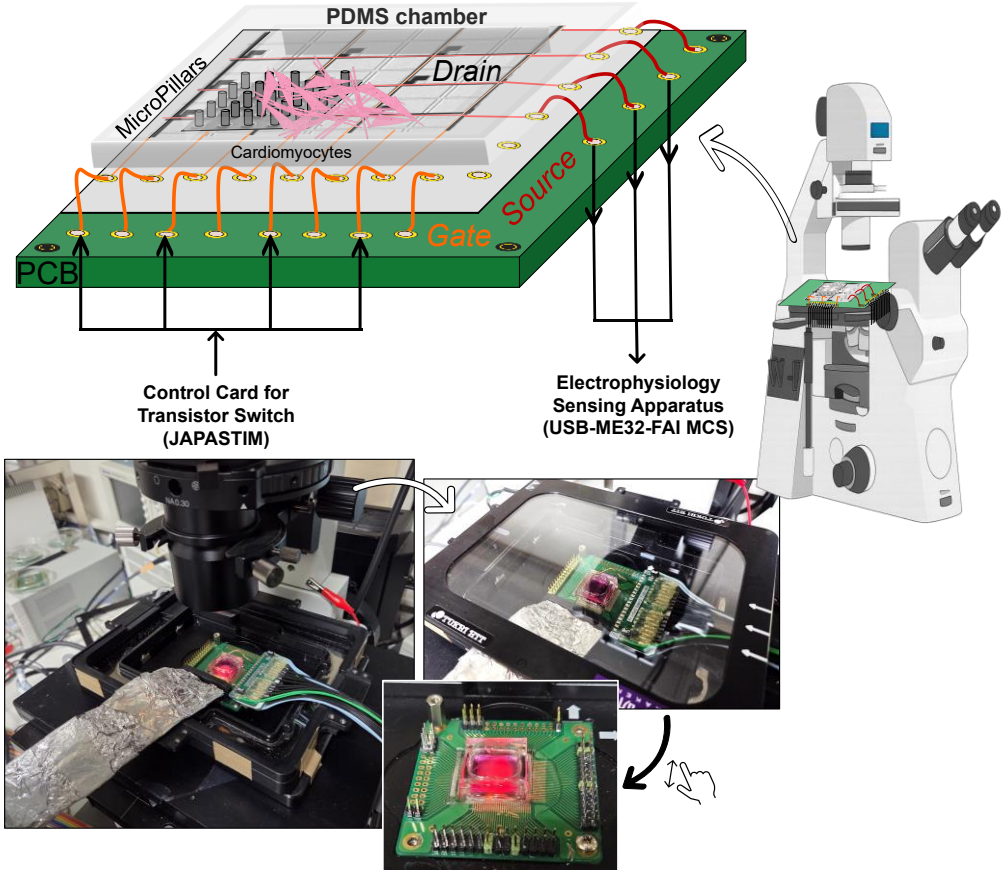


**Fig 3.10 Schematic illustration (top) and photographic images (bottom) of the hybrid TFT MEA/MPA platform for simultaneous electrical and contractile characterization of cardiomyocytes**. The device integrates a TFT-based microelectrode array (TFT-MEA) for electrophysiological recordings with PDMS micropillar arrays (MPA) for contractile force measurements. The TFT-MEA architecture enables independent addressing of each electrode through gate and source lines controlled by the JAPASTIM unit, while extracellular signals are acquired via the USB-ME32-FAI system. Cardiomyocytes are cultured within a PDMS chamber. The images highlight the main components of the setup, including the inverted optical microscope, used for both sample visualization and measurement of micropillar deflection, the electrical connections (gate and source lines), and the mini-incubator used to maintain physiological conditions.

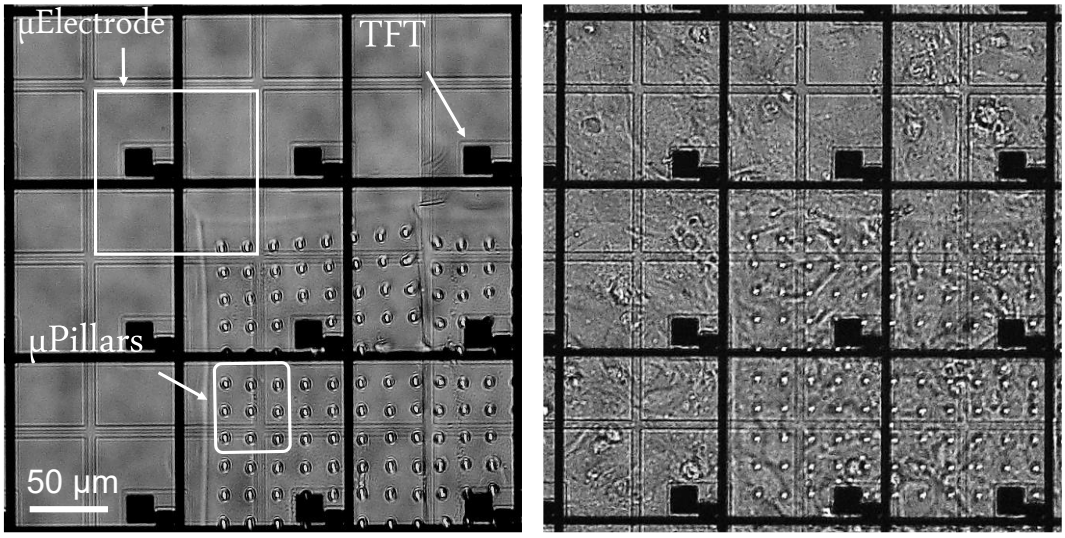


**Fig 3.11 Representative bright-field micrographs of the hybrid TFT-MEA/MPA device, illustrating the key structural components, including the µElectrodes, µPillars, and the underlying thin-film transistors (TFTs).** The same region of the device is shown before and after cell seeding: the left panel correspond to cell-free condition, revealing the device microstructures, whereas the right panel show the same region after cell culture, with cardiomyocytes distributed across both the TFT-MEA and MPA areas. Scale bar: 50 µm.

Isoprenaline Induced Changes in Cardiomyocytes Contractile and Electrical Activity

The performance of the hybrid platform was evaluated using cardiomyocyte cultures (Fig 3.11) at DIV6 and comparing both electrical and contractile activity before and after administration of isoprenaline at 20 nM concentration. A total of 5 electrodes and 60 micropillars from 3 different MPAs were analyzed across the device.

Simultaneous recordings enabled the extraction of both electrophysiological and contractile parameters. In particular, the beating frequency derived from optical (MPA) data showed strong agreement with that obtained from electrical (TFT-MEA) recordings, confirming the platform's capability to capture synchronized electromechanical activity within the same cell population. Beyond frequency analysis, the TFT-MEA also provided complementary parameters such as field potential amplitude, field potential duration, depolarization speed and depolarization duration, allowing an integrated assessment of both electrophysiological and mechanical behavior of the cardiac model.

Following isoprenaline administration, an increase in beating frequency was observed in both electrical and contractile signals, reflected by a decrease in interbeat intervals.

Cardiomyocytes exhibited an increase in contraction force amplitude and velocity, together with a reduction in contraction duration and refractory period. Similarly, electrophysiological analysis revealed an increase in field potential amplitude and depolarization speed, accompanied by a reduction in field potential duration and depolarization duration.

Representative simultaneous electrical and contractile recordings acquired before and after isoprenaline administration are shown in Fig 3.12, highlighting an increase in beating frequency and contractile force amplitude following treatment, while Fig 3.13 shows the quantitative comparison between pre- and post-treatment conditions. Each boxplot represents the distribution of values obtained from individual pillars or electrodes and pooled to describe the overall behavior of the cell population.

Table 3.2 summarizes the corresponding mean ± standard deviation values.

Consistent with the results related to previous measurements obtained using the MPA module alone, isoprenaline administration led to a reduction in variability of contractile frequency-related parameters, particularly interbeat interval and refractory period.

Interestingly, while both electrical and contractile interbeat intervals decreased in mean value following drug administration, an increase in variability was observed in the electrical signal.

Finally, it should be noted that the estimation of the field potential duration (QT) may be affected by analysis-related limitations. In several recordings, the T-wave was not clearly distinguishable, reducing the reliability of automated QT detection. Therefore, these values should be interpreted with caution and considered alongside other electrophysiological parameters.

The ability to simultaneously measure electrical and contractile parameters enables a more comprehensive characterization of cardiomyocyte function compared to single-modality approaches. Overall, these findings prove the hybrid TFT-MEA/MPA platform as a reliable tool for integrated electromechanical analysis of cardiac cell cultures and support its application in pharmacological studies.

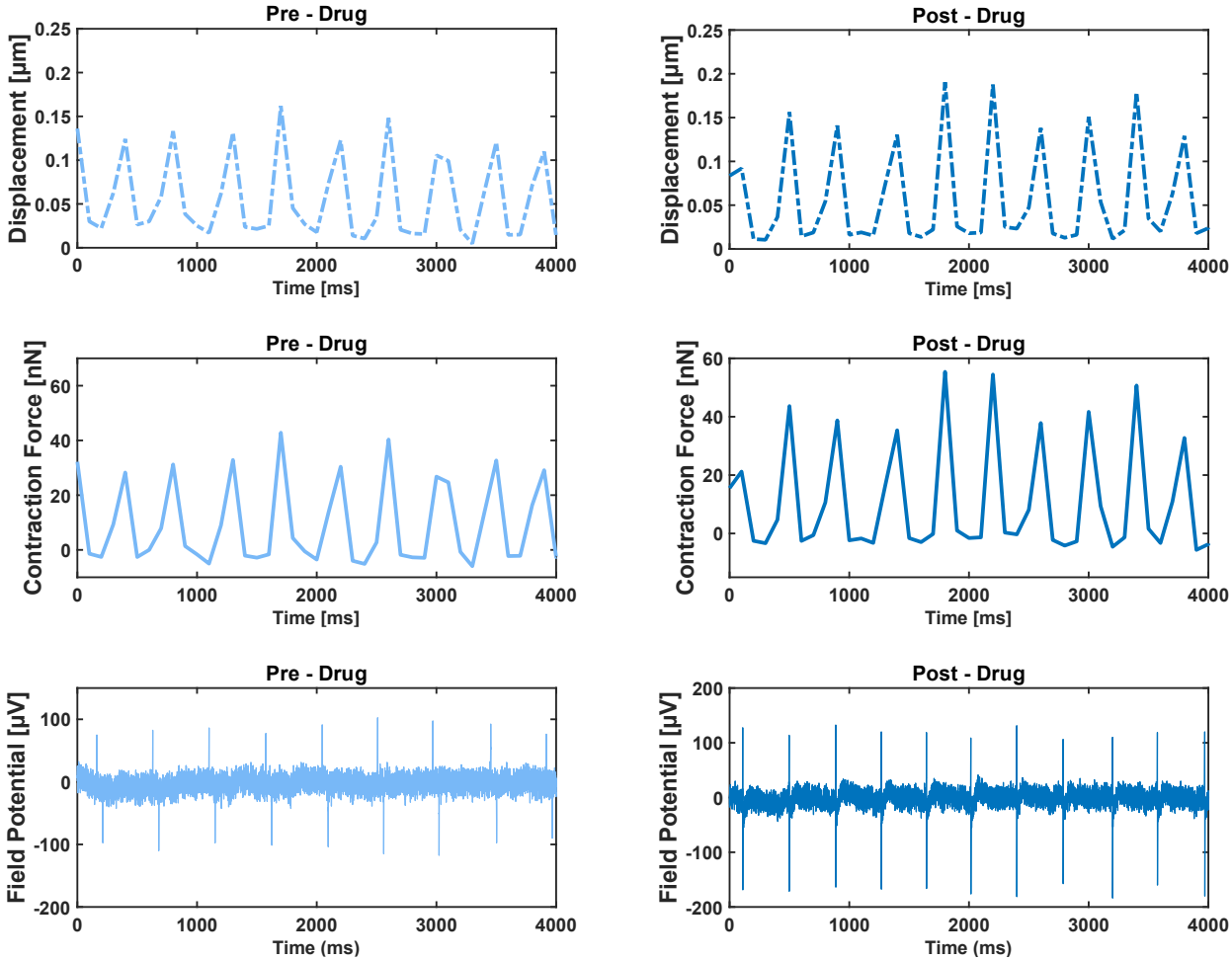


**Fig 3.12 Representative simultaneous electrical and contractile recordings acquired with the hybrid TFT-MEA/MPA platform before (PRE) and after (POST) 20 nM isoprenaline administration**. From top to bottom: micropillar displacement, corresponding contractile force signal, and extracellular field potential. The recordings show a clear increase in beating frequency following drug stimulation, consistently observed in both electrical and contractile signals, accompanied by an increased in contraction force and field potential amplitude. These results demonstrate the capability of the platform to capture synchronized electromechanical activity.

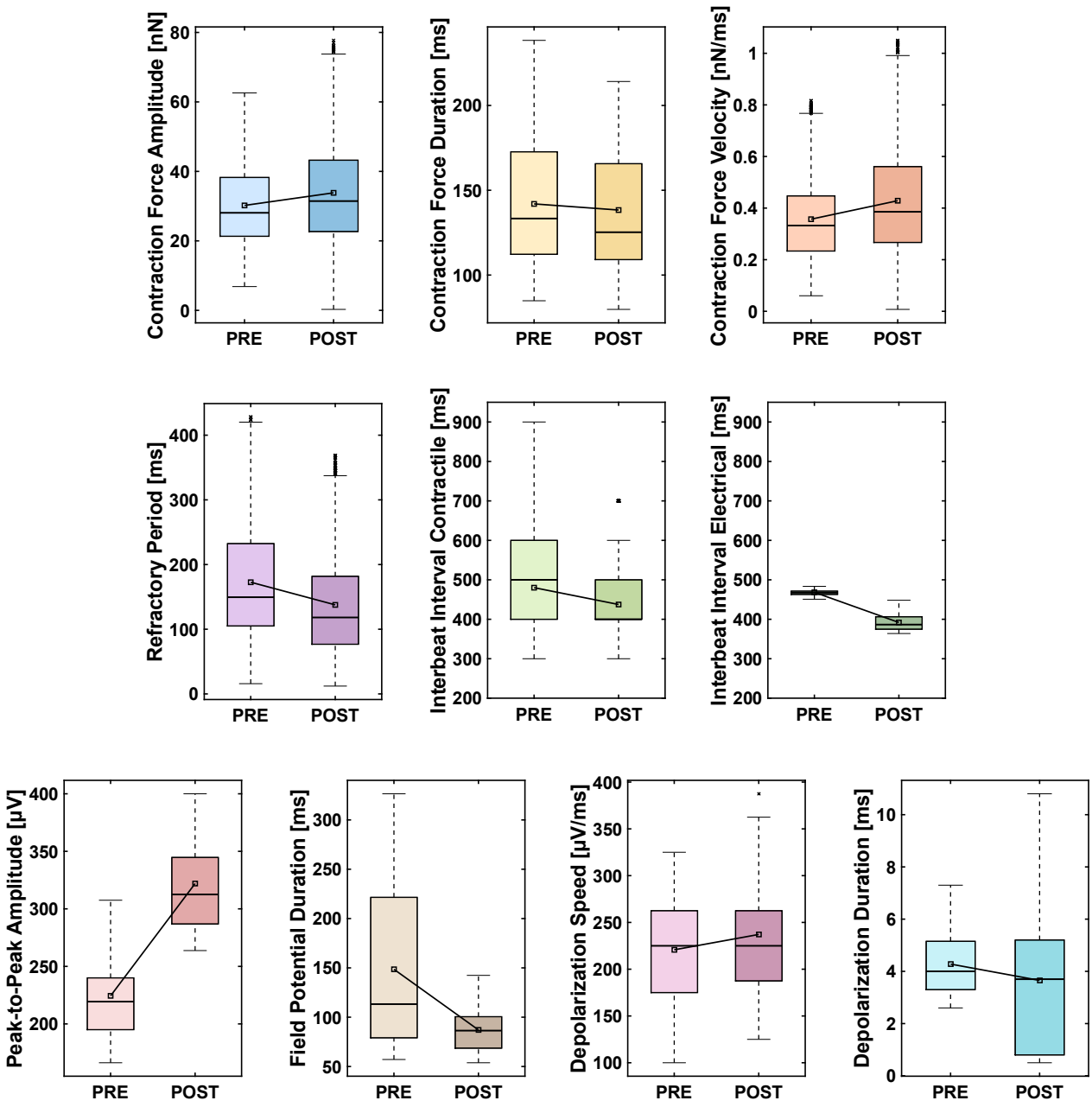


**Fig 3.13 Box plots summarizing the effect of 20 nM isoprenaline on electrophysiological and contractile parameters**. Each boxplot represents the distribution of values extracted from all analyzed micropillars (contractile parameters) and electrodes (electrical parameters), comparing pre-treatment (PRE) and post-treatment (POST) conditions. Square markers indicate mean values, while connecting lines highlight the overall trend between conditions.

| PARAMETER | CONDITION | | | | RELATIVE VARIATION (%) | |
|---|---|---|---|---|---|---|
| | *Pre - Drug* | | *Post - Drug* | | | |
| | Mean | Std | Mean | Std | ΔMean (%) | ΔStd (%) |
| **Contraction Force Amplitude [nN]** | 30.20 | 11.47 | 33.83 | 14.28 | 12.01 | 24.46 |
| **Contraction Force Duration [ms]** | 141.95 | 34.92 | 138.33 | 34.67 | -2.55 | -0.69 |
| **Contraction Force Velocity [nN/ms]** | 0.36 | 0.15 | 0.43 | 0.21 | 20.05 | 30.18 |
| **Refractory Period (tREF) [ms]** | 172.68 | 94.55 | 137.67 | 77.80 | -20.26 | -17.71 |
| **Interbeat Interval_C (IBI_C) [ms]** | 480.14 | 108.84 | 437.47 | 95.72 | -8.87 | -12.06 |
| **Interbeat Interval_E (IBI_E) [ms]** | 468.38 | 7.72 | 391.91 | 22.36 | -16.32 | 189.68 |
| **FP Amplitude Peak-to-Peak (PPA) [μv]** | 224.41 | 37.41 | 322.01 | 41.02 | 43.49 | 9.62 |
| **FP Duration (QT) [ms]** | 148.57 | 88.54 | 87.09 | 21.50 | -41.37 | -75.71 |
| **Depolarization Speed [μV/ms]** | 220.72 | 54.47 | 237.13 | 61.81 | 7.43 | 13.47 |
| **Depolarization Duration [ms]** | 4.28 | 1.32 | 3.65 | 2.56 | -14.63 | 93.97 |

**Table 3.2 Summary of electrophysiological and contractile parameters extracted from the hybrid TFT-MEA/MPA platform before (PRE) and after (POST) 20 nM isoprenaline administration**. Values are reported as mean ± standard deviation, computed by pooling data from all analyzed electrodes (electrical parameters) and micropillars (contractile parameters). Relative variations (%) highlight the drug induced increase in beating frequency and contractile activity, together with consistent changes in electrophysiological parameters. $\Delta\,(\%) = \frac{Value_{POST} - Value_{PRE}}{Value_{PRE}} \times 100.$

## 3.4 Discussion

The hybrid TFT-MEA/MPA platform developed in this study represents a significant step toward the realization of fully integrated, multimodal bioelectronic systems capable of providing simultaneous electrical and mechanical characterization of cardiac tissues *in vitro*. The integration of micro-pillar arrays directly onto an active-matrix thin-film-transistor microelectrode array enables the concurrent and high throughput assessment of electrophysiological and contractile activity from the same cellular population, overcoming the limitations of conventional measurement approaches, where separate devices or experimental sessions are typically required. The successful fabrication of the hybrid device demonstrates the feasibility of combining soft, biocompatible polymeric microstructures with a transparent electronic substrate based on amorphous or polycrystalline semiconductors. The use of two-photon polymerization for direct printing of the PDMS-based micropillar arrays onto the TFT-MEA surface ensured a reliable high spatial resolution and spatial alignment, while maintaining the optical transparency of the underlying substrate—an essential condition for optical imaging.

Functionally, the hybrid platform proved capable of simultaneously acquiring both extracellular field potentials and contractile force signals from neonatal mouse cardiomyocyte cultures, demonstrating the feasibility of a unified platform for simultaneous electromechanical interrogation of cardiac function at the *in vitro* level.

**Experimental Validation**

To validate the performance of the system, both standalone and integrated experimental analyses were conducted.

The variability observed within individual MPAs (*intra-MPA*) can largely be attributed to heterogeneity of cardiomyocyte morphology, alignment, and cell–pillar coupling geometry. Since cells adhere randomly to the PDMS surface and to the micropillars, the efficiency of force transmission may vary depending on the relative positioning of the axis of contraction with respect to the pillar location. This spatial heterogeneity is not expected to affect frequency-related parameters as strongly as amplitude- or velocity-related metrics. Conversely, *inter-MPA* variability—differences among separate arrays within the same culture—may also arise from local variations in cell density, mechanical coupling between neighboring cells, or differences in extracellular matrix deposition. Although two-photon polymerization is a highly accurate fabrication process, minor structural differences among pillars cannot be completely excluded and could contribute to variability in displacement-derived force measurements, affecting both intra- and inter-MPA variability. A mechanical

calibration of individual pillars could confirm the uniformity of their mechanical properties, representing an important step toward fully decoupling biological variability from potential device-related contributions.

Building on this preliminary characterization of the MPA module, pharmacological tests using isoprenaline were also conducted to evaluate the responsiveness and sensitivity of the hybrid TFT-MEA/MPA system.

The device successfully detected the expected chronotropic effect, manifested as a decrease in interbeat interval in both the electrical and mechanical domains. The consistent reduction of the refractory period further confirmed that the system was capable of resolving pharmacologically induced modifications in both excitation and contraction timing.

The system was also able to capture the positive inotropic effect of isoprenaline, evidenced by an increase in contraction force amplitude and contraction velocity. This result highlights the capability of the platform not only to detect changes in beating frequency but also to quantify variations in the strength of cardiomyocyte contraction, providing a more comprehensive assessment of drug-induced functional modulation.

Interestingly, while both electrical and contractile interbeat intervals decreased in mean value following isoprenaline administration, an increase in variability was observed in the electrical recordings. This apparent discrepancy may arise from multiple factors.

From a biological perspective, β-adrenergic stimulation is known to enhance pacemaker activity and increase beating frequency, but it may also introduce a degree of electrophysiological heterogeneity across the cell population, leading to increased variability in the electrical signal.

In addition, the difference between electrical and mechanical variability may reflect the distinct nature of the two measurements. While electrical signals are recorded locally at individual electrodes and are therefore more sensitive to cell-to-cell variability, contractile measurements derived from micropillar deflection represent a more integrated response of multiple cells, resulting in a more regular signal.

Finally, the sequential scanning architecture of the TFT-MEA system may further contribute to the observed variability. Since electrical signals are acquired in a time-multiplexed manner rather than simultaneously across all electrodes, temporal fluctuations in beating activity may be reflected as increased variability in the reconstructed electrical dataset.

Taken together, these results confirm the capability of the platform to reliably capture both electrical and contractile aspects of cardiomyocyte activity. Building on this validation, the functional relevance of the system can be further interpreted.

**Functional relevance of the platform**

The correlation observed between the beating frequencies derived from electrical and optical recordings confirmed that the two readouts originated from the same electromechanical events, validating the temporal synchronization between the two modalities. This result establishes the foundation for a truly integrated analysis of cardiac functionality, in which electrophysiological dynamics and mechanical output can be jointly interpreted to provide a more comprehensive understanding of the tissue's behavior.

This capability represents a key advantage over conventional single-modality systems, enabling a more complete characterization of excitation–contraction coupling at the *in vitro* level.

**Limitations and future perspectives**

Despite these promising results, several limitations of the current implementation should be considered.

First, the number of usable electrodes was notably limited. This was attributable to multiple factors: some electrodes exhibited no detectable activity, likely due to the absence of cells; others were affected by excessive noise; and a subset displayed irregular or unstable activity patterns. As a result, only those electrodes showing consistent and reliable signals across both pre- and post-drug conditions were retained for analysis. Although this selection inevitably reduced the size of the dataset and highlights the need for additional measurements to further confirm the validity of the method, it was appropriate for the specific objectives of this study. In particular, the primary aims were to validate the proper functioning of the MPA and to assess the consistency between the two measurement approaches; given that the TFT-MEA platform had been previously tested and validated, the reduced yet internally consistent dataset was considered sufficient to support these objectives.

Another major limitation of the present hybrid platform lies in the intrinsic asynchrony between the optical and electrical acquisition modalities. Although both signals originate from the same cellular events, the optical and electrical readouts are recorded through two independent acquisition chains operating at different sampling frequencies and without a common temporal reference.

As a result, the correlation between electrophysiological and contractile events can only be established a posteriori, based on frequency alignment rather than frame-by-frame synchronization. This prevents the extraction of truly electro-contractile parameters, which would require sub-millisecond temporal correspondence between the two modalities. In addition, the optical approach used to monitor pillar deflection provides only an indirect

measure of contractile force and is constrained by the limited temporal resolution (10 fps) and susceptibility to noise inherent to live-cell microscopy.

A further limitation of the present study is related to the use of a single TFT-MEA/MPA device for experimental validation. Although the obtained results demonstrate the feasibility and functionality of the platform, the limited number of devices prevents a comprehensive assessment of inter-device reproducibility and fabrication consistency. In particular, it is not possible to fully evaluate potential variability arising from device-to-device differences in micropillar geometry, electrical performance, or integration quality. Consequently, the current dataset should be considered preliminary, and further experiments involving multiple independently fabricated devices will be necessary to statistically validate the robustness and repeatability of the proposed system.

Another limitation arises from the sequential operation of the TFT-MEA system. In the current architecture, the JAPASTIM control card sequentially scans the gate lines, activating each column of transistors for 5 seconds before switching to the next. Consequently, electrical signals from different electrodes are not recorded simultaneously but rather in a temporally multiplexed manner. Although this configuration enables coverage of a large number of recording sites (784 electrodes), it precludes true real-time mapping of electrical propagation across the entire culture. The resulting dataset represents a spatially rich but temporally segmented reconstruction of the electrophysiological activity. Future designs could incorporate parallel addressing schemes or higher-frequency scanning protocols to achieve quasi-simultaneous acquisition across multiple columns, thereby improving temporal resolution.

In future developments, the presented platform could be further improved to enable a fully integrated and synchronous electromechanical characterization of the same cellular population. While the current configuration allows for parallel acquisition of electrical activity from cells in direct contact with the microelectrodes and contractile activity from cells cultured on the PDMS micropillars, these measurements are inherently decoupled.

A key advancement would consist in transforming the passive PDMS micropillars into active sensing elements; each pillar would incorporate a conductive pathway electrically connected to the underlying microelectrodes, extending the sensing interface from the planar substrate to the three-dimensional pillar region. This modification would allow cells adhering to the pillar surface to establish a tighter electrical coupling with the electrode, enabling the acquisition of extracellular signals directly from the same cells whose mechanical activity is being probed.

Concurrently, the integration of an electrical readout mechanism for pillar deflection would eliminate the need for optical tracking. The development of embedded piezoresistive sensing elements within the pillar structure could enable the conversion of pillar bending directly into a measurable electrical signal, simplifying the experimental setup by removing the reliance on microscopy.

The combination of these two strategies would result in a dual-mode sensing unit, where each micropillar simultaneously acts as a local microelectrode and as a mechanical transducer.

Moreover, both electrical and contractile signals could be acquired through the same data acquisition system, ensuring a shared temporal reference and enabling precise correlation between electrophysiological events and contractile responses.

Such a configuration would not only allow perfect synchronization between electrical and contractile activity, but would also transform the platform into a fully integrated electro-contractile biosensor capable of extracting real-time excitation–contraction coupling parameters.

Overall, this study demonstrates the feasibility of integrating electrical and mechanical sensing within a single platform, providing a solid foundation for future developments toward fully synchronized, high-resolution electro-contractile characterization of cardiac tissues for applications in drug screening and disease modeling.

**Long term perspectives**

Beyond the immediate technical improvements discussed above, the hybrid TFT-MEA/MPA platform opens the way toward more advanced bioelectronic systems integrating multiple functionalities and biological models.

In addition to these developments, the hybrid TFT-MEA/MPA approach presents several intrinsic advantages, including:

- optical transparency, enabling direct visualization of the biological interface;
- scalability, due to the large-area addressability of TFT matrices;
- multimodality, through the integration of electrical and mechanical readouts; and
- potential compatibility with flexible or polymeric substrates for future organ-on-chip applications.

In particular, the TFT-MEA device provides a transparent, large-area platform with high electrode density and operates as an active matrix, enabling not only electrophysiological recordings, but also electrical stimulation, impedance measurements, dielectrophoretic manipulation, electrochemical sensing, and optical analyses [206],[207],[208]. Such

versatility allows for the acquisition of extensive and comprehensive datasets from *in vitro* cardiac models.

In this context, a possible future development of this platform could involve the realization of a heterogeneous organ-on-chip system integrating multiple functionally coupled biological networks. In particular, the combination of neuronal and cardiac cell models within the same device could enable the study of neuromuscular interactions in a controlled *in vitro* environment.

By leveraging the addressability and transparency of TFT electronics, such a system could support simultaneous electrical stimulation, mechanical sensing, and optical monitoring across interconnected cellular compartments. The integration of microfluidic architectures would further allow spatial organization of different cell types while maintaining functional coupling, mimicking key aspects of physiological systems such as neuromuscular junctions. Ultimately, this approach could contribute to the development of advanced *in vitro* models for studying complex pathologies, including neurodegenerative diseases such as amyotrophic lateral sclerosis (ALS), and for testing pharmacological interventions in a controlled micro-engineered environment [180].

# Chapter 4 - Conclusions

This PhD thesis addressed a critical need in cardiovascular research: the development of advanced *in vitro* platforms capable of providing a comprehensive and quantitative characterization of cardiac function by simultaneously investigating electrical and contractile activity. Given the impact of cardiovascular diseases and the limitations of current preclinical models, improving the predictive power of *in vitro* systems represents a key step toward safer and more effective therapeutic strategies.

The main objective of this work was to design, optimize, and validate multimodal experimental platforms for the integrated analysis of cardiomyocyte electro-contractile behavior. In this context, two complementary approaches were developed.

In the first part of the thesis, an AFM–MEA platform was implemented and refined to enable synchronized, single-cell-level measurements of electrophysiological activity, contractile force, and mechanical properties. This system demonstrated the capability to capture the complex interplay between electrical excitation and mechanical response with high temporal and spatial resolution. A key strengths of this platform lies in its ability to extract a wide range of functional parameters at the single-cell level, including electrophysiological descriptors (e.g., field potential duration and depolarization dynamics), contractile features (e.g., force amplitude and velocity), and biomechanical properties (such as the temporal evolution of cellular stiffness). Importantly, the integration of these measurements enabled the definition of hybrid biomarkers, such as electro-contractile coupling, providing deeper insight into the physiological state of cardiomyocytes.

The application of the AFM–MEA platform to a pharmacological model of doxorubicin-induced cardiotoxicity further demonstrated its potential. The results revealed significant alterations in both electrical and contractile parameters following drug exposure, confirming the system's sensitivity in detecting early functional impairments. Moreover, the study showed that pre-treatment with extracellular vesicles derived from human amniotic fluid stem cells (hAFSC-EVs) partially mitigate these effects, suggesting a potential cardioprotective role. These findings not only validate the platform as a powerful tool for cardiotoxicity assessment but also underline its relevance for investigating novel therapeutic strategies.

Despite the possibility to quantitatively monitor the behavior of single cells over time, the AFM–MEA approach is inherently limited by low throughput.

To address this constraint, the second part of the thesis focused on the development of a hybrid TFT–MEA/MPA platform designed to enable parallel, high-throughput measurements at the cell population level.

The integration of thin-film transistor-based microelectrode arrays (TFT-MEAs) with micropillar arrays (MPAs) allowed simultaneous recording of electrical activity and contractile behavior in a label-free and scalable manner.

Preliminary validation experiments confirmed the functionality of the integrated system and its responsiveness to pharmacological modulation. In particular, exposure to isoprenaline induced measurable changes in both electrophysiological and contractile parameters, demonstrating the platform's ability to detect drug-induced functional responses. Although still at an early stage of development, this system represents a promising step toward high-throughput multimodal screening platforms.

Taken together, the two experimental approaches presented in this thesis are highly complementary. The AFM–MEA platform enables detailed, high-resolution characterization at the single-cell level, providing mechanistic insights and precise quantification of functional parameters. In contrast, the TFT–MEA/MPA platform offers scalability and throughput, making it suitable for larger-scale pharmacological studies.

From a broader perspective, this work highlights the importance of integrated measurements in cardiac research. The simultaneous evaluation of electrical and mechanical activity provides a more complete and physiologically relevant description of cardiomyocyte function compared to approaches that consider these aspects separately.

Nevertheless, some limitations remain. *In vitro* models, while highly controlled and reproducible, cannot fully recapitulate the complexity of the *in vivo* cardiac environment. Additionally, further optimization and validation of the high-throughput platform are required to fully exploit its potential in large-scale studies.

Future developments may focus on several directions. The integration of these platforms with three-dimensional cardiac models or organ-on-chip systems could enhance physiological relevance. The use of human induced pluripotent stem cell-derived cardiomyocytes (hiPSC-CMs) may enable patient-specific studies and support personalized medicine approaches. Furthermore, coupling experimental platforms with computational modeling and data-driven analysis could improve the identification of predictive biomarkers and accelerate drug development pipelines.

## *References*


[1] A. Shinde *et al.*, “Recent Advances of Biosensor-Integrated Organ-on-a-Chip Technologies for Diagnostics and Therapeutics,” *Anal. Chem.*, vol. 95, no. 6, pp. 3121–3146, Feb. 2023, doi: 10.1021/acs.analchem.2c05036.

[2] L. Tang, J. Yang, Y. Wang, and R. Deng, “Recent Advances in Cardiovascular Disease Biosensors and Monitoring Technologies,” *ACS Sens.*, vol. 8, no. 3, pp. 956–973, Mar. 2023, doi: 10.1021/acssensors.2c02311.

[3] E. H. Ohlstein, “The Grand Challenges in Cardiovascular Drug Discovery and Development,” *Front. Pharmacol.*, vol. 1, 2010, doi: 10.3389/fphar.2010.00125.

[4] “Cardiovascular diseases (CVDs).” [Online]. Available: https://www.who.int/news-room/fact-sheets/detail/cardiovascular-diseases-(cvds)

[5] V. R. Netala, S. K. Teertam, H. Li, and Z. Zhang, “A Comprehensive Review of Cardiovascular Disease Management: Cardiac Biomarkers, Imaging Modalities, Pharmacotherapy, Surgical Interventions, and Herbal Remedies,” *Cells*, vol. 13, no. 17, p. 1471, Sep. 2024, doi: 10.3390/cells13171471.

[6] G. A. Roth *et al.*, “Global Burden of Cardiovascular Diseases and Risk Factors, 1990–2019,” *J. Am. Coll. Cardiol.*, vol. 76, no. 25, pp. 2982–3021, Dec. 2020, doi: 10.1016/j.jacc.2020.11.010.

[7] J. N. M. Lui *et al.*, “Impact of New Cardiovascular Events on Quality of Life and Hospital Costs in People With Cardiovascular Disease in the United Kingdom and United States,” *J. Am. Heart Assoc.*, vol. 12, no. 19, p. e030766, Oct. 2023, doi: 10.1161/JAHA.123.030766.

[8] E. J. Benjamin *et al.*, “Heart Disease and Stroke Statistics—2019 Update: A Report From the American Heart Association,” *Circulation*, vol. 139, no. 10, Mar. 2019, doi: 10.1161/CIR.0000000000000659.

[9] A. Timmis *et al.*, “European Society of Cardiology: cardiovascular disease statistics 2021,” *Eur. Heart J.*, vol. 43, no. 8, pp. 716–799, Feb. 2022, doi: 10.1093/eurheartj/ehab892.

[10] L. A. Kaminsky, C. German, M. Imboden, C. Ozemek, J. E. Peterman, and P. H. Brubaker, “The importance of healthy lifestyle behaviors in the prevention of cardiovascular disease,” *Prog. Cardiovasc. Dis.*, vol. 70, pp. 8–15, Jan. 2022, doi: 10.1016/j.pcad.2021.12.001.

[11] H. C. McGill, C. A. McMahan, and S. S. Gidding, “Preventing Heart Disease in the 21st Century: Implications of the Pathobiological Determinants of Atherosclerosis in Youth (PDAY) Study,” *Circulation*, vol. 117, no. 9, pp. 1216–1227, Mar. 2008, doi: 10.1161/CIRCULATIONAHA.107.717033.

[12] M. C. Bahit, P. Agudo-Quilez, J. Zamorano, and C. M. Gibson, “Cardiovascular adverse effects of common non-oncologic medications: from mechanisms to clinical management,” *Eur. Heart J. - Cardiovasc. Pharmacother.*, vol. 12, no. 2, pp. 118–134, Feb. 2026, doi: 10.1093/ehjcvp/pvag007.

[13] P. Nahla *et al.*, “Pharmacovigilance in Cardiology: A Review of Adverse Drug Reactions in Practice,” *J. Drug Deliv. Ther.*, vol. 15, no. 9, pp. 201–212, Sep. 2025, doi: 10.22270/jddt.v15i9.7366.

[14] X. Li, M. Liu, R. Sun, Y. Zeng, S. Chen, and P. Zhang, “Cardiac complications in cancer treatment – A review,” *Hellenic J. Cardiol.*, vol. 58, no. 3, pp. 190–193, May 2017, doi: 10.1016/j.hjc.2016.12.003.

[15] A. Taleb *et al.*, “Antioxidant effects and mechanism of silymarin in oxidative stress induced cardiovascular diseases,” *Biomed. Pharmacother.*, vol. 102, pp. 689–698, Jun. 2018, doi: 10.1016/j.biopha.2018.03.140.

[16] J. Herrmann, “Adverse cardiac effects of cancer therapies: cardiotoxicity and arrhythmia,” *Nat. Rev. Cardiol.*, vol. 17, no. 8, pp. 474–502, Aug. 2020, doi: 10.1038/s41569-020-0348-1.

[17] W. M. Suchorska, “Radiobiological models in prediction of radiation cardiotoxicity,” *Rep. Pract. Oncol. Radiother.*, vol. 25, no. 1, pp. 46–49, Jan. 2020, doi: 10.1016/j.rpor.2019.12.001.

[18] N. Ferri, P. Siegl, A. Corsini, J. Herrmann, A. Lerman, and R. Benghozi, “Drug attrition during pre-clinical and clinical development: Understanding and managing drug-induced cardiotoxicity,” *Pharmacol. Ther.*, vol. 138, no. 3, pp. 470–484, Jun. 2013, doi: 10.1016/j.pharmthera.2013.03.005.

[19] J. A. DiMasi, H. G. Grabowski, and R. W. Hansen, “Innovation in the pharmaceutical industry: New estimates of R&D costs,” *J. Health Econ.*, vol. 47, pp. 20–33, May 2016, doi: 10.1016/j.jhealeco.2016.01.012.

[20] A. Mathur, Z. Ma, P. Loskill, S. Jeeawoody, and K. E. Healy, “In vitro cardiac tissue models: Current status and future prospects,” *Adv. Drug Deliv. Rev.*, vol. 96, pp. 203–213, Jan. 2016, doi: 10.1016/j.addr.2015.09.011.

[21] D. T. Paik, M. Chandy, and J. C. Wu, “Patient and Disease–Specific Induced Pluripotent Stem Cells for Discovery of Personalized Cardiovascular Drugs and Therapeutics,” *Pharmacol. Rev.*, vol. 72, no. 1, pp. 320–342, Jan. 2020, doi: 10.1124/pr.116.013003.

[22] M. Abdelsayed, E. J. Kort, S. Jovinge, and M. Mercola, “Repurposing drugs to treat cardiovascular disease in the era of precision medicine,” *Nat. Rev. Cardiol.*, vol. 19, no. 11, pp. 751–764, Nov. 2022, doi: 10.1038/s41569-022-00717-6.

[23] N. Milani-Nejad and P. M. L. Janssen, “Small and large animal models in cardiac contraction research: Advantages and disadvantages,” *Pharmacol. Ther.*, vol. 141, no. 3, pp. 235–249, Mar. 2014, doi: 10.1016/j.pharmthera.2013.10.007.

[24] E. C. H. Van Doorn, J. H. Amesz, A. H. Sadeghi, N. M. S. De Groot, O. C. Manintveld, and Y. J. H. J. Taverne, “Preclinical Models of Cardiac Disease: A Comprehensive Overview for Clinical Scientists,” *Cardiovasc. Eng. Technol.*, vol. 15, no. 2, pp. 232–249, Apr. 2024, doi: 10.1007/s13239-023-00707-w.

[25] A. Kumar, “Animal Models in Biomedical Research: Ethics and Alternatives,” *Stallion J. Multidiscip. Assoc. Res. Stud.*, vol. 4, no. 3, pp. 11–17, Jun. 2025, doi: 10.55544/sjmars.4.3.3.

[26] H. Frühwein and N. W. Paul, “‘Lost in translation?’ Animal research in the era of precision medicine,” *J. Transl. Med.*, vol. 23, no. 1, p. 152, Feb. 2025, doi: 10.1186/s12967-025-06084-3.

[27] T. Anzai, T. Yamagata, and H. Uosaki, “Comparative Transcriptome Landscape of Mouse and Human Hearts,” *Front. Cell Dev. Biol.*, vol. 8, p. 268, Apr. 2020, doi: 10.3389/fcell.2020.00268.

[28] W. E. Knight, H. R. Ali, S. J. Nakano, C. E. Wilson, L. A. Walker, and K. C. Woulfe, “Ex vivo Methods for Measuring Cardiac Muscle Mechanical Properties,” *Front. Physiol.*, vol. 11, p. 616996, Jan. 2021, doi: 10.3389/fphys.2020.616996.

[29] X. Zhou, A. Bueno-Orovio, and B. Rodriguez, “In silico evaluation of arrhythmia,” *Curr. Opin. Physiol.*, vol. 1, pp. 95–103, Feb. 2018, doi: 10.1016/j.cophys.2017.11.003.

[30] C. Rodero *et al.*, “A systematic review of cardiac in-silico clinical trials,” *Prog. Biomed. Eng.*, vol. 5, no. 3, p. 032004, Jul. 2023, doi: 10.1088/2516-1091/acdc71.

[31] P. R. R. Van Gorp, S. A. Trines, D. A. Pijnappels, and A. A. F. De Vries, “Multicellular In vitro Models of Cardiac Arrhythmias: Focus on Atrial Fibrillation,” *Front. Cardiovasc. Med.*, vol. 7, p. 43, Mar. 2020, doi: 10.3389/fcvm.2020.00043.

[32] A. K. Jain, D. Singh, K. Dubey, R. Maurya, S. Mittal, and A. K. Pandey, “Models and Methods for In Vitro Toxicity,” in *In Vitro Toxicology*, Elsevier, 2018, pp. 45–65. doi: 10.1016/B978-0-12-804667-8.00003-1.

[33] C. L. Mummery, “Perspectives on the Use of Human Induced Pluripotent Stem Cell-Derived Cardiomyocytes in Biomedical Research,” *Stem Cell Rep.*, vol. 11, no. 6, pp. 1306–1311, Dec. 2018, doi: 10.1016/j.stemcr.2018.11.011.

[34] G. Abdelsayed *et al.*, “2D and 3D in-Vitro models for mimicking cardiac physiology,” *Appl. Eng. Sci.*, vol. 12, p. 100115, Dec. 2022, doi: 10.1016/j.apples.2022.100115.

[35] A. Kennedy, D. D. Finlay, D. Guldenring, R. Bond, K. Moran, and J. McLaughlin, “The Cardiac Conduction System,” *Crit. Care Nurs. Clin. North Am.*, vol. 28, no. 3, pp. 269–279, Sep. 2016, doi: 10.1016/j.cnc.2016.04.001.

[36] M. S. Nielsen, C. J. M. Van Opbergen, T. A. B. Van Veen, and M. Delmar, “The intercalated disc: a unique organelle for electromechanical synchrony in cardiomyocytes,” *Physiol. Rev.*, vol. 103, no. 3, pp. 2271–2319, Jul. 2023, doi: 10.1152/physrev.00021.2022.

[37] S. Kurtenbach, S. Kurtenbach, and G. Zoidl, “Gap junction modulation and its implications for heart function,” *Front. Physiol.*, vol. 5, 2014, doi: 10.3389/fphys.2014.00082.

[38] D. DiFrancesco, “The Role of the Funny Current in Pacemaker Activity,” *Circ. Res.*, vol. 106, no. 3, pp. 434–446, Feb. 2010, doi: 10.1161/CIRCRESAHA.109.208041.

[39] L. F. Santana, E. P. Cheng, and W. J. Lederer, “How does the shape of the cardiac action potential control calcium signaling and contraction in the heart?,” *J. Mol. Cell. Cardiol.*, vol. 49, no. 6, pp. 901–903, Dec. 2010, doi: 10.1016/j.yjmcc.2010.09.005.

[40] M. Grunnet, “Repolarization of the cardiac action potential. Does an increase in repolarization capacity constitute a new anti-arrhythmic principle?,” *Acta Physiol.*, vol. 198, no. s676, pp. 1–48, Feb. 2010, doi: 10.1111/j.1748-1716.2009.02072.x.

[41] M. D. Bootman, D. R. Higazi, S. Coombes, and H. L. Roderick, “Calcium signalling during excitation-contraction coupling in mammalian atrial myocytes,” *J. Cell Sci.*, vol. 119, no. 19, pp. 3915–3925, Oct. 2006, doi: 10.1242/jcs.03223.

[42] C. J. Fearnley, H. L. Roderick, and M. D. Bootman, “Calcium Signaling in Cardiac Myocytes,” *Cold Spring Harb. Perspect. Biol.*, vol. 3, no. 11, pp. a004242–a004242, Nov. 2011, doi: 10.1101/cshperspect.a004242.

[43] J. A. Keefe, O. M. Moore, K. S. Ho, and X. H. T. Wehrens, “Role of Ca2+ in healthy and pathologic cardiac function: from normal excitation–contraction coupling to mutations that cause inherited arrhythmia,” *Arch. Toxicol.*, vol. 97, no. 1, pp. 73–92, Jan. 2023, doi: 10.1007/s00204-022-03385-0.

[44] R. B. Clark, M. E. Mangoni, A. Lueger, B. Couette, J. Nargeot, and W. R. Giles, “A rapidly activating delayed rectifier $K^+$ current regulates pacemaker activity in adult mouse sinoatrial node cells,” *Am. J. Physiol.-Heart Circ. Physiol.*, vol. 286, no. 5, pp. H1757–H1766, May 2004, doi: 10.1152/ajpheart.00753.2003.

[45] Y. Kubo *et al.*, “International Union of Pharmacology. LIV. Nomenclature and Molecular Relationships of Inwardly Rectifying Potassium Channels,” *Pharmacol. Rev.*, vol. 57, no. 4, pp. 509–526, Dec. 2005, doi: 10.1124/pr.57.4.11.

[46] D. M. Bers, “Cardiac excitation–contraction coupling,” *Nature*, vol. 415, no. 6868, pp. 198–205, Jan. 2002, doi: 10.1038/415198a.

[47] C. Tasche, E. Meyhöfer, and B. Brenner, “A force transducer for measuring mechanical properties of single cardiac myocytes,” *Am. J. Physiol.-Heart Circ. Physiol.*, vol. 277, no. 6, pp. H2400–H2408, Dec. 1999, doi: 10.1152/ajpheart.1999.277.6.H2400.

[48] Gisela Lin, R. E. Palmer, K. S. J. Pister, and K. P. Roos, “Miniature heart cell force transducer system implemented in MEMS technology,” *IEEE Trans. Biomed. Eng.*, vol. 48, no. 9, pp. 996–1006, Sep. 2001, doi: 10.1109/10.942589.

[49] J. Domke, W. J. Parak, M. George, H. E. Gaub, and M. Radmacher, “Mapping the mechanical pulse of single cardiomyocytes with the atomic force microscope,” *Eur. Biophys. J.*, vol. 28, no. 3, pp. 179–186, Mar. 1999, doi: 10.1007/s002490050198.

[50] S. Vahabi, N. Salman, and B. N. Salman, “Atomic Force Microscopy Application in Biological Research: A Review Study,” vol. 38, no. 2.

[51] J. Liu, N. Sun, M. A. Bruce, J. C. Wu, and M. J. Butte, “Atomic Force Mechanobiology of Pluripotent Stem Cell-Derived Cardiomyocytes,” *PLoS ONE*, vol. 7, no. 5, p. e37559, May 2012, doi: 10.1371/journal.pone.0037559.

[52] N.-E. Oyunbaatar, D.-H. Lee, S. Patil, E.-S. Kim, and D.-W. Lee, “Biomechanical Characterization of Cardiomyocyte Using PDMS Pillar with Microgrooves,” *Sensors*, vol. 16, no. 8, p. 1258, Aug. 2016, doi: 10.3390/s16081258.

[53] K. M. Beussman, M. L. Rodriguez, A. Leonard, N. Taparia, C. R. Thompson, and N. J. Sniadecki, “Micropost arrays for measuring stem cell-derived cardiomyocyte contractility,” *Methods*, vol. 94, pp. 43–50, Feb. 2016, doi: 10.1016/j.ymeth.2015.09.005.

[54] A. J. S. Ribeiro *et al.*, “Multi-Imaging Method to Assay the Contractile Mechanical Output of Micropatterned Human iPSC-Derived Cardiac Myocytes,” *Circ. Res.*, vol. 120, no. 10, pp. 1572–1583, May 2017, doi: 10.1161/CIRCRESAHA.116.310363.

[55] L. Sala *et al.*, “MUSCLEMOTION: A Versatile Open Software Tool to Quantify Cardiomyocyte and Cardiac Muscle Contraction In Vitro and In Vivo,” *Circ. Res.*, vol. 122, no. 3, Feb. 2018, doi: 10.1161/CIRCRESAHA.117.312067.

[56] B. W. Steadman, K. B. Moore, K. W. Spitzer, and J. H. B. Bridge, “A video system for measuring motion in contracting heart cells,” *IEEE Trans. Biomed. Eng.*, vol. 35, no. 4, pp. 264–272, Apr. 1988, doi: 10.1109/10.1375.

[57] M. L. McCain, H. Yuan, F. S. Pasqualini, P. H. Campbell, and K. K. Parker, “Matrix elasticity regulates the optimal cardiac myocyte shape for contractility,” *Am. J. Physiol.-Heart Circ. Physiol.*, vol. 306, no. 11, pp. H1525–H1539, Jun. 2014, doi: 10.1152/ajpheart.00799.2013.

[58] J. H.-C. Wang and J.-S. Lin, “Cell traction force and measurement methods,” *Biomech. Model. Mechanobiol.*, vol. 6, no. 6, pp. 361–371, Oct. 2007, doi: 10.1007/s10237-006-0068-4.

[59] F. S. Pasqualini, A. Agarwal, B. B. O’Connor, Q. Liu, S. P. Sheehy, and K. K. Parker, “Traction force microscopy of engineered cardiac tissues,” *PLOS ONE*, vol. 13, no. 3, p. e0194706, Mar. 2018, doi: 10.1371/journal.pone.0194706.

[60] M. Goßmann *et al.*, “Mechano-Pharmacological Characterization of Cardiomyocytes Derived from Human Induced Pluripotent Stem Cells,” *Cell. Physiol. Biochem.*, vol. 38, no. 3, pp. 1182–1198, 2016, doi: 10.1159/000443124.

[61] L. Wang *et al.*, “Microdevice Platform for Continuous Measurement of Contractility, Beating Rate, and Beating Rhythm of Human-Induced Pluripotent Stem Cell-Cardiomyocytes inside a Controlled Incubator Environment,” *ACS Appl. Mater. Interfaces*, vol. 10, no. 25, pp. 21173–21183, Jun. 2018, doi: 10.1021/acsami.8b05407.

[62] D.-S. Kim, Y.-J. Jeong, B.-K. Lee, A. Shanmugasundaram, and D.-W. Lee, “Piezoresistive sensor-integrated PDMS cantilever: A new class of device for measuring the drug-induced changes in the mechanical activity of cardiomyocytes,” *Sens. Actuators B Chem.*, vol. 240, pp. 566–572, Mar. 2017, doi: 10.1016/j.snb.2016.08.167.

[63] J. U. Lind *et al.*, “Cardiac microphysiological devices with flexible thin-film sensors for higher-throughput drug screening,” *Lab Chip*, vol. 17, no. 21, pp. 3692–3703, 2017, doi: 10.1039/C7LC00740J.

[64] H. Li *et al.*, “Detection of cardiovascular drugs and marine toxins using a multifunctional cell-based impedance biosensor system,” *Anal. Methods*, vol. 7, no. 18, pp. 7715–7723, 2015, doi: 10.1039/C5AY00910C.

[65] N. Hu *et al.*, “High-performance beating pattern function of human induced pluripotent stem cell-derived cardiomyocyte-based biosensors for hERG inhibition recognition,” *Biosens. Bioelectron.*, vol. 67, pp. 146–153, May 2015, doi: 10.1016/j.bios.2014.07.080.

[66] B. G. Kornreich, “The patch clamp technique: Principles and technical considerations,” *J. Vet. Cardiol.*, vol. 9, no. 1, pp. 25–37, May 2007, doi: 10.1016/j.jvc.2007.02.001.

[67] D. C. Bell and B. Fermini, “Use of automated patch clamp in cardiac safety assessment: past, present and future perspectives,” *J. Pharmacol. Toxicol. Methods*, vol. 110, p. 107072, Jul. 2021, doi: 10.1016/j.vascn.2021.107072.

[68] M. Reppel *et al.*, “Microelectrode arrays: A new tool to measure embryonic heart activity,” *J. Electrocardiol.*, vol. 37, pp. 104–109, Oct. 2004, doi: 10.1016/j.jelectrocard.2004.08.033.

[69] M. E. Spira and A. Hai, “Multi-electrode array technologies for neuroscience and cardiology,” *Nat. Nanotechnol.*, vol. 8, no. 2, pp. 83–94, Feb. 2013, doi: 10.1038/nnano.2012.265.

[70] M. C. Müllenbroich *et al.*, “Novel Optics-Based Approaches for Cardiac Electrophysiology: A Review,” *Front. Physiol.*, vol. 12, p. 769586, Nov. 2021, doi: 10.3389/fphys.2021.769586.

[71] J. R. Berlin and M. Konishi, “Ca2+ transients in cardiac myocytes measured with high and low affinity Ca2+ indicators,” *Biophys. J.*, vol. 65, no. 4, pp. 1632–1647, Oct. 1993, doi: 10.1016/S0006-3495(93)81211-6.

[72] A. Allan *et al.*, “High-throughput longitudinal electrophysiology screening of mature chamber-specific hiPSC-CMs using optical mapping,” *iScience*, vol. 26, no. 7, p. 107142, Jul. 2023, doi: 10.1016/j.isci.2023.107142.

[73] R. Shinnawi *et al.*, “Monitoring Human-Induced Pluripotent Stem Cell-Derived Cardiomyocytes with Genetically Encoded Calcium and Voltage Fluorescent Reporters,” *Stem Cell Rep.*, vol. 5, no. 4, pp. 582–596, Oct. 2015, doi: 10.1016/j.stemcr.2015.08.009.

[74] S. D. Girouard, K. R. Laurita. Ph.D., and D. S. Rosenbaum, “Unique Properties of Cardiac Action Potentials Recorded with Voltage-Sensitive Dyes,” *J. Cardiovasc. Electrophysiol.*, vol. 7, no. 11, pp. 1024–1038, Nov. 1996, doi: 10.1111/j.1540-8167.1996.tb00478.x.

[75] N.-E. Oyunbaatar, Y. Dai, A. Shanmugasundaram, B.-K. Lee, E.-S. Kim, and D.-W. Lee, “Development of a Next-Generation Biosensing Platform for Simultaneous Detection of Mechano- and Electrophysiology of the Drug-Induced Cardiomyocytes,” *ACS Sens.*, vol. 4, no. 10, pp. 2623–2630, Oct. 2019, doi: 10.1021/acssensors.9b00852.

[76] N. T. Feric *et al.*, “Engineered Cardiac Tissues Generated in the Biowire II: A Platform for Human-Based Drug Discovery,” *Toxicol. Sci.*, vol. 172, no. 1, pp. 89–97, Nov. 2019, doi: 10.1093/toxsci/kfz168.

[77] H. Liu *et al.*, “Heart-on-a-Chip Model with Integrated Extra- and Intracellular Bioelectronics for Monitoring Cardiac Electrophysiology under Acute Hypoxia,” *Nano Lett.*, vol. 20, no. 4, pp. 2585–2593, Apr. 2020, doi: 10.1021/acs.nanolett.0c00076.

[78] M. Dipalo *et al.*, “Intracellular and Extracellular Recording of Spontaneous Action Potentials in Mammalian Neurons and Cardiac Cells with 3D Plasmonic Nanoelectrodes,” *Nano Lett.*, vol. 17, no. 6, pp. 3932–3939, Jun. 2017, doi: 10.1021/acs.nanolett.7b01523.

[79] S. K. Rastogi, J. Bliley, D. J. Shiwarski, G. Raghavan, A. W. Feinberg, and T. Cohen-Karni, “Graphene Microelectrode Arrays for Electrical and Optical Measurements of Human Stem Cell-Derived Cardiomyocytes,” *Cell. Mol. Bioeng.*, vol. 11, no. 5, pp. 407–418, Oct. 2018, doi: 10.1007/s12195-018-0525-z.

[80] D. Xu *et al.*, “Synchronized intracellular and extracellular recording of action potentials by three-dimensional nanoroded electroporation,” *Biosens. Bioelectron.*, vol. 192, p. 113501, Nov. 2021, doi: 10.1016/j.bios.2021.113501.

[81] F. Qian *et al.*, “Simultaneous electrical recording of cardiac electrophysiology and contraction on chip,” *Lab. Chip*, vol. 17, no. 10, pp. 1732–1739, 2017, doi: 10.1039/C7LC00210F.

[82] B. X. E. Desbiolles *et al.*, “Volcano-Shaped Scanning Probe Microscopy Probe for Combined Force-Electrogram Recordings from Excitable Cells,” *Nano Lett.*, vol. 20, no. 6, pp. 4520–4529, Jun. 2020, doi: 10.1021/acs.nanolett.0c01319.

[83] D. Zhang, Y. Xiang, Q. Zou, K. Zhu, and N. Hu, “Electromechanical integrated recording of single cardiomyocyte in situ by multimodal microelectrode biosensing system,” *Biosens. Bioelectron.*, vol. 212, p. 114387, Sep. 2022, doi: 10.1016/j.bios.2022.114387.

[84] J. Fang *et al.*, “Cardiomyocyte electrical-mechanical synchronized model for high-content, dose-quantitative and time-dependent drug assessment,” *Microsyst. Nanoeng.*, vol. 7, no. 1, p. 26, Mar. 2021, doi: 10.1038/s41378-021-00247-0.

[85] M. C. Ribeiro *et al.*, “Functional maturation of human pluripotent stem cell derived cardiomyocytes in vitro – Correlation between contraction force and electrophysiology,” *Biomaterials*, vol. 51, pp. 138–150, May 2015, doi: 10.1016/j.biomaterials.2015.01.067.

[86] G. Caluori *et al.*, “Non-invasive electromechanical cell-based biosensors for improved investigation of 3D cardiac models,” *Biosens. Bioelectron.*, vol. 124–125, pp. 129–135, Jan. 2019, doi: 10.1016/j.bios.2018.10.021.

[87] T. Ohya *et al.*, “Simultaneous measurement of contractile force and field potential of dynamically beating human iPS cell-derived cardiac cell sheet-tissue with flexible electronics,” *Lab. Chip*, vol. 21, no. 20, pp. 3899–3909, 2021, doi: 10.1039/D1LC00411E.

[88] P. P. Kanade, N.-E. Oyunbaatar, Y.-J. Jeong, and D.-W. Lee, “Mea-On-Cantilever – A Novel Multifunctional Device for Drug Toxicity Screening in Cardiomyocytes,” in *2021 IEEE 34th International Conference on Micro Electro Mechanical Systems (MEMS)*, Gainesville, FL, USA: IEEE, Jan. 2021, pp. 506–508. doi: 10.1109/MEMS51782.2021.9375167.

[89] Z. Zhao *et al.*, “Simultaneous measurement of contraction forces and field potentials of cardiomyocytes subjected to ion channel inhibitors,” *Sens. Actuators B Chem.*, vol. 358, p. 131495, May 2022, doi: 10.1016/j.snb.2022.131495.

[90] Q. Wu *et al.*, “Flexible 3D printed microwires and 3D microelectrodes for heart-on-a-chip engineering,” *Biofabrication*, vol. 15, no. 3, p. 035023, Jul. 2023, doi: 10.1088/1758-5090/acd8f4.

[91] P. P. Kanade, N. Oyunbaatar, J. Kim, B. Lee, E. Kim, and D. Lee, “Cardiotoxicity Assessment through a Polymer-Based Cantilever Platform: An Integrated Electro-Mechanical Screening Approach,” *Small*, vol. 20, no. 33, p. 2311274, Aug. 2024, doi: 10.1002/smll.202311274.

[92] J. F. Saenz Cogollo, M. Tedesco, S. Martinoia, and R. Raiteri, “A new integrated system combining atomic force microscopy and micro-electrode array for measuring the mechanical properties of living cardiac myocytes,” *Biomed. Microdevices*, vol. 13, no. 4, pp. 613–621, Aug. 2011, doi: 10.1007/s10544-011-9531-9.

[93] J. F. Saenz Cogollo, M. Tedesco, S. Martinoia, and R. Raiteri, “A Novel AFM-MEA Platform for Studying the Real Time Mechano-Electrical Behavior of Cardiac Myocytes,” *MRS Proc.*, vol. 1261, pp. 1261-U04-09, 2010, doi: 10.1557/PROC-1261-U04-09.

[94] G. Caluori, R. Raiteri, and M. Tedesco, “Simultaneous AFM Investigation of the Single Cardiomyocyte Electro-Chemo-Mechanics During Excitation-Contraction Coupling,” in *Atomic Force Microscopy*, vol. 1886, N. C. Santos and F. A. Carvalho, Eds., in Methods in Molecular Biology, vol. 1886. , New York, NY: Springer New York, 2019, pp. 355–367. doi: 10.1007/978-1-4939-8894-5_21.

[95] C. Thomasjr, P. Springer, G. Loeb, Y. Berwaldnetter, and L. Okun, “A miniature microelectrode array to monitor the bioelectric activity of cultured cells,” *Exp. Cell Res.*, vol. 74, no. 1, pp. 61–66, Sep. 1972, doi: 10.1016/0014-4827(72)90481-8.

[96] A. Stett *et al.*, “Biological application of microelectrode arrays in drug discovery and basic research,” *Anal. Bioanal. Chem.*, vol. 377, no. 3, pp. 486–495, Oct. 2003, doi: 10.1007/s00216-003-2149-x.

[97] M. Reppel *et al.*, “The electrocardiogram of human embryonic stem cell–derived cardiomyocytes,” *J. Electrocardiol.*, vol. 38, no. 4, pp. 166–170, Oct. 2005, doi: 10.1016/j.jelectrocard.2005.06.029.

[98] Y. Omura, “RELATIONSHIP BETWEEN TRANSMEMBRANE ACTION POTENTIALS OF SINGLE CARDIAC CELLS AND THEIR CORRESPONDING SURFACE ELECTROGRAMS *IN VIVO* AND *IN VITRO* , AND RELATED ELECTROMECHANICAL PHENOMENA*,†,” *Trans. N. Y. Acad. Sci.*, vol. 32, no. 8 Series II, pp. 874–910, Dec. 1970, doi: 10.1111/j.2164-0947.1970.tb02987.x.

[99] M. Halbach, U. Egert, J. Hescheler, and K. Banach, “Estimation of Action Potential Changes from Field Potential Recordings in Multicellular Mouse Cardiac Myocyte Cultures,” *Cell. Physiol. Biochem.*, vol. 13, no. 5, pp. 271–284, 2003, doi: 10.1159/000074542.

[100] D. A. Israel, W. H. Barry, D. J. Edell, and R. G. Mark, “An array of microelectrodes to stimulate and record from cardiac cells in culture,” *Am. J. Physiol.-Heart Circ. Physiol.*, vol. 247, no. 4, pp. H669–H674, Oct. 1984, doi: 10.1152/ajpheart.1984.247.4.H669.

[101] K. Kujala *et al.*, “Electrical Field Stimulation with a Novel Platform: Effect on Cardiomyocyte Gene Expression but not on Orientation,” *Int. J. Biomed. Sci. IJBS*, vol. 8, no. 2, pp. 109–120, Jun. 2012.

[102] F. Heer *et al.*, “CMOS microelectrode array for the monitoring of electrogenic cells,” *Biosens. Bioelectron.*, vol. 20, no. 2, pp. 358–366, Sep. 2004, doi: 10.1016/j.bios.2004.02.006.

[103] B. D. DeBusschere and G. T. A. Kovacs, “Portable cell-based biosensor system using integrated CMOS cell-cartridges,” *Biosens. Bioelectron.*, vol. 16, no. 7–8, pp. 543–556, Sep. 2001, doi: 10.1016/S0956-5663(01)00168-3.

[104] J. S. Choi, H. J. Lee, S. Rajaraman, and D.-H. Kim, “Recent advances in three-dimensional microelectrode array technologies for in vitro and in vivo cardiac and neuronal interfaces,” *Biosens. Bioelectron.*, vol. 171, p. 112687, Jan. 2021, doi: 10.1016/j.bios.2020.112687.

[105] A. Tanwar, H. A. Gandhi, D. Kushwaha, and J. Bhattacharya, “A review on microelectrode array fabrication techniques and their applications,” *Mater. Today Chem.*, vol. 26, p. 101153, Dec. 2022, doi: 10.1016/j.mtchem.2022.101153.

[106] B. J. Kim and E. Meng, “Review of polymer MEMS micromachining,” *J. Micromechanics Microengineering*, vol. 26, no. 1, p. 013001, Jan. 2016, doi: 10.1088/0960-1317/26/1/013001.

[107] A. Blau *et al.*, “Flexible, all-polymer microelectrode arrays for the capture of cardiac and neuronal signals,” *Biomaterials*, vol. 32, no. 7, pp. 1778–1786, Mar. 2011, doi: 10.1016/j.biomaterials.2010.11.014.

[108] N. Adly *et al.*, “Printed microelectrode arrays on soft materials: from PDMS to hydrogels,” *Npj Flex. Electron.*, vol. 2, no. 1, p. 15, May 2018, doi: 10.1038/s41528-018-0027-z.

[109] A. Tooker, E. Meng, J. Erickson, Yu-Chong Tai, and J. Pine, “Biocomplatible parylene neurocages,” *IEEE Eng. Med. Biol. Mag.*, vol. 24, no. 6, pp. 30–33, Nov. 2005, doi: 10.1109/MEMB.2005.1549727.

[110] F. Santoro, J. Schnitker, G. Panaitov, and A. Offenhäusser, “On Chip Guidance and Recording of Cardiomyocytes with 3D Mushroom-Shaped Electrodes,” *Nano Lett.*, vol. 13, no. 11, pp. 5379–5384, Nov. 2013, doi: 10.1021/nl402901y.

[111] A. Fendyur and M. E. Spira, “Toward on-chip, in-cell recordings from cultured cardiomyocytes by arrays of gold mushroom-shaped microelectrodes,” *Front. Neuroengineering*, vol. 5, 2012, doi: 10.3389/fneng.2012.00021.

[112] D. Xu *et al.*, “Synchronized intracellular and extracellular recording of action potentials by three-dimensional nanoroded electroporation,” *Biosens. Bioelectron.*, vol. 192, p. 113501, Nov. 2021, doi: 10.1016/j.bios.2021.113501.

[113] Z. Jahed *et al.*, “Nanocrown electrodes for parallel and robust intracellular recording of cardiomyocytes,” *Nat. Commun.*, vol. 13, no. 1, p. 2253, Apr. 2022, doi: 10.1038/s41467-022-29726-2.

[114] S. Rajaraman *et al.*, “Microfabrication technologies for a coupled three-dimensional microelectrode, microfluidic array,” *J. Micromechanics Microengineering*, vol. 17, no. 1, pp. 163–171, Jan. 2007, doi: 10.1088/0960-1317/17/1/021.

[115] H. Liu *et al.*, “Heart-on-a-Chip Model with Integrated Extra- and Intracellular Bioelectronics for Monitoring Cardiac Electrophysiology under Acute Hypoxia,” *Nano Lett.*, vol. 20, no. 4, pp. 2585–2593, Apr. 2020, doi: 10.1021/acs.nanolett.0c00076.

[116] C. M. Didier, A. Kundu, D. DeRoo, and S. Rajaraman, “Development of *in vitro* 2D and 3D microelectrode arrays and their role in advancing biomedical research,” *J. Micromechanics Microengineering*, vol. 30, no. 10, p. 103001, Oct. 2020, doi: 10.1088/1361-6439/ab8e91.

[117] G. Binnig, C. F. Quate, and Ch. Gerber, “Atomic Force Microscope,” *Phys. Rev. Lett.*, vol. 56, no. 9, pp. 930–933, Mar. 1986, doi: 10.1103/PhysRevLett.56.930.

[118] Gerd K. Bennig, “Atomic force microscope and method for imaging surfaces with atomic resolution,” US4724318A [Online]. Available: https://patents.google.com/patent/US4724318

[119] R. Goyal, V. Sikka, S. Maity, and S. Chakraborty, “A review on Atomic Force Microscopy: instrumentation, procedure, and applications in textiles”.

[120] Y. F. Dufrêne *et al.*, “Imaging modes of atomic force microscopy for application in molecular and cell biology,” *Nat. Nanotechnol.*, vol. 12, no. 4, pp. 295–307, Apr. 2017, doi: 10.1038/nnano.2017.45.

[121] N. Gavara, “A beginner’s guide to atomic force microscopy probing for cell mechanics,” *Microsc. Res. Tech.*, vol. 80, no. 1, pp. 75–84, Jan. 2017, doi: 10.1002/jemt.22776.

[122] M. Krieg *et al.*, “Atomic force microscopy-based mechanobiology,” *Nat. Rev. Phys.*, vol. 1, no. 1, pp. 41–57, Nov. 2018, doi: 10.1038/s42254-018-0001-7.

[123] C. Shi, Y. He, M. Ding, Y. Wang, and J. Zhong, “Nanoimaging of food proteins by atomic force microscopy. Part I: Components, imaging modes, observation ways, and research types,” *Trends Food Sci. Technol.*, vol. 87, pp. 3–13, May 2019, doi: 10.1016/j.tifs.2018.11.028.

[124] Z. Matias, C. S. Lopes, N. C. Santos, and F. A. Carvalho, “Nanotechnology meets medicine: applications of atomic force microscopy in disease,” *Biophys. Rev.*, vol. 17, no. 2, pp. 359–384, Apr. 2025, doi: 10.1007/s12551-025-01306-w.

[125] N. Jalili and K. Laxminarayana, “A review of atomic force microscopy imaging systems: application to molecular metrology and biological sciences,” *Mechatronics*, vol. 14, no. 8, pp. 907–945, Oct. 2004, doi: 10.1016/j.mechatronics.2004.04.005.

[126] S. Liu and Y. Wang, “Application of AFM in microbiology: a review,” *Scanning*, vol. 32, no. 2, pp. 61–73, Mar. 2010, doi: 10.1002/sca.20173.

[127] S. Maghsoudy-Louyeh, M. Kropf, and B. R. Tittmann, “Review of Progress in Atomic Force Microscopy,” *Open Neuroimaging J.*, vol. 12, no. 1, pp. 86–104, Dec. 2018, doi: 10.2174/1874440001812010086.

[128] L. Wang, T. Chen, X. Zhou, Q. Huang, and C. Jin, “Atomic force microscopy observation of lipopolysaccharide-induced cardiomyocyte cytoskeleton reorganization,” *Micron*, vol. 51, pp. 48–53, Aug. 2013, doi: 10.1016/j.micron.2013.06.008.

[129] D. Borin, I. Pecorari, B. Pena, and O. Sbaizero, “Novel insights into cardiomyocytes provided by atomic force microscopy,” *Semin. Cell Dev. Biol.*, vol. 73, pp. 4–12, Jan. 2018, doi: 10.1016/j.semcdb.2017.07.003.

[130] D. Kabanov, S. Klimovic, V. Rotrekl, M. Pesl, and J. Pribyl, “Atomic force spectroscopy is a promising tool to study contractile properties of cardiac cells,” *Micron*, vol. 155, p. 103199, Apr. 2022, doi: 10.1016/j.micron.2021.103199.

[131] Y. F. Dufrêne *et al.*, “Imaging modes of atomic force microscopy for application in molecular and cell biology,” *Nat. Nanotechnol.*, vol. 12, no. 4, pp. 295–307, Apr. 2017, doi: 10.1038/nnano.2017.45.

[132] M. Pesl *et al.*, “Atomic force microscopy combined with human pluripotent stem cell derived cardiomyocytes for biomechanical sensing,” *Biosens. Bioelectron.*, vol. 85, pp. 751–757, Nov. 2016, doi: 10.1016/j.bios.2016.05.073.

[133] B. V. Derjaguin, V. M. Muller, and Yu. P. Toporov, “Effect of contact deformations on the adhesion of particles,” *J. Colloid Interface Sci.*, vol. 53, no. 2, pp. 314–326, Nov. 1975, doi: 10.1016/0021-9797(75)90018-1.

[134] H. Hertz, *Miscellaneous papers*. London: Macmillan, New York, Macmillan and co., 1896. [Online]. Available: http://archive.org/details/cu31924012500306

[135] W. Redfern *et al.*, “Relationships between preclinical cardiac electrophysiology, clinical QT interval prolongation and torsade de pointes for a broad range of drugs: evidence for a provisional safety margin in drug development,” *Cardiovasc. Res.*, vol. 58, no. 1, pp. 32–45, Apr. 2003, doi: 10.1016/S0008-6363(02)00846-5.

[136] M. Giorgi, R. Bolanos, C. Gonzalez, and G. Di Girolamo, “QT Interval Prolongation: Preclinical and Clinical Testing Arrhythmogenesis in Drugs and Regulatory Implications,” *Curr. Drug Saf.*, vol. 5, no. 1, pp. 54–57, Jan. 2010, doi: 10.2174/157488610789869148.

[137] B. Fermini *et al.*, “A New Perspective in the Field of Cardiac Safety Testing through the Comprehensive In Vitro Proarrhythmia Assay Paradigm,” *SLAS Discov.*, vol. 21, no. 1, pp. 1–11, Jan. 2016, doi: 10.1177/1087057115594589.

[138] A. Nijak, J. Saenen, A. J. Labro, D. Schepers, B. L. Loeys, and M. Alaerts, “iPSC-Cardiomyocyte Models of Brugada Syndrome—Achievements, Challenges and Future Perspectives,” *Int. J. Mol. Sci.*, vol. 22, no. 6, p. 2825, Mar. 2021, doi: 10.3390/ijms22062825.

[139] L. Sala, M. Gnecchi, and P. J. Schwartz, “Long QT Syndrome Modelling with Cardiomyocytes Derived from Human-induced Pluripotent Stem Cells,” *Arrhythmia Electrophysiol. Rev.*, vol. 8, no. 2, pp. 105–110, May 2019, doi: 10.15420/aer.2019.1.1.

[140] E. R. Pfeiffer, J. R. Tangney, J. H. Omens, and A. D. McCulloch, “Biomechanics of Cardiac Electromechanical Coupling and Mechanoelectric Feedback,” *J. Biomech. Eng.*, vol. 136, no. 2, p. 021007, Feb. 2014, doi: 10.1115/1.4026221.

[141] J. Constantino, Y. Hu, A. C. Lardo, and N. A. Trayanova, “Mechanistic insight into prolonged electromechanical delay in dyssynchronous heart failure: a computational study,” *Am. J. Physiol.-Heart Circ. Physiol.*, vol. 305, no. 8, pp. H1265–H1273, Oct. 2013, doi: 10.1152/ajpheart.00426.2013.

[142] S. S. An *et al.*, “Cell stiffness, contractile stress and the role of extracellular matrix,” *Biochem. Biophys. Res. Commun.*, vol. 382, no. 4, pp. 697–703, May 2009, doi: 10.1016/j.bbrc.2009.03.118.

[143] M. Jafari, S. Datla, E. L. Elson, B. E. Carlson, T. Wakatsuki, and F. Alisafaei, “Tension-Induced Stiffening of Cytoskeletal Components Regulates Cardiomyocyte Contractility,” Mar. 06, 2025, *Biophysics*. doi: 10.1101/2025.02.28.640898.

[144] S. Raj, V. I. Franco, and S. E. Lipshultz, “Anthracycline-Induced Cardiotoxicity: A Review of Pathophysiology, Diagnosis, and Treatment,” *Curr. Treat. Options Cardiovasc. Med.*, vol. 16, no. 6, p. 315, Jun. 2014, doi: 10.1007/s11936-014-0315-4.

[145] F. Gao, T. Xu, F. Zang, Y. Luo, and D. Pan, “Cardiotoxicity of Anticancer Drugs: Molecular Mechanisms, Clinical Management and Innovative Treatment,” *Drug Des. Devel. Ther.*, vol. Volume 18, pp. 4089–4116, Sep. 2024, doi: 10.2147/DDDT.S469331.

[146] S. M. Swain, M. Shastry, and E. Hamilton, “Targeting HER2-positive breast cancer: advances and future directions,” *Nat. Rev. Drug Discov.*, vol. 22, no. 2, pp. 101–126, Feb. 2023, doi: 10.1038/s41573-022-00579-0.

[147] M. Kciuk *et al.*, “Doxorubicin—An Agent with Multiple Mechanisms of Anticancer Activity,” *Cells*, vol. 12, no. 4, p. 659, Feb. 2023, doi: 10.3390/cells12040659.

[148] J. H. Doroshow, “Doxorubicin-Induced Cardiac Toxicity,” *N. Engl. J. Med.*, vol. 324, no. 12, pp. 843–845, Mar. 1991, doi: 10.1056/NEJM199103213241210.

[149] N. K. Ibrahim *et al.*, “Doxorubicin-induced congestive heart failure in elderly patients with metastatic breast cancer, with long-term follow-up: the M.D. Anderson experience,” *Cancer Chemother. Pharmacol.*, vol. 43, no. 6, pp. 471–478, Mar. 1999, doi: 10.1007/s002800050926.

[150] D. Cardinale *et al.*, “Early Detection of Anthracycline Cardiotoxicity and Improvement With Heart Failure Therapy,” *Circulation*, vol. 131, no. 22, pp. 1981–1988, Jun. 2015, doi: 10.1161/CIRCULATIONAHA.114.013777.

[151] Y.-W. Zhang, J. Shi, Y.-J. Li, and L. Wei, “Cardiomyocyte death in doxorubicin-induced cardiotoxicity,” *Arch. Immunol. Ther. Exp. (Warsz.)*, vol. 57, no. 6, pp. 435–445, Dec. 2009, doi: 10.1007/s00005-009-0051-8.

[152] M. Sheibani *et al.*, “Doxorubicin-Induced Cardiotoxicity: An Overview on Pre-clinical Therapeutic Approaches,” *Cardiovasc. Toxicol.*, vol. 22, no. 4, pp. 292–310, Apr. 2022, doi: 10.1007/s12012-022-09721-1.

[153] P. S. Rawat, A. Jaiswal, A. Khurana, J. S. Bhatti, and U. Navik, “Doxorubicin-induced cardiotoxicity: An update on the molecular mechanism and novel therapeutic strategies for effective management,” *Biomed. Pharmacother.*, vol. 139, p. 111708, Jul. 2021, doi: 10.1016/j.biopha.2021.111708.

[154] L. Xiao, Z. Hu, W. Zhang, C. Wu, H. Yu, and P. Wang, “Evaluation of doxorubicin toxicity on cardiomyocytes using a dual functional extracellular biochip,” *Biosens. Bioelectron.*, vol. 26, no. 4, pp. 1493–1499, Dec. 2010, doi: 10.1016/j.bios.2010.07.093.

[155] H.-G. Jahnke *et al.*, “A Novel 3D Label-Free Monitoring System of hES-Derived Cardiomyocyte Clusters: A Step Forward to In Vitro Cardiotoxicity Testing,” *PLoS ONE*, vol. 8, no. 7, p. e68971, Jul. 2013, doi: 10.1371/journal.pone.0068971.

[156] E. Lazzarini *et al.*, “Stress-induced premature senescence is associated with a prolonged QT interval and recapitulates features of cardiac aging,” *Theranostics*, vol. 12, no. 11, pp. 5237–5257, 2022, doi: 10.7150/thno.70884.

[157] W.-T. Chang, D. Yu, Y.-C. Lai, K.-Y. Lin, and I. Liau, “Characterization of the Mechanodynamic Response of Cardiomyocytes with Atomic Force Microscopy,” *Anal. Chem.*, vol. 85, no. 3, pp. 1395–1400, Feb. 2013, doi: 10.1021/ac3022532.

[158] I. Atukorala, N. Hannan, and L. Hui, “Immersed in a reservoir of potential: amniotic fluid-derived extracellular vesicles,” *J. Transl. Med.*, vol. 22, no. 1, p. 348, Apr. 2024, doi: 10.1186/s12967-024-05154-2.

[159] C. Balbi *et al.*, “Reactivating endogenous mechanisms of cardiac regeneration via paracrine boosting using the human amniotic fluid stem cell secretome,” *Int. J. Cardiol.*, vol. 287, pp. 87–95, Jul. 2019, doi: 10.1016/j.ijcard.2019.04.011.

[160] C. Balbi *et al.*, “First Characterization of Human Amniotic Fluid Stem Cell Extracellular Vesicles as a Powerful Paracrine Tool Endowed with Regenerative Potential,” *Stem Cells Transl. Med.*, vol. 6, no. 5, pp. 1340–1355, May 2017, doi: 10.1002/sctm.16-0297.

[161] A. Costa, R. Quarto, and S. Bollini, “Small Extracellular Vesicles from Human Amniotic Fluid Samples as Promising Theranostics,” *Int. J. Mol. Sci.*, vol. 23, no. 2, p. 590, Jan. 2022, doi: 10.3390/ijms23020590.

[162] F. Villa *et al.*, “The Human Fetal and Adult Stem Cell Secretome Can Exert Cardioprotective Paracrine Effects against Cardiotoxicity and Oxidative Stress from Cancer Treatment,” *Cancers*, vol. 13, no. 15, p. 3729, Jul. 2021, doi: 10.3390/cancers13153729.

[163] E. Lazzarini *et al.*, “The human amniotic fluid stem cell secretome effectively counteracts doxorubicin-induced cardiotoxicity,” *Sci. Rep.*, vol. 6, no. 1, p. 29994, Jul. 2016, doi: 10.1038/srep29994.

[164] A. Costa *et al.*, “Investigating the Paracrine Role of Perinatal Derivatives: Human Amniotic Fluid Stem Cell-Extracellular Vesicles Show Promising Transient Potential for Cardiomyocyte Renewal,” *Front. Bioeng. Biotechnol.*, vol. 10, p. 902038, Jun. 2022, doi: 10.3389/fbioe.2022.902038.

[165] C. Pipino, “Osteogenic differentiation of amniotic fluid mesenchymal stromal cells and their bone regeneration potential,” *World J. Stem Cells*, vol. 7, no. 4, p. 681, 2015, doi: 10.4252/wjsc.v7.i4.681.

[166] C. Balbi *et al.*, “Supporting data on in vitro cardioprotective and proliferative paracrine effects by the human amniotic fluid stem cell secretome,” *Data Brief*, vol. 25, p. 104324, Aug. 2019, doi: 10.1016/j.dib.2019.104324.

[167] V. Balducci *et al.*, “The human amniotic fluid stem cell secretome triggers intracellular $Ca^{2+}$ oscillations, NF-κB nuclear translocation and tube formation in human endothelial colony-forming cells,” *J. Cell. Mol. Med.*, vol. 25, no. 16, pp. 8074–8086, Aug. 2021, doi: 10.1111/jcmm.16739.

[168] J. A. Welsh *et al.*, “Minimal information for studies of extracellular vesicles (MISEV2023): From basic to advanced approaches,” *J. Extracell. Vesicles*, vol. 13, no. 2, p. e12404, Feb. 2024, doi: 10.1002/jev2.12404.

[169] A. Llach *et al.*, “Progression of excitation-contraction coupling defects in doxorubicin cardiotoxicity,” *J. Mol. Cell. Cardiol.*, vol. 126, pp. 129–139, Jan. 2019, doi: 10.1016/j.yjmcc.2018.11.019.

[170] V. Bhutani, F. Varzideh, S. Wilson, U. Kansakar, S. Jankauskas, and G. Santulli, “Doxorubicin-Induced Cardiotoxicity: A Comprehensive Update,” *J. Cardiovasc. Dev. Dis.*, vol. 12, no. 6, p. 207, May 2025, doi: 10.3390/jcdd12060207.

[171] B. Chen *et al.*, “Disruption of a GATA4/Ankrd1 Signaling Axis in Cardiomyocytes Leads to Sarcomere Disarray: Implications for Anthracycline Cardiomyopathy,” *PLoS ONE*, vol. 7, no. 4, p. e35743, Apr. 2012, doi: 10.1371/journal.pone.0035743.

[172] P. Dimitrakis, M.-I. Romay-Ogando, F. Timolati, T. M. Suter, and C. Zuppinger, “Effects of doxorubicin cancer therapy on autophagy and the ubiquitin-proteasome system in long-term cultured adult rat cardiomyocytes,” *Cell Tissue Res.*, vol. 350, no. 2, pp. 361–372, Nov. 2012, doi: 10.1007/s00441-012-1475-8.

[173] S. Upadhyay, K. B. Gupta, A. K. Mantha, and M. Dhiman, “A short review: Doxorubicin and its effect on cardiac proteins,” *J. Cell. Biochem.*, vol. 122, no. 2, pp. 153–165, Feb. 2021, doi: 10.1002/jcb.29840.

[174] G. Abdelsayed *et al.*, “2D and 3D in-Vitro models for mimicking cardiac physiology,” *Appl. Eng. Sci.*, vol. 12, p. 100115, Dec. 2022, doi: 10.1016/j.apples.2022.100115.

[175] X. Hu *et al.*, “Multimodal Characterization of Cardiomyocytes Cell Culture Using a Thin-Film-Transistor Microelectrodes Arrays (TFT-MEA)”.

[176] A. Tixier-Mita *et al.*, “Review on thin-film transistor technology, its applications, and possible new applications to biological cells,” *Jpn. J. Appl. Phys.*, vol. 55, no. 4S, p. 04EA08, Apr. 2016, doi: 10.7567/JJAP.55.04EA08.

[177] “1982 a new TFT.”

[178] T. P. Brody, J. A. Asars, and G. D. Dixon, “A 6 × 6 inch 20 lines-per-inch liquid-crystal display panel,” *IEEE Trans. Electron Devices*, vol. 20, no. 11, pp. 995–1001, Nov. 1973, doi: 10.1109/T-ED.1973.17780.

[179] G. W. Shim, W. Hong, J. Cha, J. H. Park, K. J. Lee, and S. Choi, “TFT Channel Materials for Display Applications: From Amorphous Silicon to Transition Metal Dichalcogenides,” *Adv. Mater.*, vol. 32, no. 35, p. 1907166, Sep. 2020, doi: 10.1002/adma.201907166.

[180] A. Tixier-Mita, S. Ihida, G. A. Cathcart, F. A. Shaik, and H. Toshiyoshi, “(Invited) More Than Moore Applications with Thin-Film-Transistors Array Substrates from Liquid Cristal Display: New Devices for Biological Cells Analyses,” *ECS Trans.*, vol. 72, no. 3, pp. 39–46, Apr. 2016, doi: 10.1149/07203.0039ecst.

[181] Y. Kuo, “Thin Film Transistor Technology--Past, Present, and Future,” *Interface Mag.*, vol. 22, no. 1, pp. 55–61, Jan. 2013, doi: 10.1149/2.F06131if.

[182] S. O. Kasap, “X-ray sensitivity of photoconductors: application to stabilized a-Se,” *J. Phys. Appl. Phys.*, vol. 33, no. 21, pp. 2853–2865, Nov. 2000, doi: 10.1088/0022-3727/33/21/326.

[183] C.-M. Yang *et al.*, “Nano-IGZO layer for EGFET in pH sensing characteristics,” in *2013 IEEE 5th International Nanoelectronics Conference (INEC)*, Singapore, Singapore: IEEE, Jan. 2013, pp. 480–482. doi: 10.1109/INEC.2013.6466083.

[184] P. Estrela and P. Migliorato, “Chemical and biological sensors using polycrystalline silicon TFTs,” *J Mater Chem*, vol. 17, no. 3, pp. 219–224, 2007, doi: 10.1039/B612469K.

[185] A. Tixier-Mita *et al.*, “Electronic Device from TFT Display for Applications on Biological Cells.”.

[186] J. L. Tan, J. Tien, D. M. Pirone, D. S. Gray, K. Bhadriraju, and C. S. Chen, “Cells lying on a bed of microneedles: An approach to isolate mechanical force,” *Proc. Natl. Acad. Sci.*, vol. 100, no. 4, pp. 1484–1489, Feb. 2003, doi: 10.1073/pnas.0235407100.

[187] M. L. Rodriguez, B. T. Graham, L. M. Pabon, S. J. Han, C. E. Murry, and N. J. Sniadecki, “Measuring the Contractile Forces of Human Induced Pluripotent Stem Cell-Derived Cardiomyocytes With Arrays of Microposts,” *J. Biomech. Eng.*, vol. 136, no. 5, p. 051005, May 2014, doi: 10.1115/1.4027145.

[188] F. Zhang *et al.*, “Continuous contractile force and electrical signal recordings of 3D cardiac tissue utilizing conductive hydrogel pillars on a chip,” *Mater. Today Bio*, vol. 20, p. 100626, Jun. 2023, doi: 10.1016/j.mtbio.2023.100626.

[189] A. Kajzar, C. M. Cesa, N. Kirchgeßner, B. Hoffmann, and R. Merkel, “Toward Physiological Conditions for Cell Analyses: Forces of Heart Muscle Cells Suspended Between Elastic Micropillars,” *Biophys. J.*, vol. 94, no. 5, pp. 1854–1866, Mar. 2008, doi: 10.1529/biophysj.107.115766.

[190] R. H. W. Lam, Y. Sun, W. Chen, and J. Fu, “Elastomeric microposts integrated into microfluidics for flow-mediated endothelial mechanotransduction analysis,” *Lab. Chip*, vol. 12, no. 10, p. 1865, 2012, doi: 10.1039/c2lc21146g.

[191] Z. Liu *et al.*, “Mechanical tugging force regulates the size of cell–cell junctions,” *Proc. Natl. Acad. Sci.*, vol. 107, no. 22, pp. 9944–9949, Jun. 2010, doi: 10.1073/pnas.0914547107.

[192] C. M. Nelson *et al.*, “Emergent patterns of growth controlled by multicellular form and mechanics,” *Proc. Natl. Acad. Sci.*, vol. 102, no. 33, pp. 11594–11599, Aug. 2005, doi: 10.1073/pnas.0502575102.

[193] J. Park *et al.*, “Directed migration of cancer cells guided by the graded texture of the underlying matrix,” *Nat. Mater.*, vol. 15, no. 7, pp. 792–801, Jul. 2016, doi: 10.1038/nmat4586.

[194] I. Miranda *et al.*, “Properties and Applications of PDMS for Biomedical Engineering: A Review,” *J. Funct. Biomater.*, vol. 13, no. 1, p. 2, Dec. 2021, doi: 10.3390/jfb13010002.

[195] M. Akhmanova, E. Osidak, S. Domogatsky, S. Rodin, and A. Domogatskaya, “Physical, Spatial, and Molecular Aspects of Extracellular Matrix of *In Vivo* Niches and Artificial Scaffolds Relevant to Stem Cells Research,” *Stem Cells Int.*, vol. 2015, pp. 1–35, 2015, doi: 10.1155/2015/167025.

[196] N.-E. Oyunbaatar, A. Shanmugasundaram, and D.-W. Lee, “Contractile behaviors of cardiac muscle cells on mushroom-shaped micropillar arrays,” *Colloids Surf. B Biointerfaces*, vol. 174, pp. 103–109, Feb. 2019, doi: 10.1016/j.colsurfb.2018.10.058.

[197] M. Sakamiya, Y. Fang, X. Mo, J. Shen, and T. Zhang, “A heart-on-a-chip platform for online monitoring of contractile behavior via digital image processing and piezoelectric sensing technique,” *Med. Eng. Phys.*, vol. 75, pp. 36–44, Jan. 2020, doi: 10.1016/j.medengphy.2019.10.001.

[198] M. Lejeune, T. Chartier, C. Dossou-Yovo, and R. Noguera, “Ink-jet printing of ceramic micro-pillar arrays,” *J. Eur. Ceram. Soc.*, vol. 29, no. 5, pp. 905–911, Mar. 2009, doi: 10.1016/j.jeurceramsoc.2008.07.040.

[199] Z. Faraji Rad, P. D. Prewett, and G. J. Davies, “High-resolution two-photon polymerization: the most versatile technique for the fabrication of microneedle arrays,” *Microsyst. Nanoeng.*, vol. 7, no. 1, p. 71, Sep. 2021, doi: 10.1038/s41378-021-00298-3.

[200] L. Sun *et al.*, “Chemical vapour deposition,” *Nat. Rev. Methods Primer*, vol. 1, no. 1, p. 5, Jan. 2021, doi: 10.1038/s43586-020-00005-y.

[201] A.-C. Eiler *et al.*, “Thin-Film Transistor Platform for Electrophysiological and Electrochemical Characterization of Biological Cells,” in *2020 IEEE International Electron Devices Meeting (IEDM)*, Dec. 2020, p. 14.2.1-14.2.4. doi: 10.1109/IEDM13553.2020.9372043.

[202] A. Tixier-Mita *et al.*, “A test structure to characterize transparent electrode array platform with TFTs for bio-chemical applications,” in *2017 International Conference of Microelectronic Test Structures (ICMTS)*, Mar. 2017, pp. 1–5. doi: 10.1109/ICMTS.2017.7954278.

[203] O. A. Bauchau and J. I. Craig, “Euler-Bernoulli beam theory,” in *Structural Analysis*, vol. 163, O. A. Bauchau and J. I. Craig, Eds., in Solid Mechanics and Its Applications, vol. 163. , Dordrecht: Springer Netherlands, 2009, pp. 173–221. doi: 10.1007/978-90-481-2516-6_5.

[204] S. K. Motwani and H. Saunders, “Inotropes,” *Anaesth. Intensive Care Med.*, vol. 25, no. 3, pp. 185–191, Mar. 2024, doi: 10.1016/j.mpaic.2023.11.019.

[205] M. W. Szymanski, P. Patel, and D. P. Singh, “Isoproterenol,” in *StatPearls*, Treasure Island (FL): StatPearls Publishing, 2026. [Online]. Available: http://www.ncbi.nlm.nih.gov/books/NBK526042/

[206] A.-C. Eiler *et al.*, “Application of a Thin-Film Transistor Array for Cellular-Resolution Electrophysiology and Electrochemistry,” *IEEE Trans. Electron Devices*, vol. 68, no. 4, pp. 2041–2048, Apr. 2021, doi: 10.1109/TED.2021.3050432.

[207] T. Xu, S. Ihida, H. Toshiyoshi, and A. Tixier-Mita, “Instrumentation development for 2D bioimpedance mapping with a Thin-Film-Transistor active matrix device,” in *2022 Symposium on Design, Test, Integration and Packaging of MEMS/MOEMS (DTIP)*, Jul. 2022, pp. 1–4. doi: 10.1109/DTIP56576.2022.9911743.

[208] A. Tixier-Mita *et al.*, “34-3: Sensing and Biomimetic Stimulation of Cardiomyocyte Cell Culture with a Thin-Film-Transistor Active-Matrix Platform,” *SID Symp. Dig. Tech. Pap.*, vol. 55, no. 1, pp. 439–442, Jun. 2024, doi: 10.1002/sdtp.17552.